FINAL REPORT

Predicting the Effects of Fuel Composition and Flame Structure on Soot Generation in Turbulent Non-Premixed Flames

SERDP Project WP-1578

MARCH 2011

Christopher R. Shaddix
Sandia National Laboratories

Hai Wang
University of Southern California

Robert W. Schefer
Joseph C. Oefelein
Lyle M. Pickett
Sandia National Laboratories

This document has been cleared for public release

SERDP
DOD • EPA • DOE

REPORT DOCUMENTATION PAGE

Form Approved
OMB No. 0704-0188

Public reporting burden for this collection of information is estimated to average 1 hour per response, including the time for reviewing instructions, searching existing data sources, gathering and maintaining the data needed, and completing and reviewing this collection of information. Send comments regarding this burden estimate or any other aspect of this collection of information, including suggestions for reducing this burden to Department of Defense, Washington Headquarters Services, Directorate for Information Operations and Reports (0704-0188), 1215 Jefferson Davis Highway, Suite 1204, Arlington, VA 22202-4302. Respondents should be aware that notwithstanding any other provision of law, no person shall be subject to any penalty for failing to comply with a collection of information if it does not display a currently valid OMB control number. **PLEASE DO NOT RETURN YOUR FORM TO THE ABOVE ADDRESS.**

1. REPORT DATE *(DD-MM-YYYY)*	2. REPORT TYPE	3. DATES COVERED *(From - To)*
28-03-2011	Final	Mar 2007 – Mar 2011

4. TITLE AND SUBTITLE
Predicting the Effects of Fuel Composition and Flame Structure on Soot Generation in Turbulent Non-Premixed Flames: SERDP WP-1578

5a. CONTRACT NUMBER

5b. GRANT NUMBER

5c. PROGRAM ELEMENT NUMBER

6. AUTHOR(S)
Christopher R. Shaddix, Hai Wang, Robert W. Schefer, Joseph C. Oefelein, Lyle M. Pickett

5d. PROJECT NUMBER
WP-1578

5e. TASK NUMBER

5f. WORK UNIT NUMBER

7. PERFORMING ORGANIZATION NAME(S) AND ADDRESS(ES)

Sandia National Laboratories
7011 East Avenue
Livermore, CA 94550

University of Southern California
Los Angeles, CA 90089

8. PERFORMING ORGANIZATION REPORT NUMBER

9. SPONSORING / MONITORING AGENCY NAME(S) AND ADDRESS(ES)
Strategic Environmental Research and Development Program

Arlington, VA

10. SPONSOR/MONITOR'S ACRONYM(S)
SERDP

11. SPONSOR/MONITOR'S REPORT NUMBER(S)

12. DISTRIBUTION / AVAILABILITY STATEMENT

13. SUPPLEMENTARY NOTES

14. ABSTRACT
This project aimed to develop a reduced chemistry and soot model for making accurate predictions of soot emissions from military gas turbine engines. Measurements of soot formation were performed in laminar flat premixed flames and turbulent non-premixed jet flames at 1 atm pressure and in turbulent liquid spray flames under representative conditions for takeoff in a gas turbine engine. Fuels investigated included ethylene and a JP-8 surrogate consisting of n-dodecane and m-xylene. The pressurized turbulent jet flame measurements demonstrated that the surrogate fuel was representative of actual JP-8. The premixed flame measurements revealed that flame temperature has a strong impact on the rate of soot nucleation and particle coagulation. Mean and rms soot concentrations were measured throughout the turbulent non-premixed jet flames, together with soot concentration-temperature data, as well as spatially resolved radiant emission. A detailed chemical kinetic mechanism for ethylene combustion, including fuel-rich chemistry and benzene formation steps, was compiled, validated, and reduced. The reduced ethylene mechanism was incorporated into a high-fidelity large eddy simulation (LES) code, together with a moment-based soot model and different models for thermal radiation. The LES results highlight the importance of including an optically-thick radiation model to accurately predict gas temperatures and thus soot formation rates. When including such a radiation model, the LES model predicts mean soot concentrations within 30% in the ethylene jet flame.

15. SUBJECT TERMS
Gas turbine, soot formation, jet flames, JP-8, ethylene, premixed flat flame, radiation, LES

16. SECURITY CLASSIFICATION OF:			17. LIMITATION OF ABSTRACT	18. NUMBER OF PAGES	19a. NAME OF RESPONSIBLE PERSON
					Christopher Shaddix
a. REPORT	**b. ABSTRACT**	**c. THIS PAGE**			**19b. TELEPHONE NUMBER** *(include area code)* 925-294-3840

Standard Form 298 (Rev. 8-98)
Prescribed by ANSI Std. Z39.18

Table of Contents   Page

List of Acronyms

AFM	atomic force microscopy
AFRL	Air Force Research Lab
ALS	Advanced Light Source
Ar	argon
ASTM	American Society for Testing and Materials
BSSF	burner-stabilized stagnation-flow
C_2H_2	acetylene
C_2H_4	ethylene
$C_{12}H_{26}$	dodecane
CaF_2	calcium fluoride
CFD	computational fluid dynamic
CH	methylidyne
CH_4	methane
CH_2O	formaldehyde
CMC	conditional moment closure
CO	carbon monoxide
CO_2	carbon dioxide
CPC	condensation particle counter
cw	continuous wave (i.e. non-pulsed)
DOE	Department of Energy
DMA	differential mobility analyzer
DNS	direct numerical simulation
DRO	Direct Reduction-Optimization
EGR	exhaust gas recirculation
EPA	Environmental Protection Agency
FSK	full-spectrum k-distribution
FT	Fischer-Tropsch
FTIR	fourier transform infrared
GE	General Electric
GEAE	General Electric Aircraft Engines
H	atomic hydrogen
H_2	molecular hydrogen
H_2O	water
H/C	ratio of fuel hydrogen to carbon

HACA	hydrogen-abstraction-carbon-addition
HeNe	helium-neon
IBM	International Business Machines
ID	internal diameter
JP-8	jet propulsion 8 (U.S. military jet fuel)
K_e	dimensionless extinction coefficient
LES	large eddy simulation
LII	laser-induced incandescence
LOI	Level of Importance
MPI	Message Passing Interface
MURI	Multi-University Research Initiative
N_2	molecular nitrogen
NERSC	National Energy Research Scientific Computing Center
NIST	National Institute of Standards and Technology
NO	nitric oxide
NO_2	nitrogen dioxide
O	atomic oxygen
O_2	molecular oxygen
OH	hydroxyl radical
P&W	Pratt & Whitney
PAH	polycyclic aromatic hydrocarbons
PDF	probability density function
PIV	particle-image velocimetry
PLIF	planar laser-induced fluorescence
PLII	planar laser-induced incandescence
PM	particulate matter
PM2.5	particulate matter with an aerodynamic diameter less than 2.5 micrometers
PSDF	particle size distribution function
PSR	perfectly stirred reactor
QSST	quasi-steady state

RANS	Reynolds-averaged Navier Stokes		TEM	transmission electron microscopy
Re	Reynolds number		TNF	turbulent nonpremixed flame
RRKM	Rice, Ramsperger, Kassel, and Marcus		UIC	University of Illinois at Chicago
SERDP	Strategic Environmental Research and Development Program		U.S.	United States
			USC	University of Southern California
SGS	subgrid-scale		UTRC	United Technologies Research Center
SMPS	Scanning Mobility Particle Sizer		UV	ultraviolet
SPMD	Single-Program—Multiple-Data		YAG	yttrium aluminium garnet
TCL	Turbulent Combustion Laboratory			

List of Figures   **Page**

x

List of Tables   Page

Acknowledgements

1.0 Abstract

This project featured collaborative research between the University of Southern California and Sandia National Laboratories, with the primary aim of developing and evaluating a reduced chemistry and soot model for making accurate predictions of soot emissions from military gas turbine engines. Collaborative discussions and information sharing also occurred with the other four projects on soot formation that were also funded by SERDP coincidentally with this project, in what became known as the SERDP Soot Science working group. Discussions were also held with researchers from General Electric Aircraft Engines (GEAE) and Pratt & Whitney (P&W) regarding the project research plans and the results of the project.

Measurements of soot formation were performed in laminar flat premixed flames and turbulent non-premixed jet flames at 1 atm pressure and in turbulent liquid spray flames under representative conditions for takeoff in a gas turbine engine. The laminar flames and open jet flames used both ethylene and a prevaporized JP-8 surrogate fuel, according to the surrogate formulation consisting of n-dodecane and m-xylene developed by the SERDP Soot Science working group. The pressurized turbulent jet flame measurements used the JP-8 surrogate fuel and compared its combustion and sooting characteristics to typical JP-8 fuel samples, demonstrating that the surrogate was representative of JP-8, with a tendency to strong soot formation. The premixed flame measurements revealed that flame temperature has a strong impact on the rate of soot nucleation and particle coagulation. Even in the higher temperature flames, the soot particles demonstrated liquid-like behavior. Doping of benzene into ethylene fuel and operating the burner on n-dodecane was shown to have little influence on the trends previously established for ethylene fuel. Significant quantities of aliphatic carbon were shown to be present in soot sampled from the premixed flames, increasing with flame temperature and height above the flame.

An extensive array of non-intrusive optical and laser-based measurements was performed in turbulent non-premixed jet flames established on specially designed piloted burners with well-defined boundary conditions (to assist comparisons with models). Mean and statistical soot concentration data was collected throughout the flames, together with instantaneous images showing the relationship between soot and the OH radical and soot and PAH. Time-records of local soot concentration-temperature were collected, as well as spatially resolved thermal radiation emitted from the flames. Measurements of red laser light extinction across the flames provided useful data for correcting the soot concentration measurements for signal trapping in these optically thick flames.

A detailed chemical kinetic mechanism for ethylene combustion, including fuel-rich chemistry and benzene formation steps, was compiled, validated, and reduced. An attempt was made to develop a detailed mechanism for the JP-8 surrogate, but the existing knowledge of m-xylene chemistry was found to be insufficient to yield suitable agreement with validation data. The reduced ethylene mechanism was incorporated into a high-fidelity large eddy simulation (LES) code, together with a moment-based soot model and models for thermal radiation, to evaluate the ability of the chemistry and soot models to predict soot formation in the jet diffusion flame. The LES results highlight the importance of including an optically-thick radiation model to accurately predict gas temperatures and thus soot formation rates. When including such a

radiation model, the LES model predicts mean soot concentrations within 30% in the ethylene jet flame.

The results of this project suggest that LES modeling, when incorporating suitably reduced chemical kinetics with fuel-rich chemistry and a suitable, optically-thick radiation model, can predict soot formation with good accuracy in an ethylene nonpremixed jet flame (at 1 atm) when using a fairly simple soot model (developed explicitly for application to ethylene flames). Extension of this predictive ability to more complex fuels representative of JP-8 requires improvements in the understanding of aromatic oxidation and pyrolysis chemistry and may require further improvements to the soot model itself.

2.0 Objective

The goal of this project was to develop a reduced chemical model and associated experimental data that permit accurate predictions by combustor models of engine-out fine particulate matter (PM) emissions, dominated by soot, from military gas turbine engines. By combining laminar, 1-D flame measurements and modeling of particle size distributions and chemistry, detailed flow field and soot measurements in open jet flames, and high-fidelity turbulent flame modeling, an accurate reduced-chemistry model for soot formation and oxidation was generated that is available for use by engine designers to reduce soot emissions in future engines and to evaluate the effects of fuel composition and the use of fuel additives on soot emissions.

Several secondary objectives included the following: (1) improving the understanding of the evolution of soot optical properties and particle size distribution function (PSDF) during the soot mass growth process; (2) improving the understanding of soot formation and oxidation as a function of turbulence mixing, fuel composition, and pressure; and (3) improving the ability to predict soot formation and oxidation using large eddy simulation (LES) methods.

3.0 Background

The health effects of fine particulate matter in ambient air are becoming increasingly evident. These particles are able to deeply penetrate lung tissue and have been shown to have a number of deleterious effects associated with the pulmonary and cardiovascular systems, leading to increased human morbidity and mortality [1-8]. As a consequence, the U.S. Environmental Protection Agency (EPA) has been setting increasingly strict ambient air quality standards for particulate matter with an aerodynamic diameter less than 2.5 micrometers (PM2.5). Furthermore, local regulatory agencies are working to minimize emissions of fine particulates or of gaseous compounds (such as sulfur and ammonia) that generate fine particulates in the atmosphere. Airports and military bases are receiving increased attention in this regard, as they can be significant point sources for emissions of these pollutants. Gas turbine engines are important sources of PM2.5 emissions at these locations. In addition, in-flight emission of fine particulates from gas turbine engines has effects on contrail/cloud formation and climate forcing [9].

In light of these considerations, in addition to considerations of infrared signatures and excessive heating of the gas turbine liner, there is a strong interest in reducing the emission of particulate matter (dominated by soot particles) from military gas turbine engines. In particular, it is desirable to have a truly predictive modeling capability for soot emission, considering the influence of changes in the fuel chemical composition (either bulk composition or with the inclusion of additives) and in the engine design and operation.

The traditional approach to predicting soot emissions from gas turbine engines is to use one of a large number of empirical correlation formulas that have been developed relating soot emission to bulk fuel composition and/or the laminar smoke point of the particular fuel. These correlations have been based on fuel hydrogen content, H/C ratio, aromatic content, and naphthalene content, among other variables [10]. However, soot emissions vary considerably with combustor operating conditions (i.e. idle, cruise, and takeoff settings), as would be expected with the resultant variations in combustor inlet temperature and pressure [11,12]. Therefore, the most advanced empirical correlations attempt to take into account the effects of operating conditions, for example as they relate to the characteristic residence times in the fuel-rich primary zone and the oxidating secondary zone [13]. Even with this degree of sophistication, however, empirical correlations generally do not offer predictability better than a mean standard deviation of 40% for a range of fuels and operating conditions, for a given engine design [13]. Furthermore, the range of applicability of a given correlation is usually very narrow and the use of the correlation is generally limited to the gas turbine combustor in which the correlation is developed. Consequently, the empirical approach has not yielded effective predictability of soot emissions.

In the last 10-15 years, several computational fluid dynamic (CFD) modeling approaches have been attempted for prediction of soot emissions from gas turbine combustors, using standard k-ε models to describe mean turbulence properties [14-19]. The soot formation and oxidation rates have been based on laminar flamelet approaches for non-premixed flames, assuming that the presence of soot does not affect the structure of the laminar flamelets (i.e., low soot limit). Most of the calculations to-date have used various simplifying assumptions: (a) soot oxidation by O_2 only, (b) soot formation constants taken from studies using propane or ethylene, and/or (c)

calculations performed for steady laminar flamelets. Furthermore, in all case radiant heat transfer from soot was ignored. These modeling attempts largely failed to accurately predict engine-out soot emission (usually the only soot measurement available), even with some partially tuned parameters and often when only making comparisons against a single engine/operating condition. In some cases, the predicted soot masses were exceedingly high (by orders of magnitude), while in others they were low. All of the simulations have shown that the soot concentrations in the primary combustion zone are several orders of magnitude higher than the exhaust soot concentrations, demonstrating that accurate predictions of soot oxidation rates are as important as predictions of soot inception and mass growth rates for determining engine-out soot emissions.

Recent efforts at improving the accuracy of CFD modeling of gas turbine combustors have focused on the development of large eddy simulation (LES) approaches [20-24]. LES, in contrast to the traditional CFD approach known as Reynolds-averaged Navier Stokes (RANS), accurately tracks large unsteady vortical motions and properly accounts for their effect on mean flow quantities. In gas turbine combustor flows, fluid mixing is driven by such vortices, so LES is expected to give superior results in comparison to RANS approaches. The long timescales associated with soot formation make it especially sensitive to large-scale vortex mixing processes [25,26], and therefore make its accurate prediction much more likely with LES. However, the computational demands for LES are much greater than for RANS, so currently only relatively crude LES models have been employed to simulate actual gas turbine combustor operation. In the future, as LES is further developed and computational capabilities improve, it is expected that LES models with the capability of calculating soot concentrations will be employed for simulating gas turbine combustors.

Currently, LES modeling is being used to further the understanding of chemistry-turbulence interactions in simpler, idealized flame geometries such as open jet flames [27-33]. Much of this work has been coordinated as part of a collaborative international research effort associated with the International Workshop on Measurement and Computation of Turbulent Nonpremixed Flames (www.ca.sandia.gov/TNF), led by researchers at the Combustion Research Facility of Sandia National Labs. Under funding from the U.S. DOE Basic Energy Sciences program, several canonical flame systems have been investigated in Sandia's Turbulent Combustion Laboratory (TCL) using an array of laser diagnostic techniques to provide an extensive experimental database for comparison with model predictions. Flames studied in the TCL have been selected to address a progression in chemical-kinetic and flow-field complexity, starting with simple hydrogen jet flames. Specific experiments, as well as the overall progression of flames, have been designed to allow separate physical processes and individual submodels to be isolated. For example, a series of H_2 flames with helium dilution allowed a detailed evaluation of NO predictions, independent of uncertainties in the radiation model [34]. Jet flames of $CO/H_2/N_2$ [35] and $CH_4/N_2/H_2$ [36] have added kinetic complexity, while maintaining the simple, attached jet-flame geometry. The series of piloted CH_4/air jet flames [37] includes increasing degrees of localized extinction that tests the ability of models to treat strong interactions of turbulence and chemistry. This systematic progression is essential to the development of robust, predictive, integrated models that have a solid basis in fundamental combustion science.

In this project, we built on this established hierarchy of canonical turbulent non-premixed flames and focused on flames that include soot and the relevant fuel chemistry for military gas turbines

(i.e. a JP-8 surrogate). As with the previous flames investigated in the TCL, a variety of laser diagnostic methods were employed to provide the best-possible experimental database for detailed comparisons with model predictions. For the sooty flames investigated in this project, several of the laser diagnostic approaches that have been routinely employed in the nonsooting TNF workshop flames (such as Raman scattering and Rayleigh scattering) cannot be effectively employed. However, previous research at Sandia has demonstrated that several different techniques that give important information about the flow field, flame structure, soot field, and radiation field can be effectively employed in unsteady sooty non-premixed flames, and these techniques were employed in this investigation. In addition, the geometric, boundary and flow conditions associated with the flame system were carefully controlled and recorded, allowing modelers to identically match these conditions. In contrast, other existing experimental databases for sooty turbulent non-premixed flames involve a scarcity of measured parameters (typically only soot concentrations and mean temperature) and usually involve poorly defined boundary conditions. Consequently, flame modelers have insufficient data available with which to validate proposed models of soot formation and oxidation.

Pressure and ambient temperature are known to have strong influences on soot formation in non-premixed flames. Over the past ten years, the effects of the liquid fuel injection process and ambient pressure and temperature conditions on flame ignition and soot formation under diesel combustion conditions have been systematically investigated in Sandia's Engine Combustion Simulation Lab. Recently, interest in the Single-Fuel Concept for the U.S. military has led to research on JP-8 jet flame properties under simulated diesel combustion conditions. In this project we capitalized on this existing dataset with world-average JP-8 and a natural gas Fischer-Tropsch (FT) JP-8 fuel to compare the combustion performance of the JP-8 surrogate chosen by the SERDP Soot Science research group against these fuel standards. Furthermore, we performed measurements under appropriate takeoff conditions for military gas turbines to provide insight into the important parameters for soot formation and for validation data for future modeling predictions of soot formation.

Finally, to incorporate a realistic chemical kinetic model of the soot formation and oxidation processes into a high-fidelity LES code, a significant effort of this project has been to generate appropriate detailed and reduced chemical kinetic mechanisms for the combustion and pyrolysis reactions of the investigated fuels. Clearly, use of a full, detailed chemical kinetic mechanism for JP-8 (or even for a JP-8 surrogate), with at least 200 chemical species and over 1000 reactions is not computationally feasible for all but the simplest CFD solver, unless this information is conveyed in laminar flamelet lookup tables. Rather, for a high-fidelity LES model of a turbulent jet flame no more than approximately 20 reactive scalars can currently be carried in the calculation. Therefore, only the essential chemical species to describe the primary combustion reactions and to describe the primary steps of soot formation, growth, and oxidation can be incorporated into the model. Determining these species and the associated reduced chemical steps and rate constants is a key part of development of an effective LES architecture for predicting soot concentrations.

Another key ingredient of successful soot modeling in non-premixed flames, not fully recognized at the beginning of this project, is the incorporation of a suitable radiation model. The incorporation of radiation effects is important to yield accurate flame temperature predictions, which in turn control soot formation and oxidation rates. There are many different approaches to

radiation modeling, with vastly differing computational requirements and overall accuracy, depending on the optical thickness of the flame in question. To keep computational costs reasonable, we investigated the influence of the simplest type of radiation model (assuming an optically thin environment with no radiant absorption) and a reasonably accurate model for flames with some optical thickness (i.e. with radiant absorption).

4.0 Materials and Methods

This project consisted of several distinct but interacting efforts, as shown in Figure 1. Experimental measurements were performed in laminar premixed flat flames, turbulent non-premixed jet flames, and pressurized spray flames. In addition, a reduced-chemistry soot model was developed and applied via LES to the investigated turbulent ethylene non-premixed jet flame. The information derived from the laminar flame studies fed (together with literature data) into the development of the reduced chemical and soot model, while the turbulent flame measurements and the reduced model fed into the LES modeling effort. The pressurized spray flame investigation provided an important check on the combustion and soot formation tendencies of the two-component SERDP JP-8 surrogate fuel under practically relevant conditions. Ethylene and prevaporized JP-8 surrogate were investigated in the laminar flat flames and the turbulent nonpremixed jet flames, while the liquid JP-8 surrogate was investigated in the spray flames.
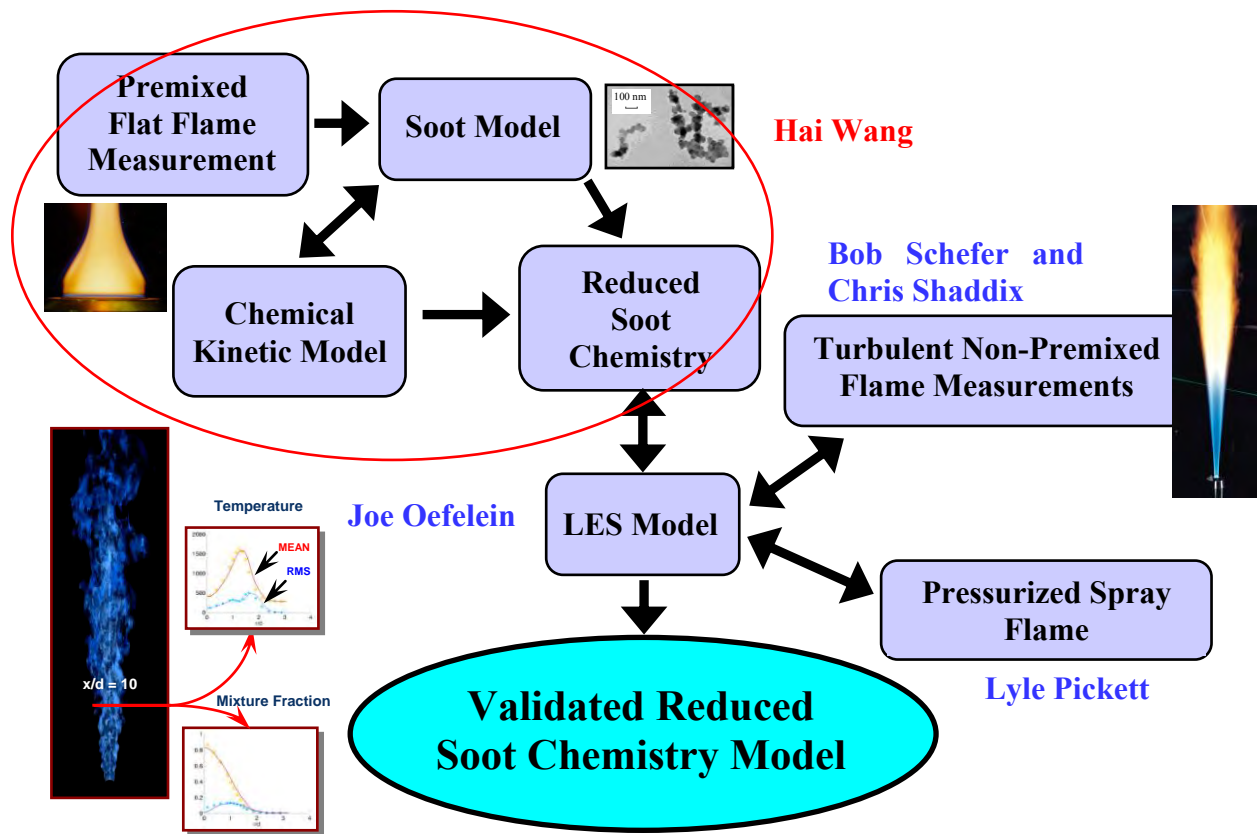
Figure 1.   Graphical representation of major activities in this research project, leading to the production of a validated reduced soot chemistry model for predictions of soot emissions from gas turbine engines.

Ethylene was chosen as the initial fuel for investigation because its combustion chemistry is well understood and it has seen extensive investigation in previous studies of soot formation. Also, a semi-detailed model for soot formation in non-premixed flames has been developed, with

specific application to laminar ethylene flames [38] and served well as a test case for predictiveness in the LES computations of the non-premixed turbulent jet flames. JP-8, in the form of a simplified chemical surrogate mixture, was also chosen for investigation in this project, to provide direct relevance to aviation-fueled engines.

4.1 Soot Chemistry Model

A predictive model of soot formation includes three logical parts: (i) a gas-phase chemistry model describing the rate of heat release and fuel ignition; (ii) a gas-phase model predicting the production and destruction of relevant precursor species for soot nucleation, namely polycyclic aromatic hydrocarbons (PAH); and (iii) a gas-surface and aerosol dynamics model for soot nucleation and mass growth. In this project, an updated detailed gas-phase chemistry model for ethylene combustion was compiled and combined with a PAH model. This model was then validated against experimental measurements of laminar flame speed, ignition delay (shock tube), and individual species concentrations in flat flames and flow reactor experiments.

Participants from the current set of SERDP soot program projects chose to use a common JP-8 surrogate, with consideration of the recommendations from the Surrogate Working Group and the MURI projects that were recently initiated on this topic. This surrogate composition was chosen to be a blend of 77 vol-% n-dodecane and 23 vol-% m-xylene. A detailed chemical kinetic model for this surrogate was constructed, based on a mechanism for n-dodecane combustion derived from the JetSuRF alkane combustion mechanism developed at USC [39] and an m-xylene reaction mechanism developed by the Nancy research group in France [40].

Although many fundamental soot models have been proposed over the last 15 years, the physical and chemical processes in these models are fundamentally the same as those proposed in the early 1990's [41-43]. The formation and mass growth of polycyclic aromatic hydrocarbons include the hydrogen-abstraction-carbon-addition mechanism (HACA) [41] and the more recently recognized kinetic processes involving resonantly stabilized species [44,45]. Though the exact mechanism of soot inception remains somewhat empirical, this obstacle does not seem to notably affect soot mass predictions [46]. The formation and growth of soot particles are described by collision-induced coalescence, surface reaction/oxidation, and surface condensation, and, when particles exceed a certain size, by particle-particle agglomeration, leading to fractal-like aggregates. Several methods of solution of aerosol dynamics have been proposed, including the moment [41,42], sectional [47], Galerkin [48], and stochastic methods [46,49,50]. Because of limitations on the number of species and variables high-fidelity LES models are able to handle, the moment method remains the most promising near-term solution to soot aerosol dynamics and was used in this project.

4.2 Soot Chemistry Model Reduction

Current computational capabilities place an upper limit of approximately 20 reactive scalars for high-fidelity LES simulations of jet flames with sufficient spatial resolution. Though the permissible number of scalars is likely to increase in the next several years, simulations using a full, or even skeletal, soot chemistry model are probably not feasible for many years to come. Because of the wide ranges of timescales involved in soot chemistry, the problem of model reduction was approached using an array of suitable techniques. The detailed reaction model was

first reduced to a skeletal model that could account for fuel ignition and heat release as well as the formation of the first aromatic ring. Subsequently, the skeletal reaction mechanism was reduced to 20 species using the Level of Importance (LOI) approach [51]. The PAH chemistry was reduced using a neural network approach. In the neural network approach, the production rate of a soot-precursor PAH (e.g., pyrene) was mapped as a function of the local concentrations of the hydrogen atom, acetylene, and molecular oxygen, residence time, and temperature in a piecewise fashion over the entire space of the independent variables. This procedure ensured the PAH production rates to be continuous in the entire independent-variable space. Lastly, the soot number density and mean particle diameter was modeled with a 2-moment method. In this way, the total number of reactive scalars was limited to 20 chemical species, plus the concentration of a characteristic PAH and two variables to describe soot chemistry. Development and validation of the reduced model was based on the detailed-chemistry model previously discussed.

4.3 Flat Flame Measurements

Scanning Mobility Particle Sizer (SMPS) characterization of soot PSDFs was performed in premixed, burner-stabilized C_2H_4 flames (see Fig. 2) over a range of flame temperature and C/O ratios, using previously established experimental methods and procedures [46,52,53]. The SMPS device consists of a differential mobility analyzer (DMA), which uses an electron mobility classifier to sort particles according to size, followed by a condensation particle counter (CPC), which increases the size of the sorted particles through condensation and then optically counts each particle [54]. A schematic of the experimental arrangement for performing particle sampling and analysis by either SMPS or thermal desorption mass spectrometry is shown in Fig. 3. Special attention was placed on the evolution of soot aerosol dynamics from coalescence to agglomeration. Various degrees of particle carbonization were studied by characterizing flames over a wide range of post-flame temperature and residence time.

Figure 2.   Photograph of typical sooting ethylene premixed
flat flame, stabilized on a McKenna burner.

Since the mobility diameter (measured by the SMPS) gives a direct measure of the particle size only if the particles are spherical, some transmission electron microscopy (TEM) grid samples were collected to examine the morphology of soot. For fractal aggregates, the relation between mobility diameter and fractal aggregate properties is currently being developed [55]. The results from this element of study improved the understanding of the evolution of soot optical properties, specifically during the critical transition from particle coalescence to particle agglomeration during the soot mass and size growth process.
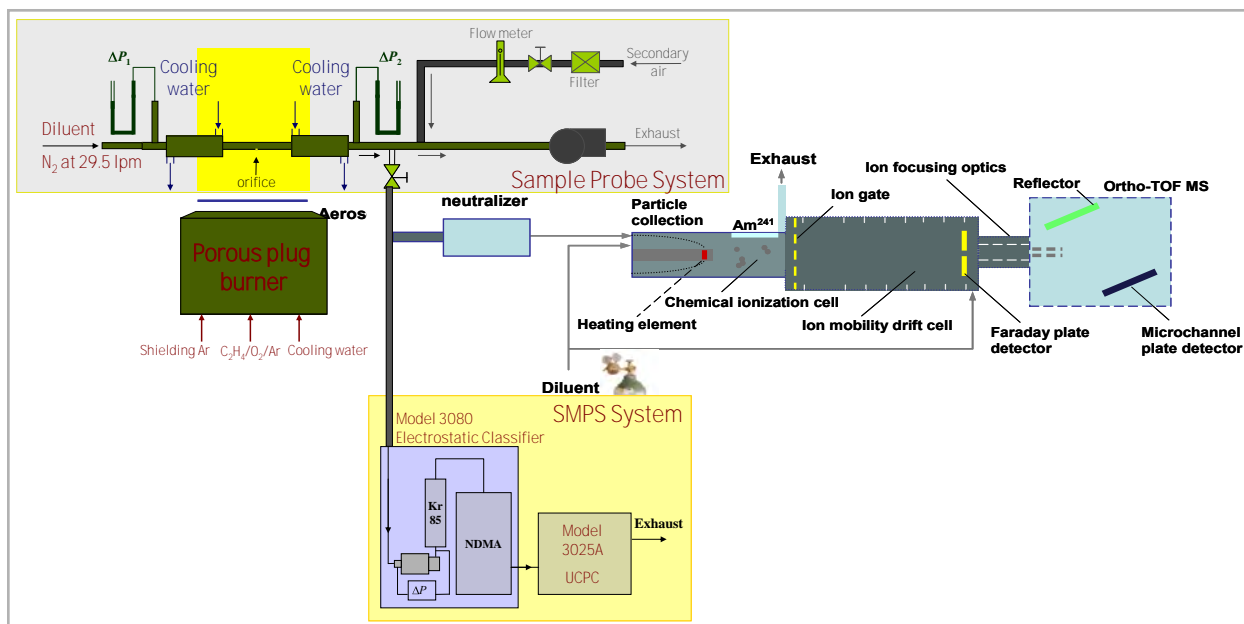
Figure 3.   Schematic diagram of flat flame soot sampling and analysis by SMPS or thermal desorption chemical ionization mobility mass spectrometry, which was not used in this study.

4.4 Turbulent Non-Premixed Flame Measurements

A detailed set of measurements of soot, flow field, and chemical properties was performed on open jet turbulent non-premixed flames with well-documented boundary and initial conditions. Ethylene was chosen to be the first fuel investigated to act as a bridge between the nonsooting, small-hydrocarbon flames that have traditionally been used to develop models of turbulence-chemistry interactions and the more heavily sooting kerosene flames. Following the ethylene flame measurements, the two-component SERDP JP-8 surrogate was investigated.

When using liquid fuels, it is advisable for comparisons with high-fidelity models to separate out the spray injection and evaporation problem from the flame problem itself, so prevaporization of the liquid fuel was performed in the jet flame experiments. While Sandia's TCL has a number of established burners for different types of gas jet flames, none has a heated fuel supply line, as is required for prevaporized liquid fuels, so a vaporization system and heated fuel supply line was designed and constructed as part of a new burner. Also, the high molecular weight of kerosene fuels necessitated due consideration of the gas jet flow rate, jet diameter, and resultant flame height.

Experience derived from the TNF Workshops has shown that a jet Reynolds number of approximately 20,000 is preferable for turbulent jet flame modeling. Jets with this Reynolds number contain a sufficient level of turbulence to generate substantial turbulence-chemistry interactions, but have a minimal amount of local flame quenching. Also, for higher flow or less reactive fuels, a flame pilot is desirable to maintain an attached flame (lifted flame phenomena introduce significant difficulties in modeling). The optically accessible heights above the fuel tube in the TCL are limited to just over 0.5 m. These considerations were used to make an assessment of the proper fuel diameter to use for kerosene-type turbulent non-premixed flames.

Using a correlation for visible flame lengths [56,57], predicted visible flame heights for n-decane are shown in Fig. 4 as a function of jet Reynolds number and fuel tube diameter (when this project began, the chemical composition of the surrogate fuel had not been decided upon, so n-decane was used for the purposes of estimating flame heights). From these results, it appeared that a fuel tube diameter of less than 4 mm was desired for the kerosene fuel, in order to keep the overall flame height below 1 m.
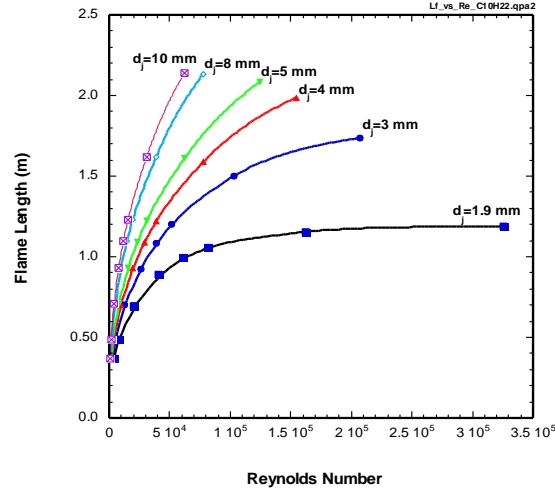
Figure 4.   Calculated visible flame length of n-decane (vapor) fueled turbulent jet flame for different fuel tube diameters.

Laser diagnostic techniques that were employed in this research included planar laser-induced fluorescence (PLIF) of hydroxyl radical (OH•) and polycyclic aromatic hydrocarbons (PAH), laser-induced incandescence (LII) of soot, particle-image velocimetry (PIV), and laser extinction/emission of soot. The PLIF measurements yield semi-quantitative, instantaneous concentrations of hydroxyl radical, the dominant oxidizing species of soot in flames (fully quantitative fluorescence measurements of concentrations is virtually impossible in soot-laden turbulent flames) and qualitative measurements of concentrations of PAH, associated with soot inception and mass growth. The PLII measurements give semi-quantitative, instantaneous measurements of soot concentration, once calibrated against laser extinction measurements in a laminar flame. Simultaneous measurements of PLII and OH• PLIF were also conducted, yielding information about the location of soot relative to the active flame zone. Similarly, simultaneous measurements of PLII and PAH PLIF gave information about the location of soot relative to regions of active fuel pyrolysis. PIV yields planar measurements of the instantaneous velocity field. In contrast to the instantaneous but discrete planar information provided by the aforementioned techniques, the laser extinction/emission technique provides time record information at a given location in the flow and is therefore useful for measuring soot-turbulence statistics. In addition, the laser extinction/emission technique yields simultaneous measurements of soot concentration and temperature. To achieve suitable spatial resolution, this technique requires the use of a small gas-purged probe that was expressly developed for this project.

In addition to the aforementioned measurements, Rayleigh scattering measurements were performed along a horizontal line, just above the burner lip, to define the thermal boundary conditions for modeling of these flames.

4.5 Pressurized Spray Combustion

Soot formation and oxidation during pressurized spray combustion was investigated in Sandia's optically accessible constant-volume combustion vessel, which has been used to study fuel jet combustion under diesel-engine-like conditions for over 15 years [58-61]. A schematic of the combustion vessel is shown in Fig. 5. The vessel has a cubic combustion chamber, 108 mm on a side. The fuel injector is mounted in a port as shown in the top-view. Optical access is provided by sapphire windows located in four other ports that permit line-of-sight and orthogonal optical access to the injected fuel jet.
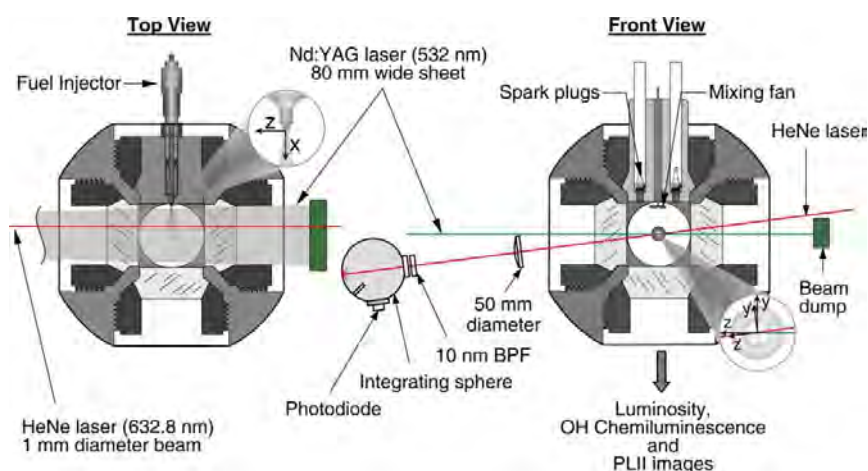
Figure 5.   Schematic of the constant-volume combustion vessel and the optical setup for soot measurements.

The preparation of the ambient gas mixture begins by filling the vessel to a specified density with a premixed, combustible-gas mixture. This mixture is then ignited with spark plugs, creating a high-temperature, high-pressure environment in the vessel. As the products of combustion cool over a relatively long time (~1 s) due to heat transfer to the vessel walls, the vessel pressure slowly decreases. When the desired temperature and pressure is reached, the fuel injector is triggered and fuel injection, autoignition, and combustion processes ensue. Throughout an experiment, the mixing fan at the top of the combustion chamber operates. This fan maintains a spatially uniform temperature environment (±2%) in the combustion vessel up to the time of fuel injection [59,60]. Fuel injection typically occurs over time periods as short as 4 ms for investigations of diesel engine combustion, but was extended to 7 ms in this study. Previous studies have shown that once the leading edge of the injection jet has passed the viewing section (typically within 2 ms), the injected jet undergoes a quasi-steady combustion process [58-61]. Therefore, with the rapid laser diagnostics employed in interrogating this combustion process, the derived information is applicable to the steady injection process characteristic of gas turbines.

The temperature, density, and composition of the ambient gas in the vessel at the time of fuel injection can be widely varied with this simulation procedure. The ambient gas temperature and pressure at injection are determined from the ambient gas pressure at the time the fuel injector is triggered and the mass of gas initially transferred into the vessel (a constant up to the time of the injection event). The ambient temperature can be varied from 1300 K down to 500 K, and the ambient pressure can be varied up to 35 MPa. For most experiments, a combustible-gas mixture of 68.1% N_2, 28.4% O_2, 3.0% C_2H_2, and 0.5% H_2 (by volume) is used. The product composition of this combustible mixture simulates air, having a composition of 21.0% O_2, 69.3% N_2, 6.1% CO_2, and 3.6% H_2O (by volume) and a molecular weight of 29.5. The JP-8 surrogate fuel was investigated in this study. Two combustion conditions were investigated: a pressure of 2.7 MPa and initial temperatures of 800–900 K, representative of jet engine takeoff conditions, and a pressure of 6.7 MPa and initial temperatures of 900–1000 K, representative of diesel engine conditions. The takeoff pressure and temperature ranges that were investigated were based on recommendations from our project monitors at Pratt & Whitney and GE Aircraft Engines. The SERDP JP-8 surrogate was investigated under the diesel engine conditions for the purpose of comparing its combustion and soot formation tendencies with those that have been previously determined in this experimental device for a range of JP-8 fuels. As the SERDP surrogate only involves two species and had not been previously investigated before this work, there was substantial interest among all of the SERDP Soot Science program members to compare its performance against actual JP-8 fuels under practically relevant combustion conditions.

Several different optical diagnostics were employed in the constant-volume combustion vessel experiments, as indicated in Fig. 5. These included line-of-sight laser extinction, PLII imaging, natural soot luminosity imaging, and OH• chemiluminescence imaging. The laser extinction technique is used for measuring the soot optical thickness across a fuel jet, while the PLII imaging is used for visualizing the spatial location of soot in a fuel jet. The spatial soot profiles, provided by PLII, and quantitative optical thickness from laser extinction are then combined to obtain soot volume fraction distributions throughout the jet. OH• chemiluminescence images were used for determining the ignition delay after the start of spray injection and the lift-off length of the combusting region of the fuel jet during its quasi-steady combustion phase. The lift-off length measurement is used to estimate the amount of air entrained into the fuel jet, and therefore the extent of partial premixing at the flame stabilization point, using a relationship developed for a 1-D model fuel jet [59,62]. This information is important for interpreting the measured amounts of soot formation, because partial premixing of the jet reduces its tendency to form soot.

4.6 Large Eddy Simulation

The baseline theoretical-numerical framework combines a general treatment of the governing conservation and state equations with state-of-the-art numerical algorithms and massively-parallel programming paradigms [63-67]. The numerical formulation treats the fully-coupled compressible form of the conservation equations, but can be evaluated in the incompressible limit. The theoretical framework handles both multicomponent and mixture-averaged systems, with a generalized treatment of the equation of state, thermodynamics, and transport processes. It can accommodate high-pressure real-gas/liquid phenomena, multiple-scalar mixing processes, finite-rate chemical kinetics and multiphase phenomena in a fully coupled manner. For LES applications, the instantaneous conservation equations are filtered and models are applied to

account for the subgrid-scale (SGS) mass, momentum and energy transport processes. The baseline SGS closure is obtained using the mixed dynamic Smagorinsky model by combining the models of Erlebacher et al. [68] and Speziale [69] with the dynamic modeling procedure [70-72] and the Smagorinsky eddy viscosity model [73]. There are no tuned constants employed anywhere in the closure. The property evaluation scheme is derived using the extended corresponding states model [74,75] and designed to handle multicomponent systems. The scheme has been optimized to account for thermodynamic nonidealities and transport anomalies over a wide range of pressures and temperatures.

The numerical framework provides a fully-implicit all-Mach-number time-advancement using a fully explicit multistage scheme. A unique dual-time approach is employed with a generalized (pseudo-time) preconditioning methodology that treats convective, diffusive, geometric, and source term anomalies in an optimal manner. The implicit formulation allows one to set the physical-time step based solely on accuracy considerations. The spatial differencing scheme is optimized for LES using a staggered grid arrangement in generalized curvilinear coordinates. This provides non-dissipative spectrally clean damping characteristics and discrete conservation of mass, momentum and total-energy. The scheme can handle arbitrary geometric features, which inherently dominate the evolution of turbulence. A Lagrangian-Eulerian formulation is employed to accommodate particulates, sprays, or Lagrangian based combustion models, with full coupling applied between the two systems. The algorithm is massively-parallel and has been optimized to provide excellent parallel scalability attributes using a distributed multiblock domain decomposition with a generalized connectivity scheme. Distributed-memory message-passing is performed using Message Passing Interface (MPI) and the Single-Program—Multiple-Data (SPMD) model. It accommodates complex geometric features and time varying meshes with generalized hexahedral cells while maintaining the high accuracy attributes required for LES. The numerical framework has been ported to all major platforms and provides highly efficient fine-grain scalability attributes. Sustained parallel efficiencies above 90-percent have been achieved with jobs as large as 4096 processors on the National Energy Research Scientific Computing Center (NERSC) IBM SP platform (Seaborg). The code is fully vectorized and has been optimized for both vector and commodity architectures.

Our combustion modeling approach for the high-fidelity LES facilitates direct treatment of turbulence-chemistry interactions and multiple-scalar mixing processes without the use of tuned model constants. The systematic development and validation of this approach is currently a major focal point. Unlike conventional models, chemistry (and the associated mechanisms developed under this grant) is treated directly within the LES formalism. The filtered energy and chemical source terms are closed by employing a moment-based reconstruction methodology that provides a modeled representation of the local instantaneous scalar field. Model coefficients are evaluated locally in closed form as a function of time and space using the dynamic modeling procedure. In the limit as the grid resolution and time-step approach the smallest relevant scales, contributions from the subgrid-scale models approach zero and the limit of a direct numerical simulation (DNS) is achieved.

All of the subgrid-scale models for combustion developed to-date are relatively simple due to past computational limitations and the long-standing requirement of fast turnaround times for calculations. Approaches aimed at obtaining accurate closure schemes include the assumption of fast chemistry, the assumption of laminar flamelets, the conditional moment closure (CMC), and

PDF transport models. Klimenko has established the relation between CMC and unsteady flamelets [76]. There are several limitations associated with each of these approaches, and each exhibit clear trade-offs between model accuracy and the validity of the modeling assumptions. More recently, a new class of reconstruction subgrid-scale models has been proposed that combine the purely mathematical approximate deconvolution procedure with physical information from an assumed scalar spectrum to match specific scalar moments [77,78]. Approximate reconstruction using moments provides an alternative approach that avoids the intermediate step of modeling the joint-PDF associated with subgrid-scale fluctuations. The instantaneous scalar field is estimated using an approximate deconvolution operation that requires the filtered moments of respective scalars to match to a specified order. The estimated scalar field is then used as a surrogate for the exact scalar field to calculate the subgrid-scale contribution and the additional set of derived coefficients can be obtained in a consistent manner using the dynamic procedure. Research to-date suggests that this method cannot be reliably used to close the filtered chemical source terms directly. It has been shown, however, that it can be used to obtain highly accurate representations of polynomial nonlinearities associated with terms such as subgrid-scale scalar variances.

Here, we extend the approach described above by using the highly accurate representations of the subgrid-scalar scalar variances and coupling this to a stochastic reconstruction methodology to obtain a modeled representation of the instantaneous scalar field. This, in turn, is used to obtain accurate representations of the filtered chemical source terms. The approach allows one to track the evolution of multiple scalars in both time and space and accounts for finite-rate chemistry in a time-accurate manner.

A focal point of our effort under this grant is to incorporate a suitable radiation model closure and to incorporate a method-of-moments soot model into the LES framework. Soot particulates are treated both directly in the Eulerian frame and also using a Lagrangian particle model to simulate a statistically relevant sample of soot ―parcels". This model is directly coupled to an appropriately reduced chemical mechanism that accounts for the instantaneous production soot particles, subject to nucleation from the gas phase and coagulation in the free molecular regime.

5.0 Results and Accomplishments

Substantial accomplishments were achieved in all 4 major project tasks: development of chemistry and soot models, evaluation of JP-8 surrogate performance during pressurized spray combustion, measurement of soot and flame properties in turbulent non-premixed jet flames, and large eddy simulation of turbulent non-premixed jet flames. The results of work in each of these project areas is described under the appropriate subheadings below.

5.1 Soot Chemistry Model

5.1.1 Development and Validation of Ethylene Chemical Kinetic Mechanism

A new, detailed chemical kinetic model for ethylene combustion, including the chemistry of PAH formation, was developed. The model is based on USC-Mech II for C1-C4 hydrocarbon combustion [79]. In collaboration with Meredith Colket of United Technologies Research Center (UTRC), a set of PAH chemistry was added to the base hydrocarbon combustion model. The result is a detailed reaction model (currently called SERDP v0.1), which contains 170 species and 1002 chemical reactions. The model was validated against a large set of experimental data including laminar flame speeds, shock tube ignition delay, species profiles in flow reactors, species profiles in shock tubes (as a function of temperature), and species profiles in premixed flat flames. In additional, comparisons were made against existing, state-of-the-art reaction models for ethylene combustion. In general, the new mechanism shows good agreement with the experimental data and is superior to previous mechanisms. Examples of the comparison of the new SERDP mechanism with the data and with competing ethylene mechanisms are shown in Figs. 6 and 7. The complete results of the model validation study are presented in ref. 81. Based on the favorable comparisons with the available experimental data, SERDP v0.1 was accepted by consensus as the base ethylene combustion model for this and other SERDP Soot Science research teams modeling ethylene combustion.
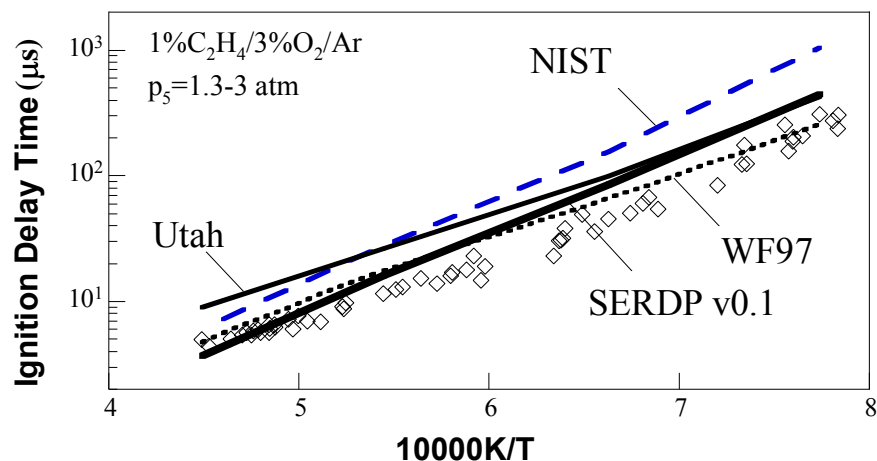
Figure 6.   Experimental (symbols) and computed (lines) ignition delay times behind reflected shock waves. Experimental data are taken from ref. 80. The ignition is measured by the onset of CH* chemiluminescent emission.

17
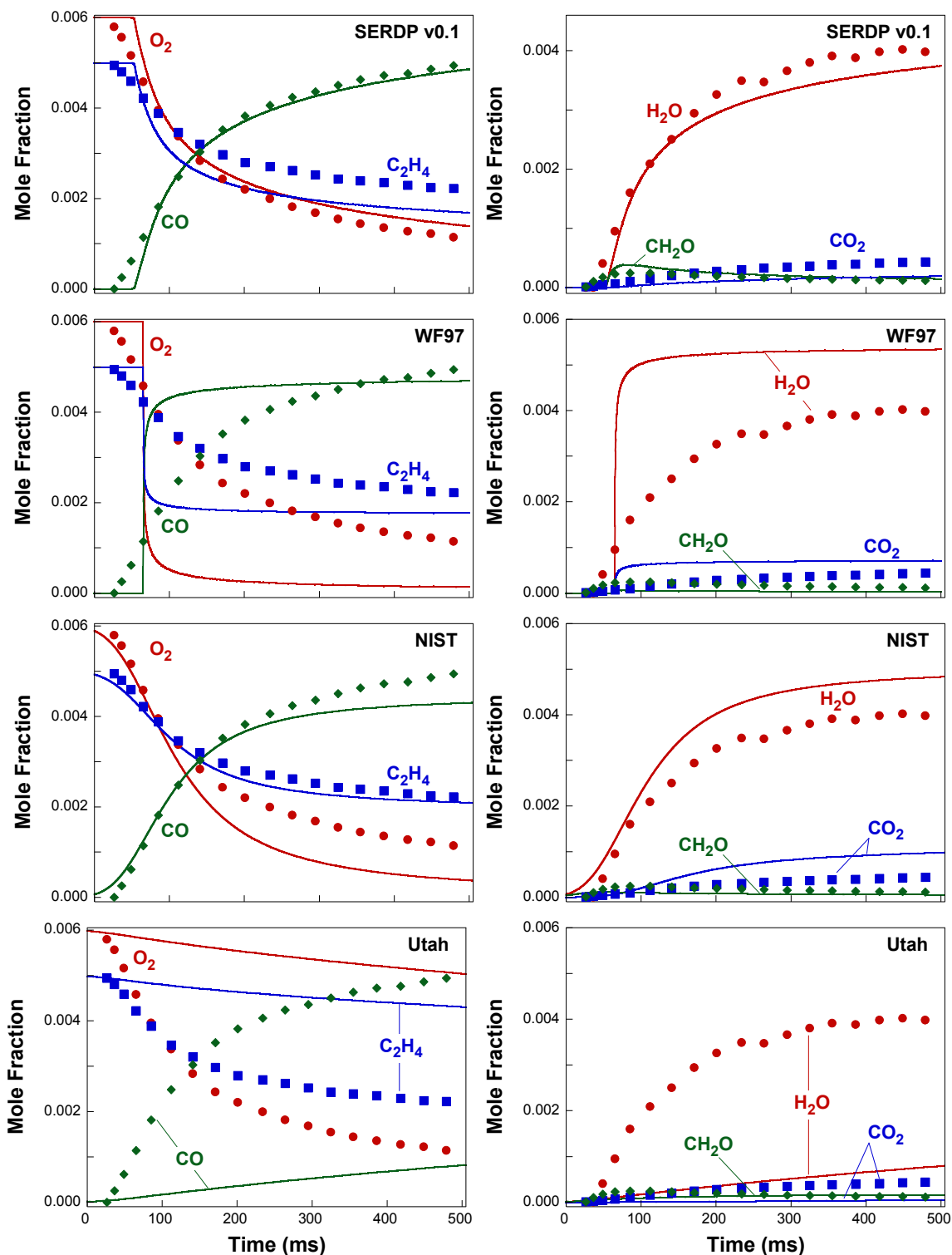
Figure 7.   Experimental (symbols) and computed (lines) species profiles during ethylene oxidation in a flow reactor at a pressure of 5 atm and temperature of 950 K. Computed profiles are time-shifted (SERDP v0.1: -40 msec; WF97: -0.5 sec; NIST: -1.1 sec; Utah: -1.2 sec) to match experimental data.

5.1.2 Development of a Detailed Chemical Kinetic Mechanism for the SERDP JP-8 Surrogate

Following the successful development and validation of the detailed chemical kinetic model for ethylene combustion, a chemical kinetic model was constructed for the SERDP JP-8 surrogate, in collaboration with Med Colket at UTRC. This model is composed of three components: USC Mech II as the kinetic foundation for $H_2/CO/C_1$-C_4 hydrocarbon oxidation [79], JetSurF 1.0 for n-dodecane combustion [39], and the Battin-Leclerc model [40] for *m*-xylene combustion. As shown in Fig. 8, the model does quite well in predicting the combustion behavior of n-dodecane. However, comparisons with existing data for m-xylene combustion are not very promising, especially with respect to laminar flame speeds, as shown in Fig. 9. The current SERDP program research being conducted by Ken Brezinsky at UIC is, in part, devoted to developing an improved chemical kinetic model for m-xylene combustion.
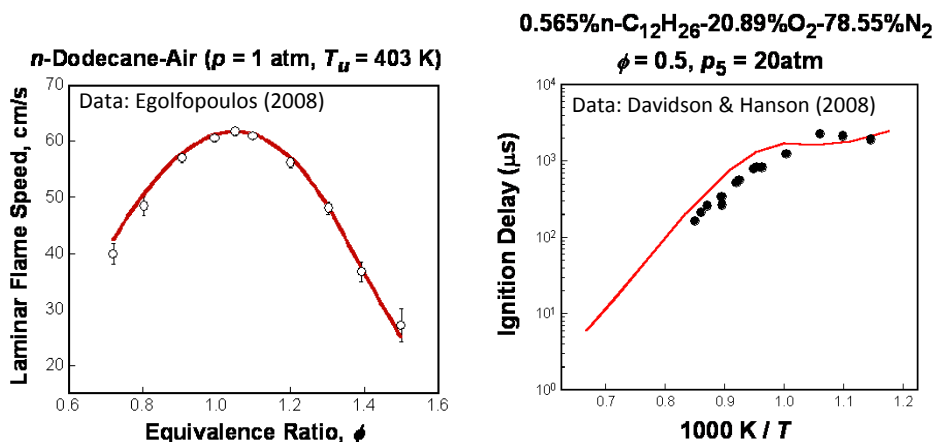
Figure 8.   Comparison of experimental n-dodecane-air flame speed measurements [39] (left) and ignition delay measurements [82] (right) with predictions from the detailed chemical kinetic model for SERDP JP-8 surrogate.
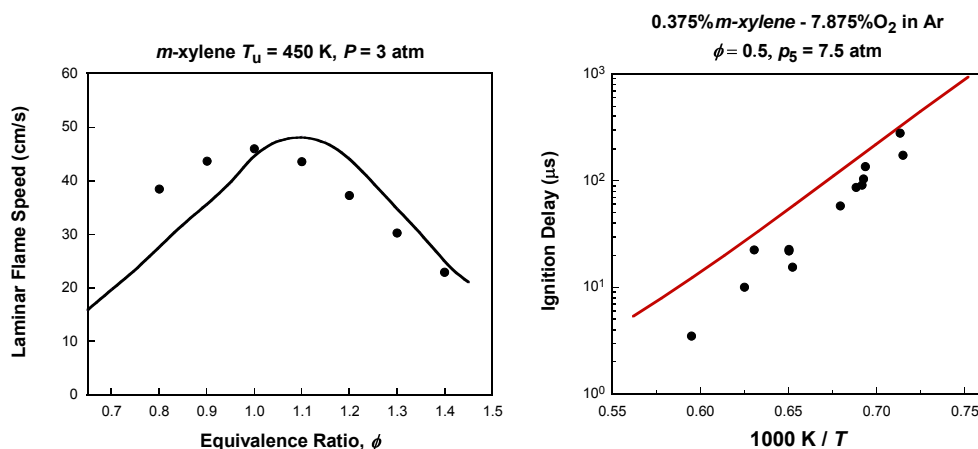
Figure 9.   Comparison of experimental m-xylene-air flame speed measurements [83] (left) and ignition delay measurements [40] (right) with predictions from the detailed chemical kinetic model for SERDP JP-8 surrogate.

19

To assist in the development of a suitable m-xylene model, a study was undertaken of the product branching ratio of the important O + benzene reaction step. This reaction step is an important part of a benzene reaction model that, together with a toluene reaction model, is a subcomponent of the m-xylene model. The reaction proceeds mainly through the addition of the O atom to benzene, forming an initial triplet diradical adduct, which can either dissociate to form the phenoxy radical and H atom, or undergo intersystem crossing onto a singlet surface, followed by a multiplicity of internal isomerizations, leading to several possible reaction products. In collaboration with Craig Taatjes at Sandia National Laboratories, the product branching ratios were examined over the temperature range of 300 to 1000 K and pressure range of 1 to 10 Torr (0.13 – 1.3 kPa). The reactions were initiated by pulsed-laser photolysis of NO_2 in the presence of benzene and helium buffer in a slow-flow reactor, and reaction products were identified by using the multiplexed chemical kinetics photoionization mass spectrometer operating at the Advanced Light Source (ALS) of Lawrence Berkeley National Laboratory. Phenol and phenoxy radical were detected and quantified. Cyclopentadiene and cyclopentadienyl radical were directly identified for the first time. Finally, ab initio calculations and master equation/RRKM modeling were used to reproduce the experimental branching ratios, yielding pressure-dependent rate expressions for the reaction channels, including phenoxy + H, phenol, cyclopentadiene + CO, which are proposed for kinetic modeling of benzene oxidation. Details are provided in ref. 84.

5.2 Reduction of Ethylene Chemical Kinetic Mechanism

The detailed chemical kinetic model for combustion and pyrolysis of ethylene that was described in the previous section was reduced to 17 species using a two-step process. First, the full ethylene mechanism (with 1002 reactions involving 170 species) was reduced to a skeletal mechanism using the Level of Importance (LOI) method [51]. Skeletal mechanisms with different degrees of reduction were evaluated by comparing the reduced model predictions of hydroxyl radical concentrations in an adiabatic perfectly stirred reactor (PSR) to the uncertainty bands of the full model (determined via a spectral expansion method). With this methodology, it was determined that one could reduce the mechanism to 30 species in the skeletal model and still keep within the uncertainty bands for hydroxyl in the active reaction stage (i.e. for residence times greater than 10 μs in the PSR simulations shown in Fig. 10). Having reduced the skeletal model as far as possible via LOI, it was reduced a final step using the quasi-steady state (QSST) approach. This reduced the final mechanism to 17 species, suitably small for inclusion in LES calculations.

5.3 Flat Flame Measurements

5.3.1 Measurement of Soot PSDFs for Different Flame Temperatures

The evolution of the soot particle size distribution function (PSDF) and particle morphology were studied for premixed ethylene-oxygen-argon flat flames at a common equivalence ratio $\phi =$ 2.07 over a range of maximum flame temperatures. Experiments were carried out using an in situ probe sampling method in tandem with a scanning mobility particle sizer (SMPS), yielding the PSDF for various distances from the burner surface. Within the particle size range that can be detected, the PSDF transitions from an apparent unimodal PSDF for high temperature flames (T_f > ~1800 K) to a bimodal PSDF at lower temperatures (T_f < ~1800K). The two extremes in
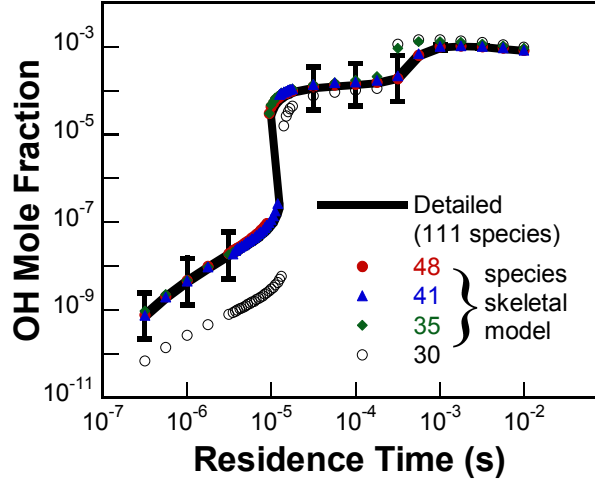
Figure 10. Test of skeletal models in adiabatic PSR. The error bars are the uncertainty of the detailed model and were determined by a spectral expansion method [81].

PSDFs are shown in Figs. 11 and 12. The bimodal PSDFs have a noticeable trough that separates the nucleation and coagulation modes of particle growth. This mode-transition trough had been previously thought to occur at a fixed particle size, but these results show a continuous shift of the trough location towards smaller sizes with increasing flame temperature. The morphology of the particles was examined by transmission electron microscopy (TEM) and atomic force microscopy (AFM). TEM images show the particles are spherical, even when the PSDF is bimodal, suggesting that the bimodality occurs as the primary particles grow by coagulation, and
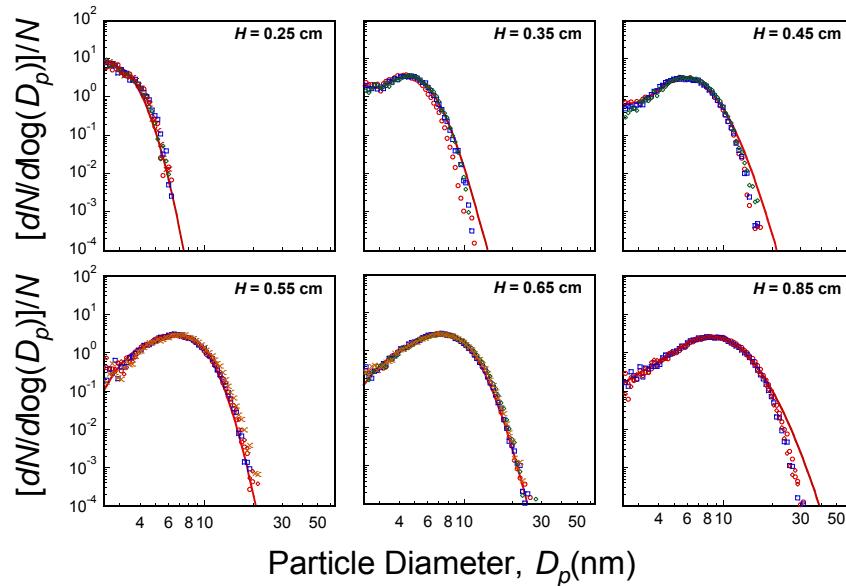
Figure 11. Evolution of PSDFs measured for ethylene flat flame with a maximum temperature of 1900 K. Symbols are experimental data and lines are fits to data using a bi-lognormal distribution function.

21
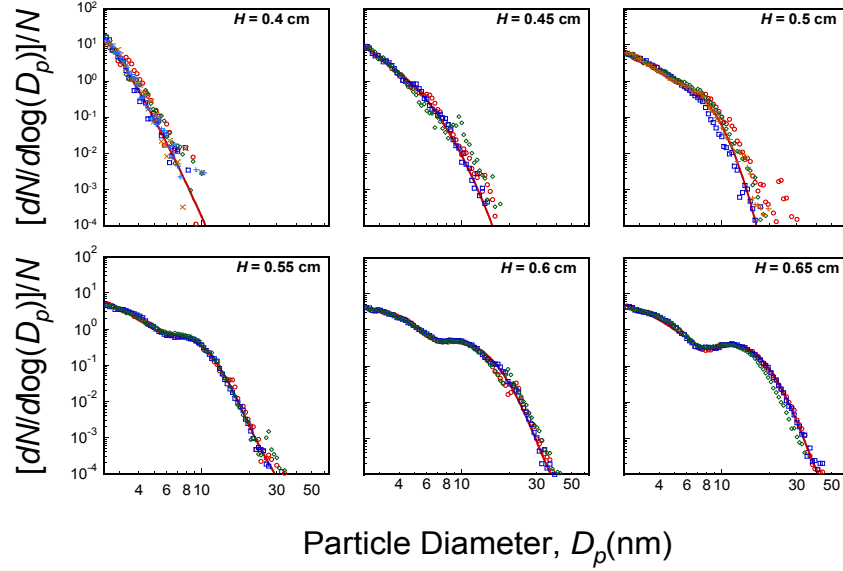
Figure 12.   Evolution of PSDFs measured for ethylene flat flame with a
maximum temperature of 1660 K. Symbols are experimental data
and lines are fits to data using a bi-lognormal distribution function.

is not a result of particle aggregation. AFM of substrate-deposited particles shows that particles spread and form hill-like structures upon impact with the substrate surface, indicating they are liquid-like at the time of impact (see Fig. 13). Additional details are presented in ref. 85.
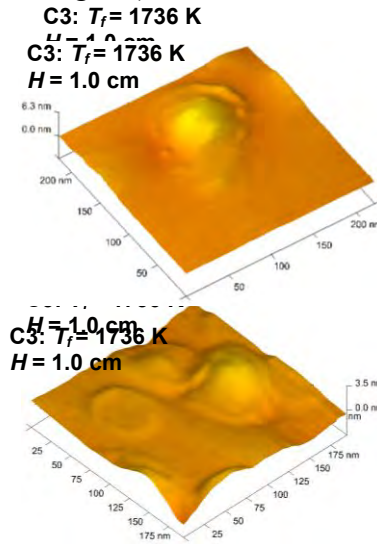
Figure 13.   AFM images of soot collected from an ethylene flat flame
with a maximum temperature of 1740 K.

5.3.2 Measurement of Soot PSDFs for Benzene-Doped Ethylene Flames

Particle size distribution functions of nascent soot were studied in a spatially resolved manner by online sampling/scanning mobility particle sizer in two burner-stabilized, premixed ethylene–oxygen–argon flames with two different levels of benzene doping, amounting to up to 1/3 of the

22

total fuel carbon. Particle morphology was analyzed by atomic force microscopy (AFM) of substrate-deposited samples. An aerosol electrometer was introduced to extend the lower detection limit to 1.6 nm in diameter. The results show that the bimodal behavior of particle size previously observed for neat ethylene fuel is also applicable to the benzene-doped flames studied. The variation of the size distribution from flame to flame is conclusively attributed to flame temperature variation. Under the condition of an equal carbon concentration, benzene doping leads to negligible changes in the characteristics of the size distribution. For all flames studied, AFM observations show that nascent soot is liquid-like and spreads extensively upon impact on a substrate surface. Further details are provided in ref. 86.

5.3.3 Development of an Improved Soot Probe Technique for Premixed Flat Flames

A burner-stabilized, stagnation flame technique was developed, to improve comparisons between modeling and experiments in premixed flat flames. In this technique, the previously developed sampling probe is combined with a water-cooled circular flame stabilization plate such that the combination simultaneously acts as a flow stagnation surface and soot sample probe for mobility particle sizing. The technique provides a rigorous definition of the boundary conditions of the flame with probe intrusion and enables less ambiguous comparison between experiment and model. Tests on a 16.3% ethylene–23.7% oxygen–argon flame at atmospheric pressure show that, with the boundary temperatures of the burner and stagnation surfaces accurately determined, the entire temperature field may be reproduced by pseudo one-dimensional stagnation reacting flow simulation (see Fig. 14). Soot particle size distribution functions were determined for the burner-stabilized, stagnation flame at several burner-to-stagnation surface separations. It was found that the tubular probe developed earlier perturbs the flow and flame temperature in a way that is better described by a one-dimensional stagnation reacting flow than by a burner-stabilized flame free of probe intrusion. Further details are provided in ref. 87.

5.3.4 Measurement of Soot PSDFs for n-Dodecane Flames

n-Dodecane is an important component of jet fuel surrogate. We experimentally investigated the evolution of particle size distribution of incipient soot formed in laminar premixed n-dodecane-oxygen-argon flames. The flames were established on a porous flat flame burner with an equivalence ratio of 2 and a maximum flame temperature around 1800 K. Detailed particle size distributions were obtained by the burner-stabilized stagnation-flow (BSSF) sampling approach using a nano-scanning mobility particle sizer and are shown in Fig. 15. The flame temperature profiles were determined for each separation distances between the burner surface and stagnation surface/probe orifice. As the size distributions are obtained using the recently developed BSSF approach, it was shown that the flames can be modeled using an opposed jet flame code without having to estimate the effect of probe perturbation. The measured and simulated temperature profiles show good agreement. The evolution of the soot size distributions for n-dodecane flames was found to be similar to that obtained from ethylene flames. The size distributions are characteristically bimodal indicating strong, persistent nucleation over a large range of residence times in the flame. Under similar conditions, the nucleation mode in the n-dodecane flames is stronger than that in the ethylene flames. Further details are provided in ref. 88.
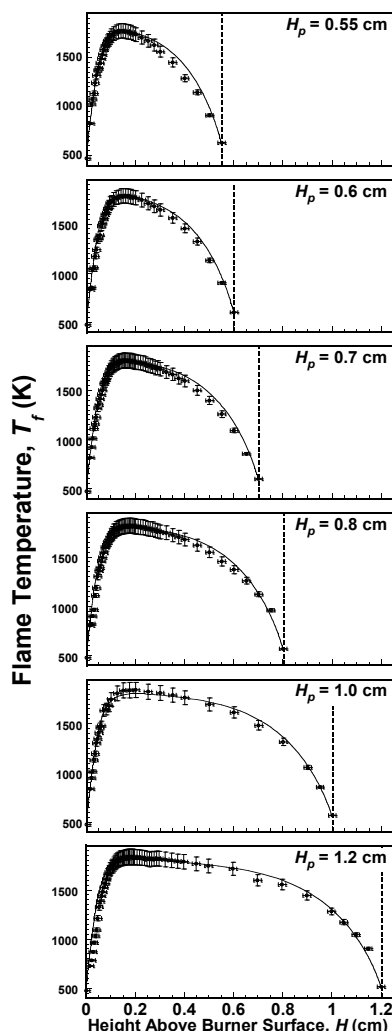
Figure 14. Comparison of measured and radiation corrected gas temperature (symbols) and calculated temperature profiles in an ethylene flame as a function of distance from the burner surface. The sampling plate position relative to the burner surface is marked by the dashed lines. The computation assumes a stagnation flow field.

5.3.5 *Measurement of Aliphatic Compounds in Flat Flame Soot*

Previous studies suggest that soot formed in premixed flat flames can contain a substantial amount of aliphatic compounds. The presence of these compounds may affect the kinetics of soot mass growth and oxidation in a way that is currently not understood. Using an infrared spectrometer coupled to a microscope (micro-FTIR), we examined the composition of soot sampled from a set of ethylene-argon-oxygen flames we recently characterized [85], all with an equivalence ratio $\phi = 2.07$ but varying in maximum flame temperatures. Soot was sampled at three distances above the burner surface using a probe sampling technique and deposited on silicon nitride thin film substrates using a cascade impactor. Spectra were taken and analyses

24
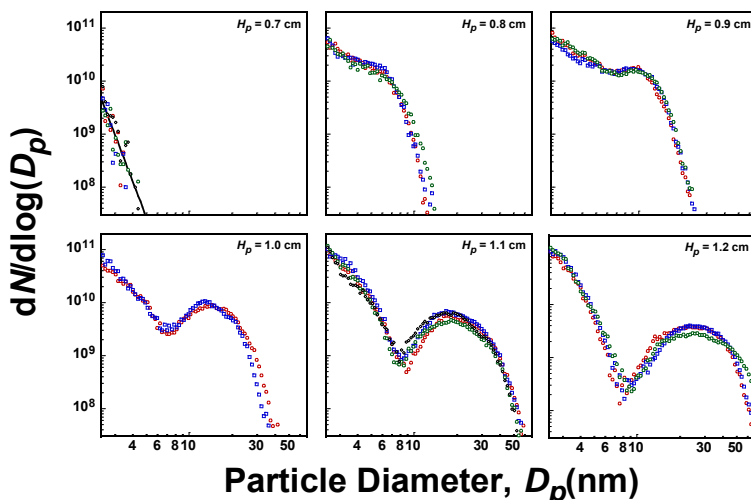
Figure 15.   Repeat measurements of the evolution of PSDFs in an n-dodecane
flat flame with a maximum temperature of 1660 K.

performed for samples collected on the lowest five impactor stages with the cut-off sizes of $D_{50} =$ 10, 18, 32, 56 and 100 nm. The micro-FTIR spectra revealed the presence of aliphatic C-H, aromatic C-H and various oxygenated functional groups, including carbonyl (C=O), C-O-C and C-OH groups. Spectral analyses were made to examine variations of these functional groups with flame temperature, sampling position and particle size. Results indicate that increases in flame temperature leads to higher contents of non-aromatic functionalities. Functional group concentration was found to be ordered as follows: [C=O] < [C-O] < [aliphatic C-H]. Aliphatic C-H was found to exist in significant quantities, with very little oxygenated groups present. The ratio of these chemical functionalities to aromatic C-H remains constant for particle sizes spanning 10-100 nm. The results confirm a previous experimental finding: a significant amount of aliphatic compounds is present in nascent soot formed in the flames studied, especially towards larger distances above the burner surface. Further details are provided in refs. 89 and 90.

5.4 Turbulent Non-Premixed Flame Measurements

5.4.1 Ethylene TNF Burner Development

An existing burner at Sandia, known as the —½scale Sydney burner," was installed in the Turbulent Combustion Laboratory (TCL) and used to support ethylene flames burning in coflowing air. This entailed the installation of appropriate air conditioning screens to yield a fully conditioned coflow that matched conditions typically used in the Turbulent Nonpremixed Flame (TNF) Workshop series flames that have been extensively modeled and demonstrated to have good flow boundary conditions. The pilot flame for this existing burner was observed to be spatially uneven and to have variable flame conditions over time. Furthermore, as the jet Reynolds number was increased to 20,000 and higher, a hole was observed to form in the flame on one side just above the fuel tube. This hole increased in size as the jet fuel velocity increased. Comparisons of the pilot flame design with the full-sized Sydney burner that has been extensively utilized in TNF flame studies revealed that the ½-scale burner had an undersized and poorly constructed pilot flame area, consisting of a single row of irregularly drilled pilot flames,

compared to the three interwoven, machine-drilled concentric rows for the full-sized Sydney burner (see Fig. 16). To correct for these deficiencies, it was decided to design and construct a new burner that featured a pilot flame design similar to the Sydney burner design, but with a smaller diameter fuel tube appropriate for use with ethylene.

Figure 16.   Photographs of the pilot flames for the —½scale Sydney burner,"
on the left, and the actual full-scale Sydney burner, on the right.

While the ½-scale Sydney burner was installed, scoping studies were conducted to determine the overall characteristics of turbulent ethylene jet flames. First, it was determined that a pilot flame is required to avoid flame lift-off for reasonably high Reynolds numbers (Re ≥ 15,000). Flame lift-off is undesirable in the current study, as it complicates modeling efforts and makes comparisons of soot formation modeling with data more difficult to interpret. Evaluation of the ethylene flame height as a function of Reynolds number showed that the flame was approximately 1 meter in height and the flame height increased slowly with increasing jet Re. OH PLIF images of the near-burner high shear region where flame quenching first occurs revealed that local extinction begins to occur for a jet Re ~ 20,000, as shown in Fig. 17.
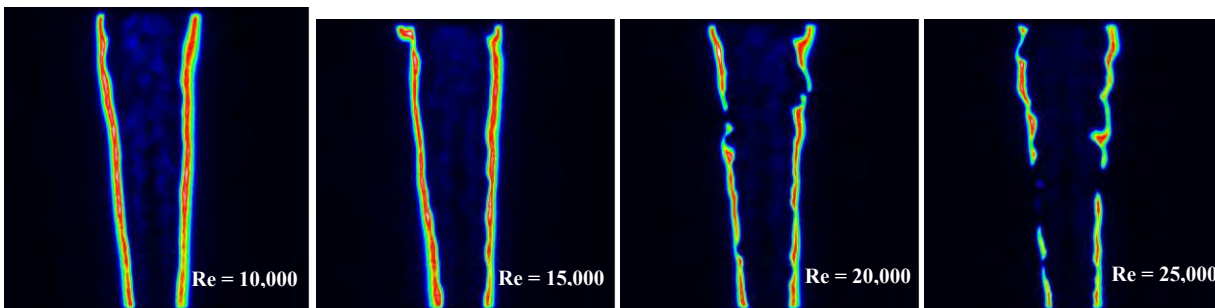
Figure 17.   PLIF images of OH• over heights of x/D from 2.3 to 15.6 (i.e. from x = 8.7 mm
to x = 58.8 mm) for four different ethylene jet flow velocities, corresponding to
Re = 10,000 to 25,000, on the ½-scale Sydney burner. The light blue inner
structures evident in interior regions of the flame arise from PAH PLIF.

Based on considerations of flame height, available polished tube diameters, and the estimated Re at which local flame extinction was likely to begin to occur, it was decided to construct a new burner for ethylene jet flames with a fuel tube ID of 3.2 mm (compared to 3.8 mm for the ½-scale Sydney burner). In addition, type 304 stainless steel was chosen for the burner material. Photographs of the burner and the pilot plate design are shown in Fig. 18. Tests with the new burner demonstrated good flame attachment for the ethylene jet flame for Re > 30,000, even when using an ethylene/air pilot flame with a heat release rate that was only 2% of that of the

main fuel jet. Fast-shutter digital photographs (revealing the degree of flame wrinkling) of the ethylene jet flames stabilized on the new burner are shown in Fig. 19. For a target flame of Re = 20,000, this burner produced a flame with a height of less than 900 mm, which was accessible with our burner translation system.
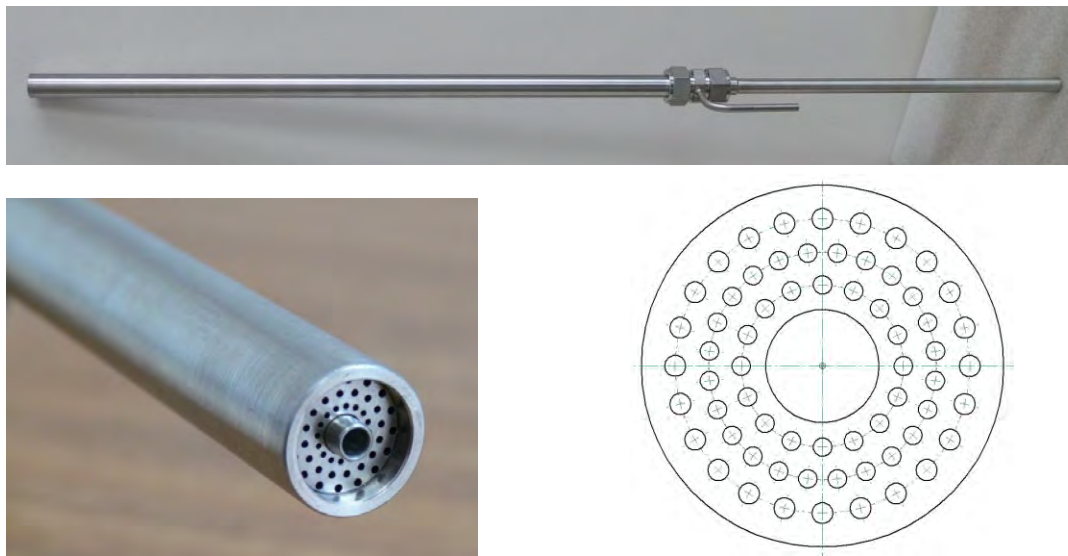
Figure 18. Photographs of the complete ethylene burner assembly (top) and burner face (left). The pilot plate design with three concentric rows of pilot flames that provide uniform heating is shown to the right.

Line Rayleigh imaging was performed with a 532 nm doubled YAG beam just above the burner lip (5 mm downstream) to quantify the thermal boundary condition provided by the pilot flame and to validate the uniformity of flow through the pilot. As shown in Fig. 20, the pilot flame indeed performed well and provided a uniform thermal boundary condition for use with CFD modeling. The temperature profile could not be computed through the active flame region because of uncertainties over the local Rayleigh scattering cross-section of the chemical species mix in these areas. Further details concerning the burner development process are documented in ref. 91.

5.4.2 *Surrogate JP-8 Fuel Vaporization and TNF Burner Development*

To utilize a liquid fuel, such as the SERDP JP-8 surrogate fuel, in a turbulent non-premixed jet flame, without adding additional modeling complications associated with spray development and evaporation, a liquid fuel vaporizer and heated vapor transport line needed to be constructed. A schematic of the liquid fuel handling system design that was adopted is shown in Fig. 21. This

Re = 10,000   20,000   30,000
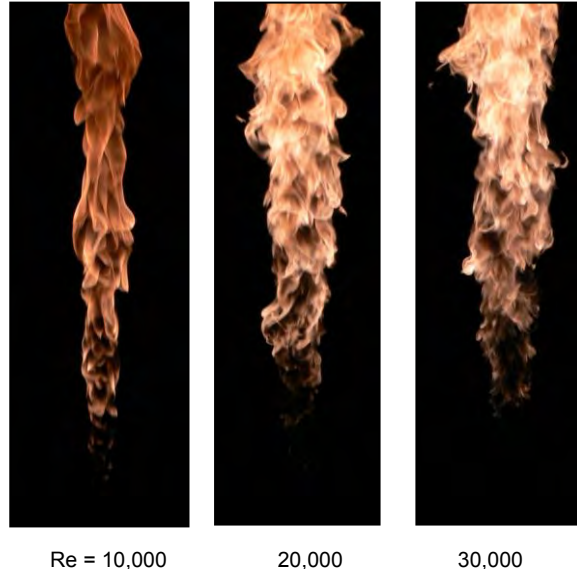
Figure 19.   Fast-shutter (1/1600 s) photographs of ethylene jet
flames stabilized on the new jet flame burner.
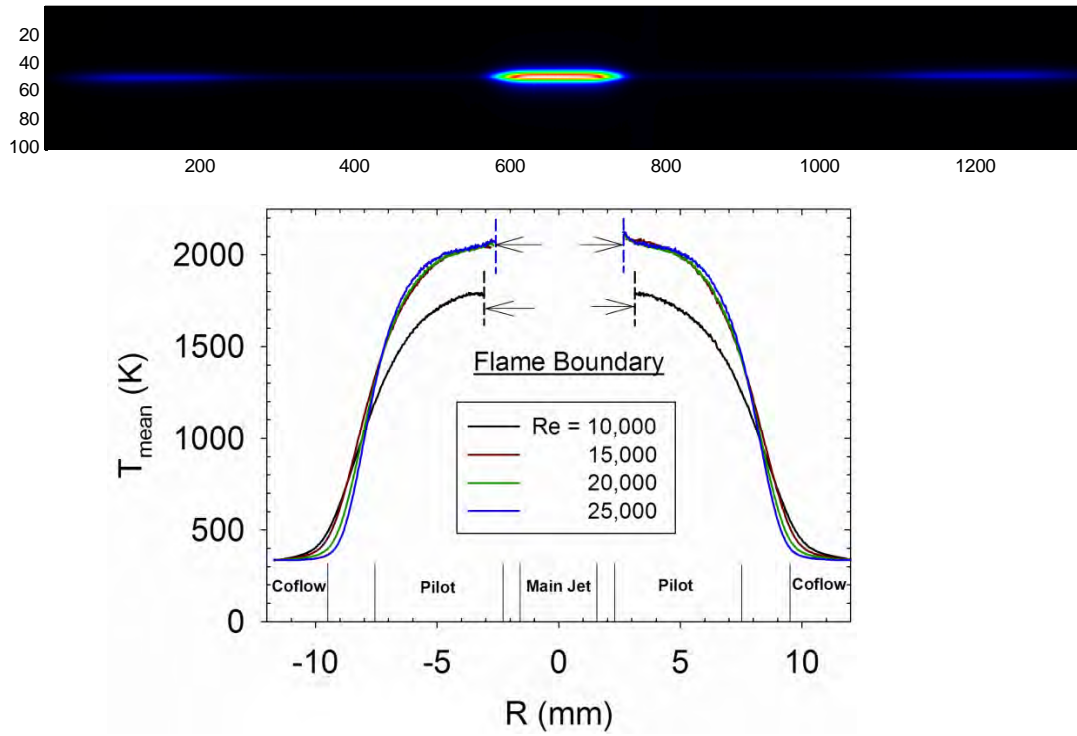
Figure 20.   Sample Rayleigh scattering image (top) and derived temperature field (bottom), up
to the flame boundary, 5 mm downstream from the burner lip. The anomalous
profile for Re = 10,000 results from the nonlinear response of a mass flow
controller for the pilot flame when used near its lower flow limit.

system consists of a fuel tank, a metering pump, to allow fine control of the liquid flow rate, a liquid accumulator (not shown in the diagram), downstream of the pump, to dampen out pump oscillations, a hollow-cone diesel spray nozzle, to provide fine fuel atomization, and a heated vaporizer. To assist in rapid vaporization of the fuel spray and minimize or eliminate droplet carryover from the vaporizer, the vaporizer was constructed with embedded aluminum fins, as shown in Fig. 22. Fig. 23 shows a photograph of the vaporizer. To verify that the vaporization process did not introduce any distillation or thermal cracking of the SERDP JP-8 surrogate fuel, the vaporized fuel was recondensed and analyzed by mass spectrometry. Only the original fuel mass spectral peaks associated with n-dodecane and m-xylene were present in the recondensed sample (thereby showing no indication of thermal cracking, which would have resulted in lower and upper mass spectral peaks) and the peak area ratio agreed with that in the original fuel (thereby showing no evidence of distillation effects).
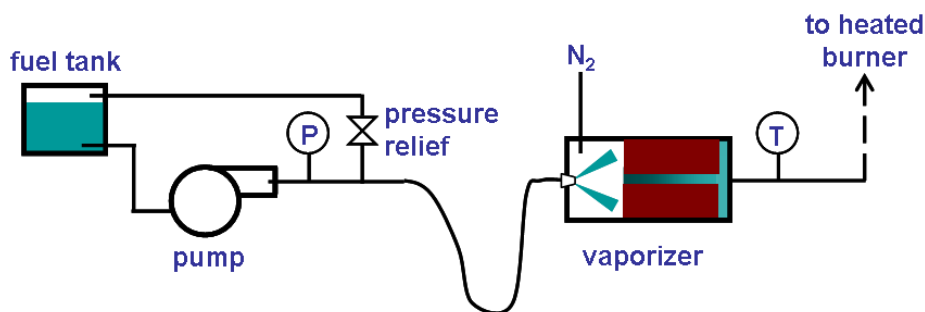
Figure 21.   Schematic of liquid fuel handling and vaporization system.
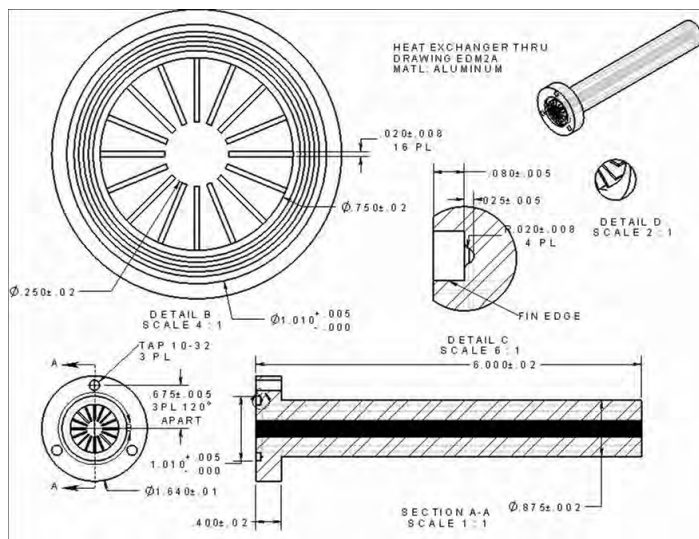
Figure 22.   Design drawing of finned aluminum heat exchanger for
rapid vaporization of fuel spray.

A burner with a similar design as the ethylene burner, but with a smaller fuel tube diameter (2.5 mm ID) and with a heated fuel line, was designed and constructed. As with the ethylene burner, the pilot flame was fed with a slightly lean ($\phi = 0.95$) ethylene/air mixture, at a flow rate corresponding to 2% of the heat release rate of the main fuel jet. Fig. 24 shows a photograph of

the base of the heated burner when supporting a SERDP JP-8 surrogate flame. Further details concerning the liquid fuel handling, vaporization, and delivery system are documented in ref. 91.

Figure 23. Photograph of liquid fuel vaporizer, with externally clamped electrical heaters. The side port tubing is for nitrogen purging of the system.
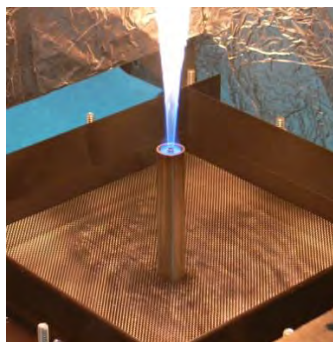
Figure 24. Photograph of the flame base of SERDP JP-8 surrogate TNF flame.

5.4.3 Simultaneous OH• PLIF and Planar LII

As suggested by Fig. 17, interrogation of OH• PLIF images in the high-shear near-burner region of ethylene jet flames showed occasional local extinction for a jet Reynolds number of 20,000, and more frequent extinction events at higher Re. Based on the judgments of Dr. Robert Barlow (principal organizer of the TNF workshops) and Dr. Joseph Oefelein, the extinction events at Re = 20,000 are infrequent enough to avoid affecting the downstream flame structure and therefore posing a problem for flame modeling that doesn't treat local extinction and reignition. Conversely, the Re = 15,000 flame was judged to lack sufficient turbulent characteristics to be desirable as a target flame for experiments and modeling. Consequently, the Re = 20,000 flame was chosen to be the canonical ethylene flame for detailed characterization. The mean gas exit velocity for this flame is 55 m/s.

Simultaneous OH• PLIF and LII imaging were performed both in this canonical ethylene jet flame and in a JP-8 surrogate flame with the same calculated fuel jet Reynolds number. Diagnostic details are provided in ref. 88. Figure 25 shows the process by which overlay images of OH and soot were produced and gives four examples of the instantaneous planar distribution of soot and OH• in a particular location within the ethylene flame. At this height, OH• exists as continuous layers and its presence serves as a marker of the stoichiometric flame zone. Soot is

largely confined within the inner edge of OH•, with occasional penetrations into the high-temperature flame zone. The soot layers display vortex-like features, which isn't surprising because, as a result of its non-diffusive nature, soot largely follows the local streaklines (except for the influence of thermophoresis in low-strain regions). This characteristic of soot does mean that at least qualitative information regarding the velocity field is provided by the soot layer imaging.
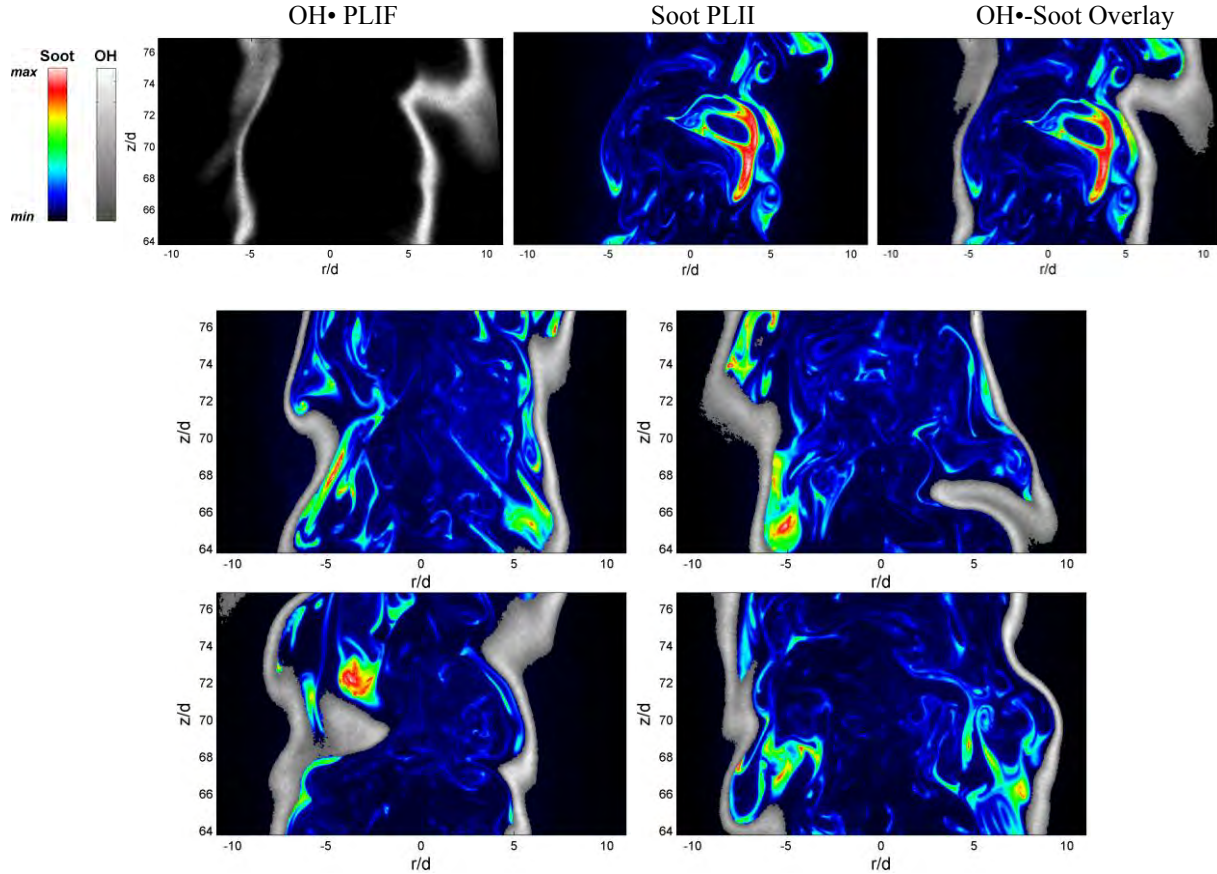
Figure 25.   Instantaneous distribution of soot and OH• in a turbulent non-premixed ethylene jet flame, as revealed by simultaneous LII and OH PLIF imaging. False-color structures are from the LII images, on which have been overlaid OH• structures, in an inverted grayscale. z and r designate the axial and radial coordinates.

The evolution of OH• and soot with height of the flame is shown in Fig. 26. Marching downstream from the jet exit, OH• structures evolve from straight, thin layers near the nozzle to increasingly wrinkled, thick structures. Local flame extinction occasionally occurs at heights from 50 mm to 100 mm, where the strain rate is expected to be high. Measurable soot starts to appear 80 mm downstream as localized streaks or pockets before becoming thick and interconnected downstream in the flame. Up to 300 mm downstream, soot is primarily contained within the OH• layer (or flame sheet); beyond that, fuel-rich soot structures are 'penetrated' by OH• and eventually form isolated islands.

31
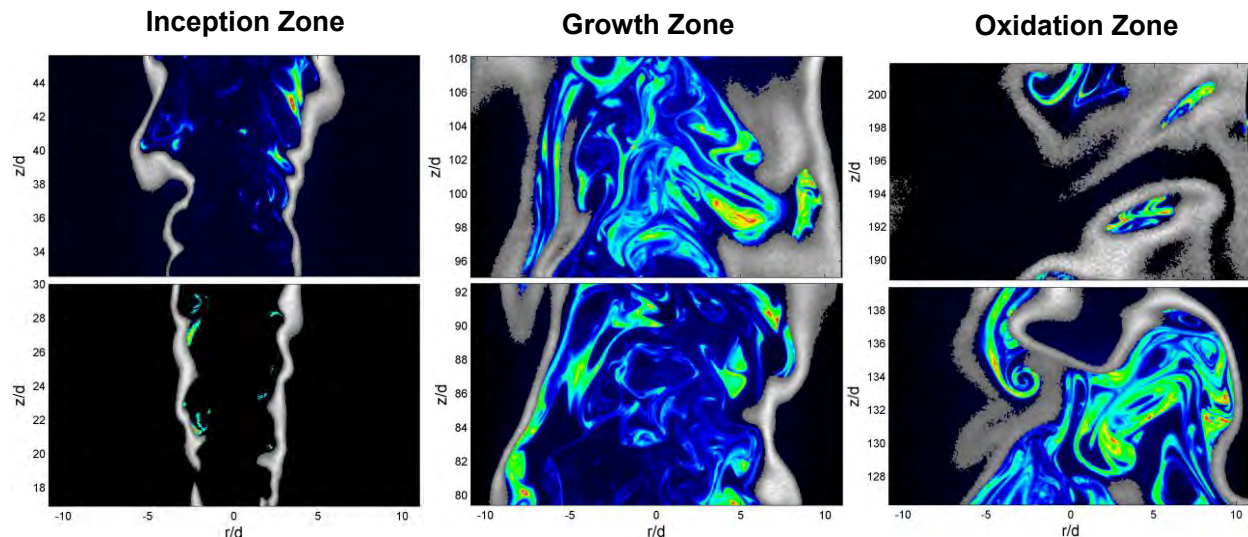
Figure 26. Evolution of OH• and soot structures within a Re = 20,000 turbulent non-premixed ethylene jet flame, as revealed by simultaneous LII and OH PLIF imaging.

OH• imaging in the JP-8 surrogate flame showed three differentiating effects from the imaging in the ethylene flame: (1) excitation of fluorescence from the m-xylene component of the fuel vapor and/or from closely related aromatic species produced from fuel pyrolysis (low in the flame, along the fuel jet axis), (2) significant degradation of the OH• signal on the far side of the flame relative to laser beam propagation (due to laser light extinction in the flame), and (3) the appearance of soot structures at the top of the flame that are not surrounded by OH• (suggesting quenching of the local flame sheet surrounding the soot). The simultaneous OH•-soot images from the JP-8 flame clearly show both of these effects, as seen in Fig. 27.

5.4.4 Simultaneous PAH PLIF and Planar LII

By tuning the dye laser wavelength off of the OH• excitation lines near 283.6 nm and adjusting the UV camera detection bandpass to include wavelengths from 330–480 nm, broadband, red-shifted fluorescence from aromatic species can be detected [92]. Performing these measurements in concert with LII, in the same manner as was done with the OH• fluorescence measurements, allows detection of the regions where pyrolytic chemistry is occurring together with detection of the soot field. Detailed studies in laminar flames have linked soot formation and mass growth to these regions of pyrolytic chemistry, so the simultaneous detection of these signals provides at least qualitative information on the extent of this linkage between PAH formation and soot formation in turbulent flames. Figure 28 shows a series of time-resolved "snapshots" of the PAH LIF overlayed with soot LII. The PAH structures tend to be relatively diffuse, so, for the purposes of the overlay they are indicated by their boundaries, as projected on the LII images. From Fig. 28, it is clear that PAH forms before any measurable soot is formed in the flame (as expected), and the PAH are generally constrained to the inner core of the jet, where the most fuel-rich regions are generally present. Also, the stronger soot LII signals occur in regions on the hot, outside edge of the PAH layers, suggesting an evolution of PAH into soot as the PAH undergo pyrolysis at high temperatures. Near the top of the flame, where soot formation has ceased, the soot PAH signals are very weak.
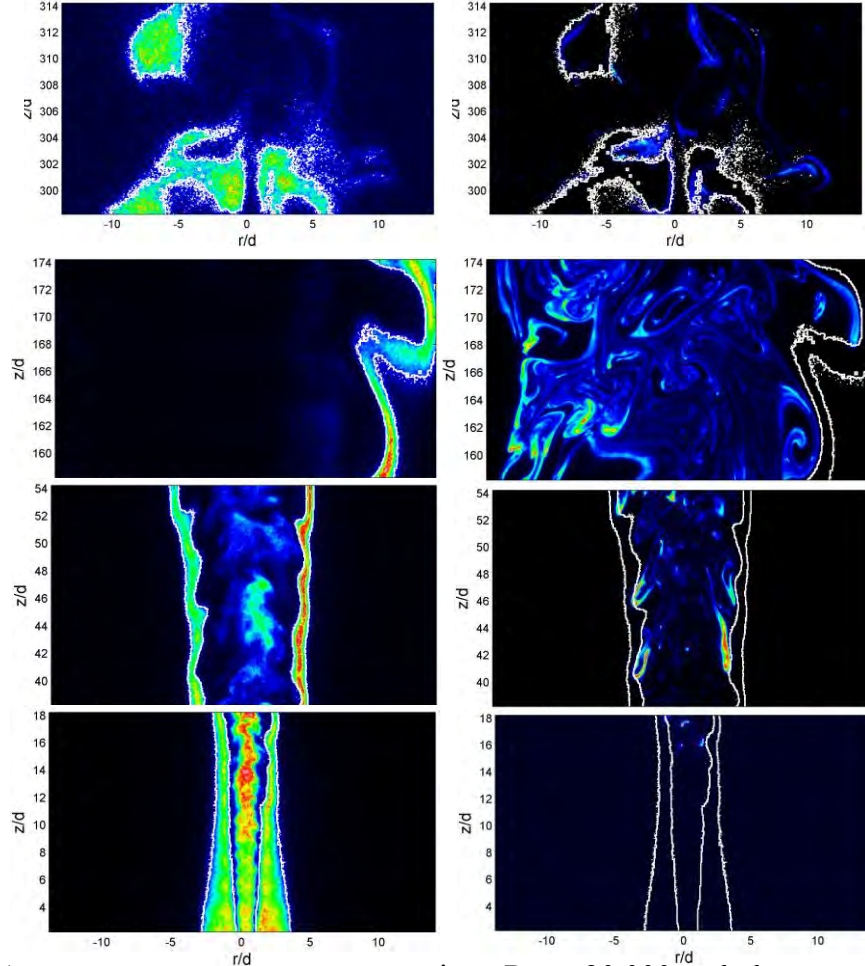
Figure 27. Evolution of OH• and soot within a Re = 20,000 turbulent non-premixed JP-8 surrogate jet flame, as revealed by simultaneous LII and OH• PLIF. Images on the left show LIF from OH• and PAH (in interior regions, particularly low in flame), whereas images on the right show soot LII, with boundaries of OH• in white.
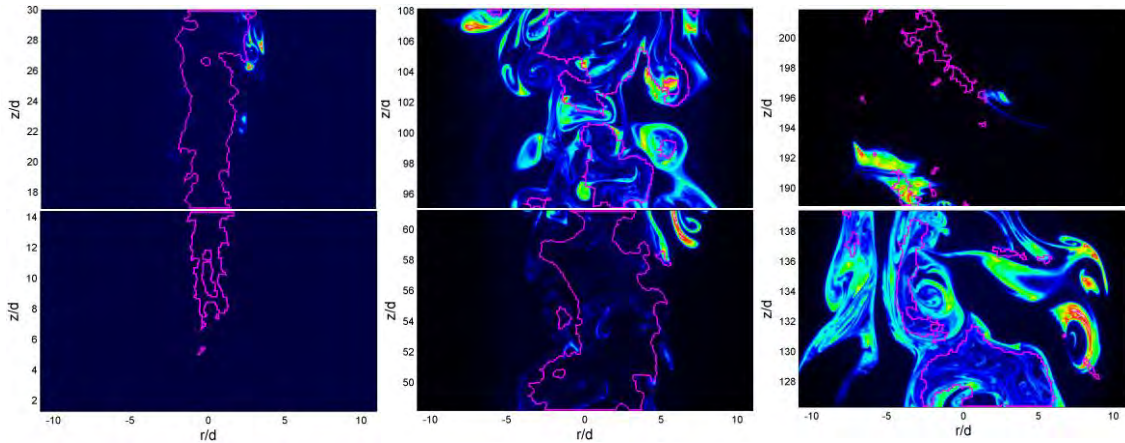
Figure 28. Evolution of PAH and soot structures within a Re = 20,000 turbulent non-premixed ethylene jet flame, as revealed by simultaneous LII and PAH PLIF imaging. The images show soot LII, with boundaries of PAH denoted in magenta.

33

5.4.5 Soot Volume Fraction

The planar LII measurements have been quantified in terms of soot volume fraction by calibrating against a laminar ethylene flame, anchored on the same jet burner. The calibration constant was determined by comparing the LII signal and the measured soot volume fraction derived from the laser extinction method, when using a best-available value of 9.3 for the dimensionless extinction coefficient of soot at 632.8 nm [93]. Note that this value for the dimensionless extinction coefficient (K_e) is approximately a factor of two higher than the values assumed by many combustion researchers, despite a wide array of data supporting such high values of K_e. Figure 29 compares the radial distribution of soot volume fraction measured by LII with that by extinction. As the laser extinction measurement is path-integrated, it needs to be de-convoluted (i.e. one needs to apply tomographic inversion) to give the spatial profile of soot volume fraction. We have used three inversion methods, including the Abel three-point and two-point methods and the onion peeling method [94]. All three methods give approximately the same results, with the Abel three-point method being smoothest. In general, the spatial profile from LII agrees quite well with those from laser extinction, giving good confidence in the determined calibration constant. Figure 30 compares the soot volume fraction integrated across the flame at different heights, $\int_{-\infty}^{\infty} f_V \, r \, dr$, as determined by these two methods. Good consistency is obtained, with deviations likely due to non-uniform flat-field response of the LII camera [95].
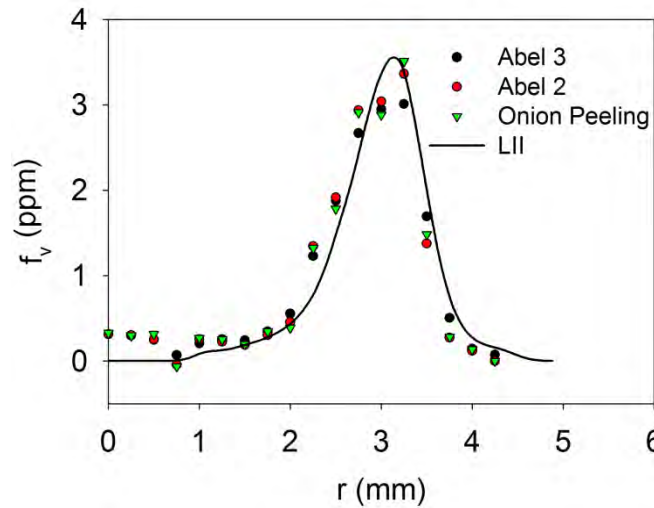
Figure 29.   Radial distribution of soot volume fraction at a height of 41.5 mm in a laminar ethylene jet flame as measured by laser extinction and LII. Measurements from extinction are de-convoluted with three algorithms: Abel three-point inversion (Abel 3), Abel two-point inversion (Abel 2), and onion peeling.

Instantaneous, mean, and rms soot volume fractions are presented in Fig. 31 for the turbulent ethylene jet flame. Each distribution is composed of stacked slices at different heights, with statistics at each height collected from 500 instantaneous images. Discontinuities between adjacent slices are evident and result from the non-uniform flat-field response of the camera system, which is exacerbated by the vignetting effect from a small lens aperture that was used to

correct for spherical aberrations in the lens. We are currently quantifying this flat field so we can correct these images for this effect.
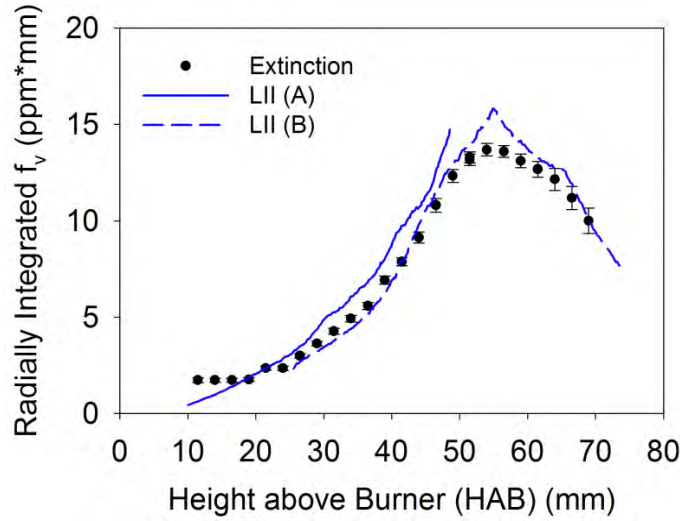
Figure 30. Axial profile of soot volume fraction integrated across the canonical ethylene jet flame measured by laser extinction and LII. A and B indicate results from LII images obtained at two different heights.

Probability density functions (PDFs) of soot volume fraction are shown in Figs. 32 and 33. In general, PDFs of soot volume fraction at all locations behave as clipped-Gaussian distributions, with significant zero-clipping. As zero-clipping is an indication of intermittency, this finding suggests that soot volume fraction is a highly intermittent scalar, which is consistent with the localized features of soot observed from instantaneous LII images and is also consistent with recent results reported for a turbulent jet flame fueled with natural gas [96]. Figure 32 shows the PDFs at various axial locations. The zero-clipping is initially dominant at upstream locations where soot appears as localized streaks and mostly stays away from the jet axis (Fig. 26), and then becomes less dominant when moving downstream, reaching a minimum at the height of 375 mm, where soot becomes connected and more evenly distributed. Near the flame tip, where soot only exists in distinct islands and is subject to strong oxidation, the PDF again shows prominent zero-clipping.

Figure 33 shows the evolution of the PDFs along the radial direction, where the height of 475 mm approximately corresponds to the peak mean soot volume fraction. It can be seen that at this height, although soot volume fraction has about the same range of variation at all radial locations (varying from 0 to 2.5 ppm), the degree of zero-clipping becomes greater when moving away from the jet centerline, where soot oxidation is expected to be more active and where eventually one moves outside the main flame brush. In fact, as shown in Fig. 34, the soot intermittency can be expressly evaluated from the series of LII images by defining a lower threshold for signal-noise that cleanly rejects all spurious signals (the threshold was defined to be equivalent to 0.03 ppm of soot). The intermittency shows the expected trends with axial and radial position within the flame.
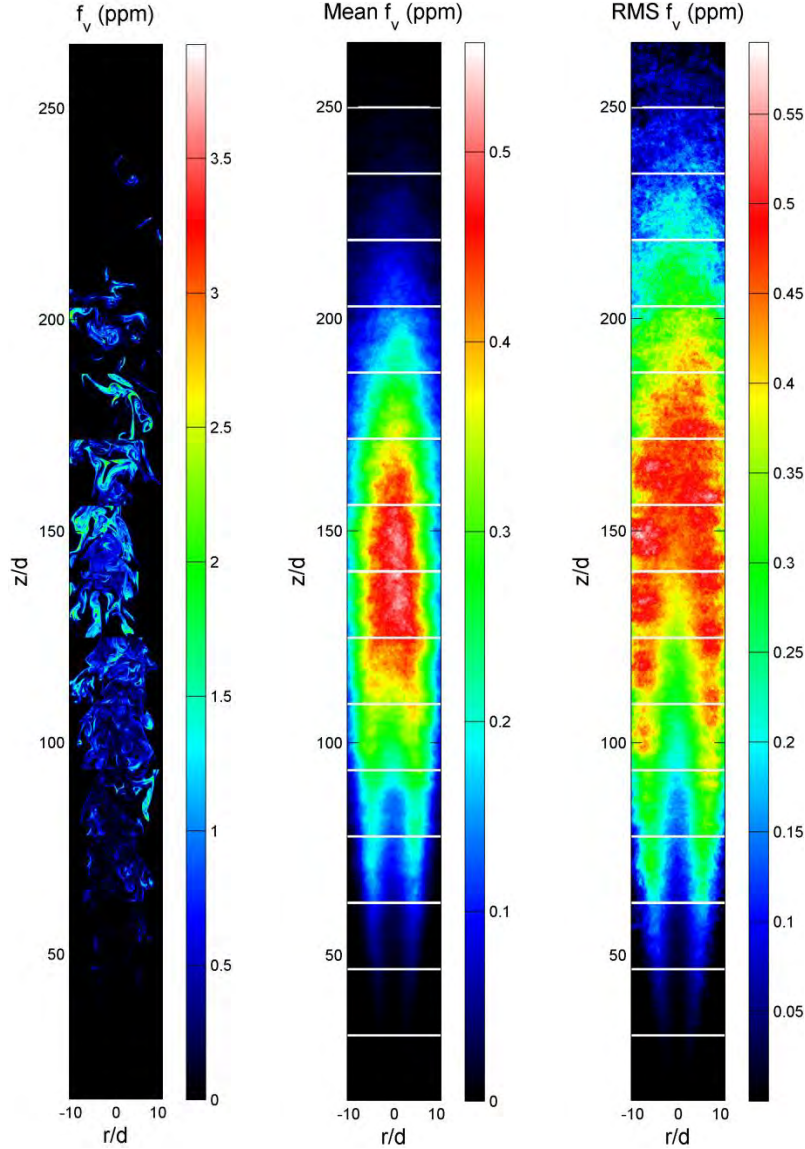
Figure 31.   Instantaneous, mean, and rms soot volume fractions measured by LII imaging in a Re = 20,000 turbulent non-premixed ethylene jet flame. The mean and rms statistics are computed from 500 instantaneous images taken at each height.

Instantaneous, mean, and rms soot volume fractions are presented in Fig. 35 for the turbulent JP-8 surrogate jet flame. As with the ethylene flame data, each distribution is composed of stacked slices at different heights, with mean values and statistics at each height derived, in this case, from 1000 instantaneous images. Discontinuities between adjacent image slices are even more strongly evident than was the case for the ethylene flame, for unknown reasons.

5.4.6 *Laser Extinction and Correction for Signal Trapping*

Optical and laser-based measurements in sooty flames are inherently complicated by the strongly absorbing nature of soot. As a consequence of this optical extinction, the local laser strength is typically reduced from that entering the flame, and the instantaneous laser strength depends on

z = 125 mm   z = 275 mm   z= 375 mm

z = 425 mm   z = 525 mm   z= 625 mm
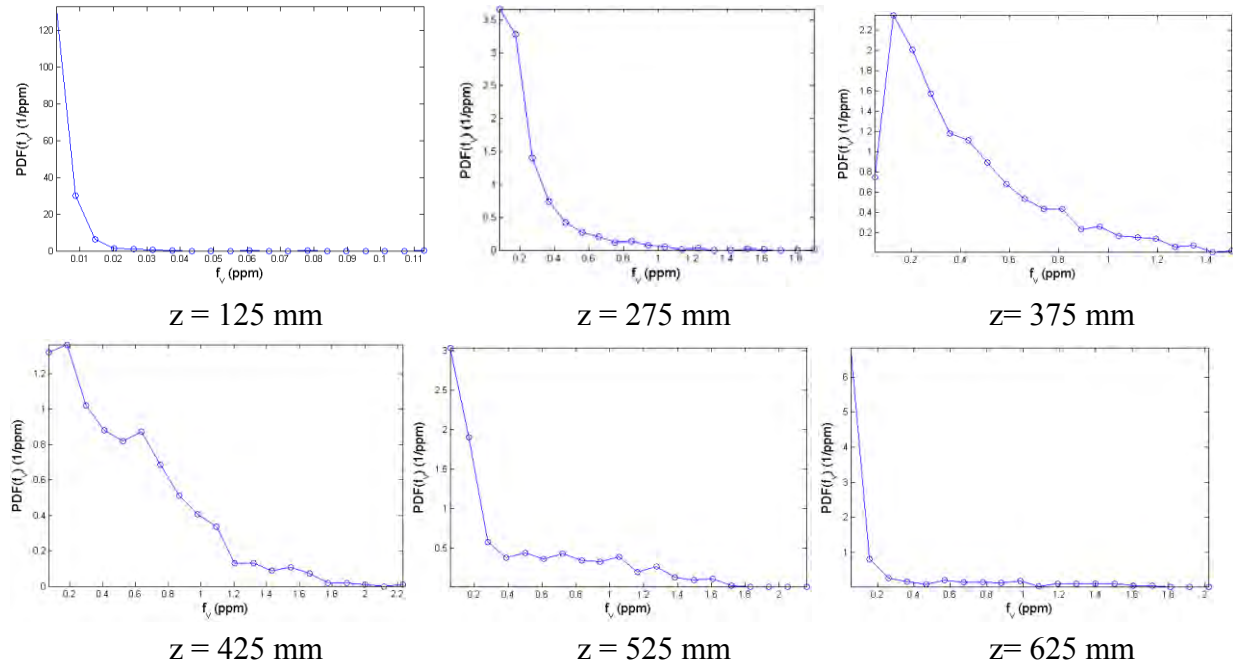
Figure 32.   PDFs of soot volume fraction at six axial locations along the jet centerline in a Re = 20,000 turbulent non-premixed ethylene jet flame. The statistics are computed from 1000 instantaneous images.
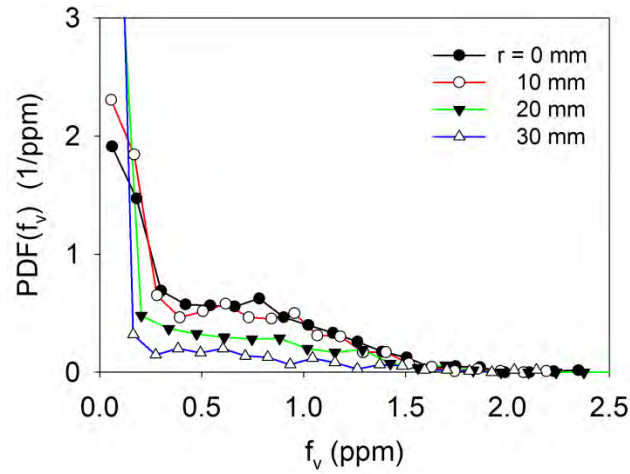
Figure 33.   PDFs of soot volume fractions at four radial locations of the same height of 475 mm in a Re = 20,000 turbulent non-premixed ethylene jet flame. These statistics are computed from 1000 instantaneous images.
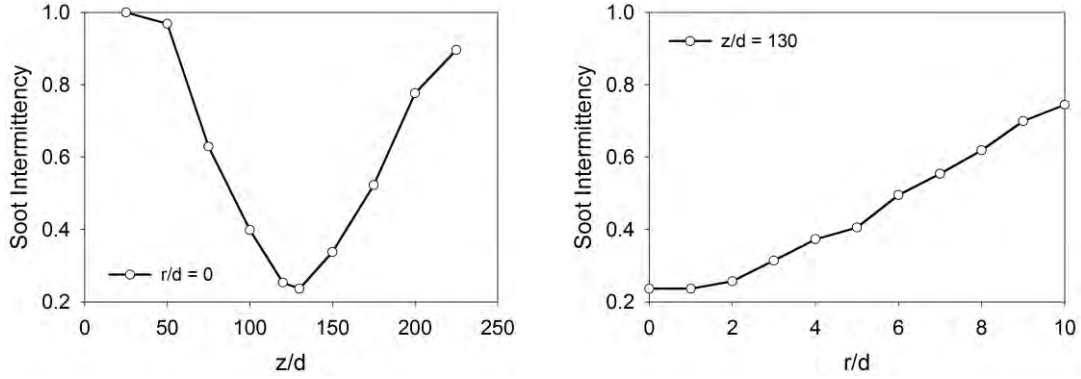
Figure 34.   Soot intermittency in the ethylene jet flame (a) as a function of axial position along the flame centerline (left) and (b) as a function of radial position at the height of minimum centerline intermittency.

the amount of soot that the laser beam has passed through in reaching the optical probe volume. Similarly, laser-generated signals in interior regions of the flame must pass through soot layers before they can exit the flame and be measured on photodetectors. Unlike the laser beam extinction, which depends only on the instantaneous soot concentrations along the laser line-of-sight, the signal extinction depends on the instantaneous soot concentrations within the optical acceptance angle cone of the camera imaging system (and thus is affected by soot within a broad region of the flame, particularly when using fast imaging optics). This attenuation of optical signals from interior regions of a flame is generally referred to as "signal trapping."

Optical extinction by soot nominally follows a λ^{-1} dependence at visible and near-infrared wavelengths [97]. To minimize the influence of optical extinction on the LII measurements of soot concentration, an excitation wavelength of 1064 nm (YAG fundamental) was used in this project, which limits the extinction of the laser beam itself and also allows detection of the LII signals at wavelengths through the visible region, limiting the extinction of the LII signal in comparison to typical LII signal detection around 400 nm. Use of a long-wavelength excitation wavelength for LII also has the distinct advantage of severely limiting the extent of C_2 and C_3 LIF produced from LII excitation [98].

To compensate for the decrease in the LII laser excitation strength as the beam propagated across sooty flames, the LII measurements were conducted in the fluence "plateau" region of the laser excitation power dependence curve, as indicated in Fig. 36. One of the unique and very useful aspects of LII measurements is that there typically exists a region of laser power (or, more properly, laser *fluence*, which is the amount of energy contained in a laser pulse) over which the resulting LII signal is approximately independent of the laser power. The precise shape of the laser power dependence curve and the size and "flatness" of this fluence plateau region strongly depend on the characteristics of both the laser pulse and the detection optics and filters [99,100].

For the laser and LII detection system that we have employed here, Fig. 36 shows that the signal response is approximately constant from laser fluences of $0.25 - 0.7$ J/cm^2. For this reason, we have employed a mean laser fluence of 0.6 J/cm^2, which allows for 60% extinction of the laser beam before significant influences on the generated LII signal would be expected. Indeed, as is evident in Fig. 27, the measured LII signal intensity does not show any significant side-to-side
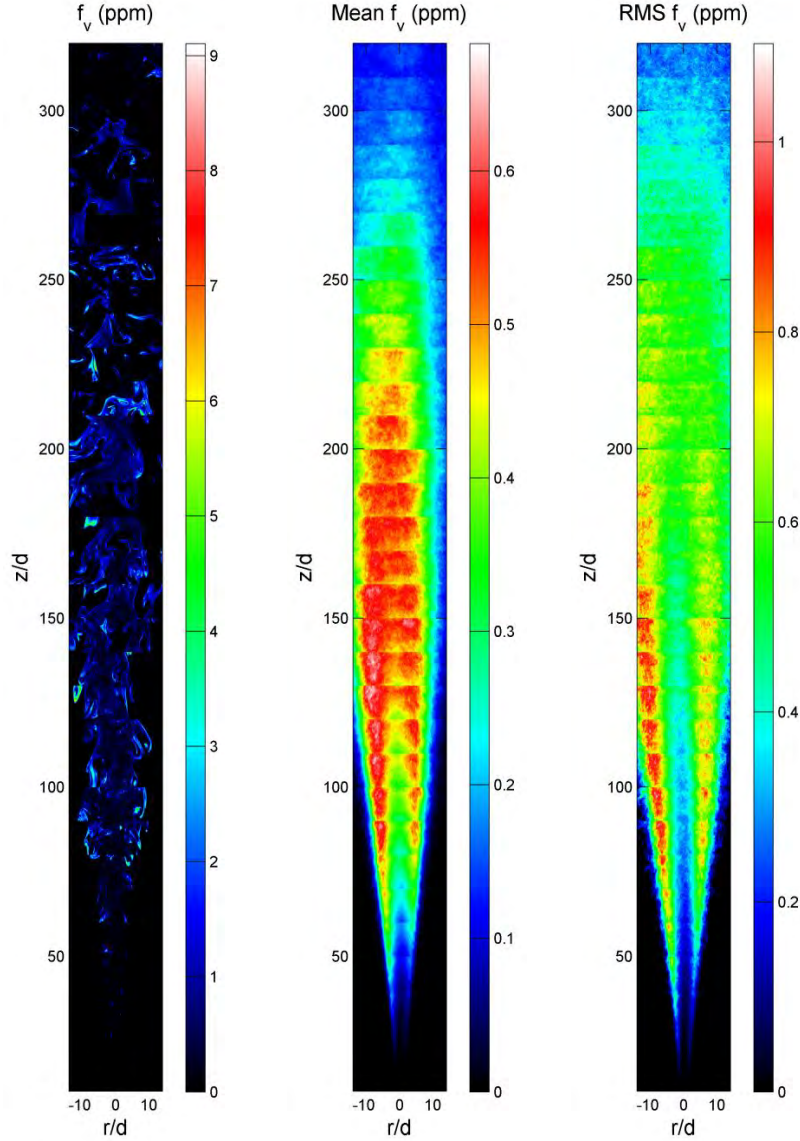
Figure 35. Instantaneous, mean, and rms soot volume fractions measured by LII imaging in a Re = 20,000 turbulent non-premixed JP-8 surrogate jet flame. The mean and rms statistics are computed from 1000 instantaneous images taken at each height.

variations, even at locations where strong attenuation of the OH PLIF laser sheet (at 283 nm) results in negligible OH LIF signal on the far side of the flame from where the laser beams enter.

To account for LII signal trapping in the sooty turbulent jet flames, extinction measurements were performed using a HeNe cw laser (632.8 nm) and an integrating sphere, to minimize beam-steering losses [101]. A schematic of the experimental configuration used is shown in Fig. 37. A polarizer was necessary to clean up the output of the HeNe laser such that a vertically polarized laser source was transmitted downstream of the polarizer, to polarization-sensitive optics such as the plate beamsplitter that directed a reference beam to a detector. With the use of an appropriate laser-line spectral filter in front of the transmitted beam detector, no measurable signal was
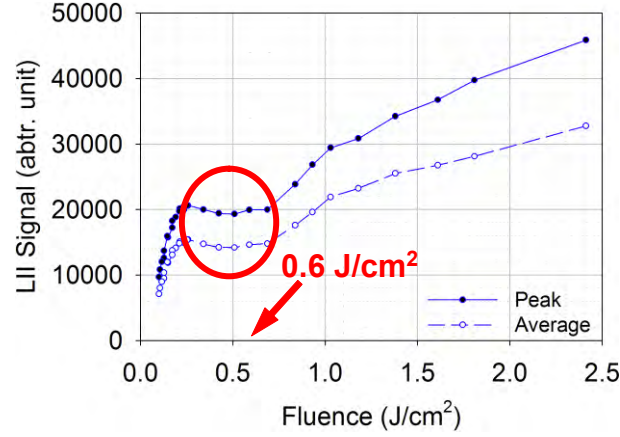
Figure 36.   Experimentally measured laser fluence dependence of LII signals measured on the laser-incident side of a laminar ethylene flame.
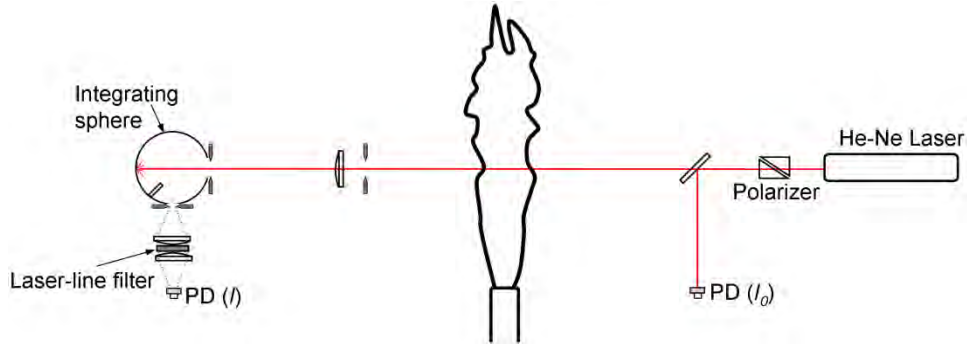
Figure 37.   Schematic of experimental setup for performing laser extinction measurements across a turbulent jet flame "PD" stands for silicon photodiode detector.

apparent from natural flame emission, so there was no need to employ laser beam modulation and lock-in detection. During experiments, the burner was traversed axially and radially to measure extinction along different chords through the flame, as shown in Fig. 38.

Extinction measurements were performed using a data acquisition rate of 40 kHz, allowing good resolution of turbulent fluctuations at fine spatial scales. A typical time series of soot optical thickness is shown in Fig. 39 in terms of the "KL factor," which is a measure of the product of soot concentration and soot layer thickness, as shown in Eq. 1.

$$KL = \ln\left(\frac{I_0}{I}\right) = \left(\frac{K_e}{\lambda}\right)\int_L f_V \; l \; dl \qquad (1)$$

where I_0 is the incident laser intensity, I is the transmitted laser intensity, K_e is the dimensionless extinction coefficient, λ is the laser wavelength, f_v is the soot volume fraction, and dl is the differential path of the laser light across the flame. If one defines a 'typical' value of the flame

thickness, then the KL factor is equivalent to a measure of the 'average' soot concentration across the flame.
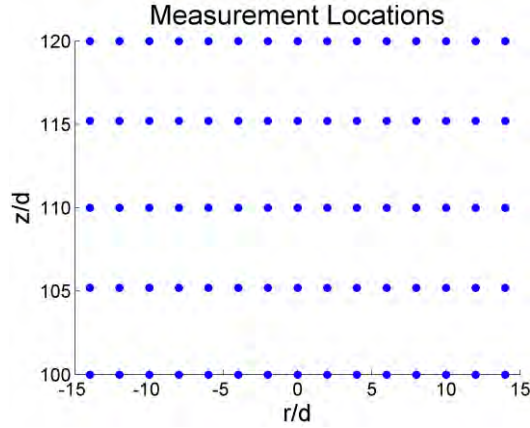
Figure 38.   Map of extinction measurement chord locations at a mid-height region of the turbulent jet flames.
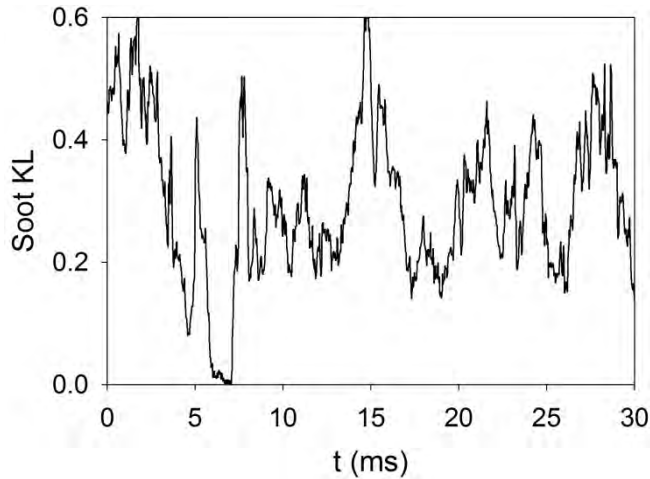
Figure 39.   A sample time record of measured soot optical thickness for the ethylene flame at z/d = 135, r/d = 0.

From Fig. 39, it is clear that the KL factor shows strong and rapid fluctuations, and occasionally gives a value of zero, implying very little soot along the beam path, which is consistent with the spatial intermittency of soot as observed by LII imaging. Fig. 40 shows the power spectral densities (PSDs) of the KL factor measured at five different heights of the ethylene jet flame. Except for z/d = 50, where the presence of soot along the centerline is highly intermittent, the PSDs largely collapse, implying similar frequency components. All the PSDs show constant-slope portions in the log-log plot, a feature characteristic to the turbulent inertial subrange.

By calculating the mean laser transmittance for each measurement chord and applying a two-dimensional interpolation algorithm that is included in the MATLAB software, the mean laser transmittance can be calculated throughout the PLII measurement domain within the turbulent jet flames. Dividing these values by a factor of two, to account for signal trapping across half the

projected flame width, the signal transmittance field can be calculated, as shown in Fig. 41. For the ethylene flame, this transmittance reaches a minimum of approximately 0.88, at mid-height, towards the center of the flame. From these calculated values of LII signal transmittance, the mean PLII measurements of soot volume fraction can be corrected for signal trapping, as shown in Fig. 42.
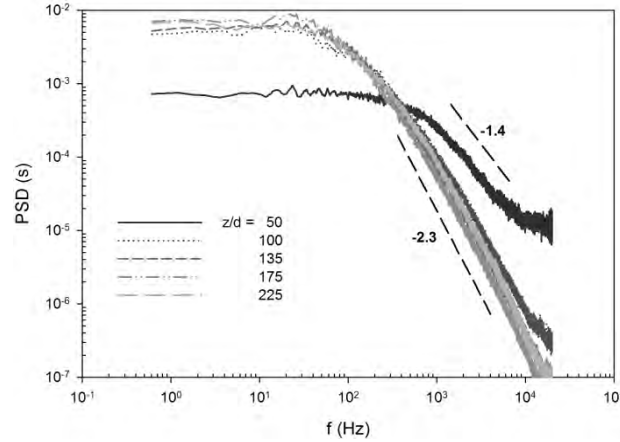
Figure 40.   Power spectral densities (PSDs) of soot optical thickness for the centerline of the ethylene flame at five different heights.
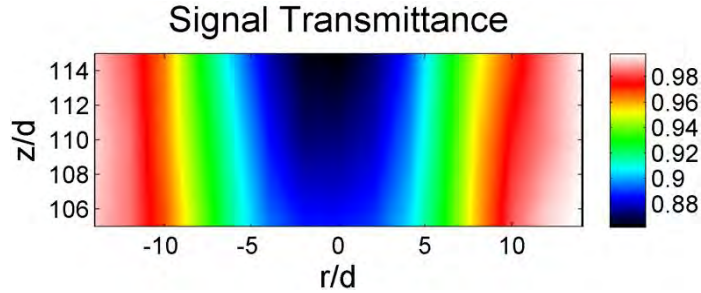
Figure 41.   Derived mean LII signal transmittance at mid-height of the ethylene jet flame.

5.4.7 *Joint Statistics of Soot Temperature and Volume Fraction*

Knowledge of the joint statistics of soot concentration and temperature in the canonical jet flames is important for accurate predictions of soot radiation intensity and also for validation of soot formation and oxidation rate expressions (because the relevant kinetic rates are strong functions of temperature). A measurement technique known as the "3-line" diagnostic, which combines a local laser extinction measurement of soot concentration and a two-color pyrometry measurement over the same probe volume, has been previously developed and applied in turbulent non-premixed flames to measure these joint statistics [102-105]. The diagnostic setup used in the current research is shown in Fig. 43.

A key aspect of this technique is the need to insert a two-ended probe into the flame to limit the length of the optical interrogation region. In previous studies, these probes have typically been

42
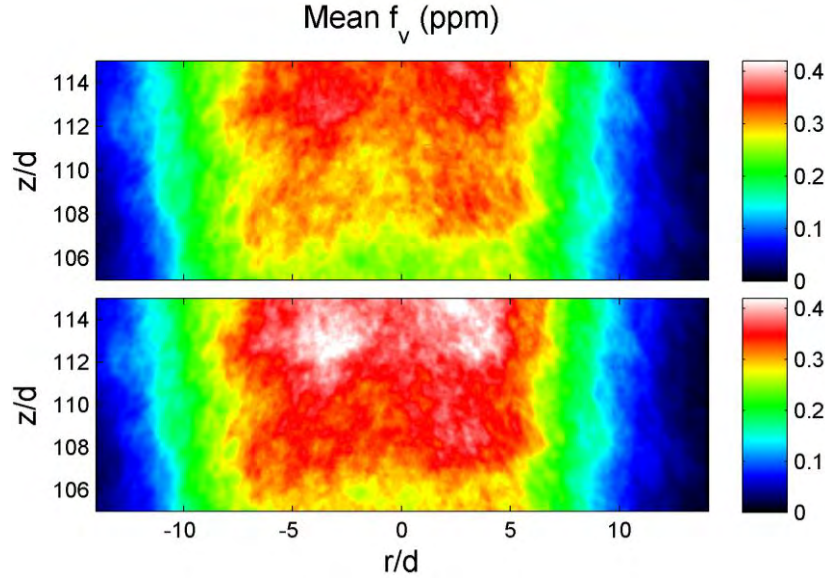
Figure 42. Original (top) and signal-trapping-corrected (bottom) LII data at mid-height of the ethylene jet flame.
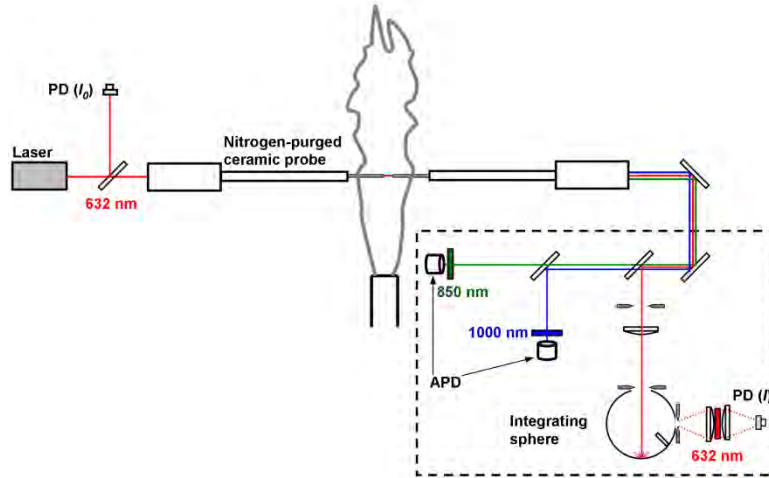
Figure 43. Schematic of diagnostic configuration used to perform 3-line measurements of soot temperature/concentration statistics in the turbulent jet flame.

constructed of water-cooled steel or aluminum tubing, in some cases with insulation wrapped around the outside of the probes. With this design approach, the probe tubes are necessarily quite large and also provide a thick thermal quench layer. To minimize probe perturbation of the flowfield and flamesheets, for this project we adopted the approach first used by Sivathanu and Faeth [102], with tapered refractory probe ends that are uncooled, as shown in Fig. 44.

A 10 mm probe end separation was used for most of the measurements, but some data were also collected for probe separations of 5 mm and 20 mm. Calibration of the two-color pyrometry diagnostic was performed using a high-temperature blackbody source and a mirror that redirected the blackbody light towards the avalanche photodiode detectors. Bandpass filters with center wavelengths of 850 nm and 1000 nm were used for the pyrometry measurement.
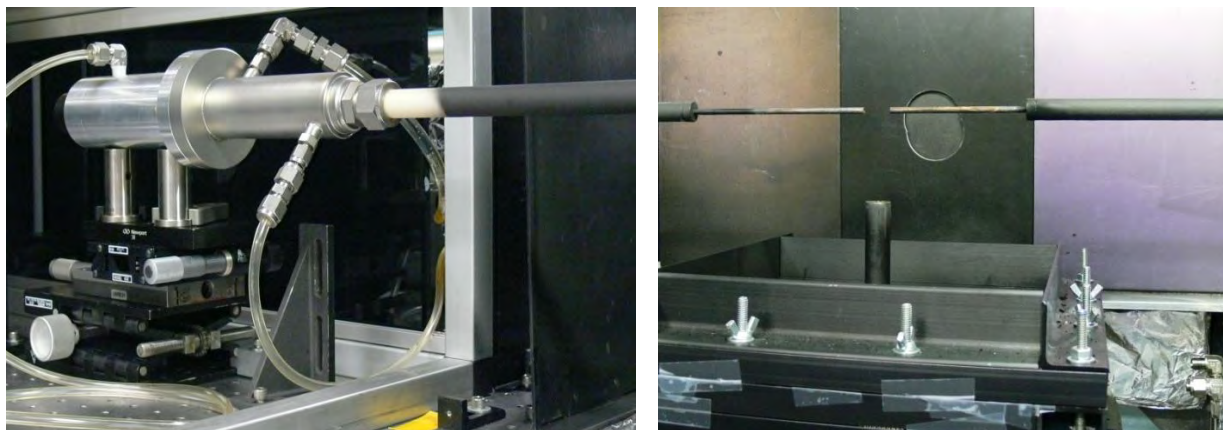
Figure 44.   Optical probe for performing 3-line measurements of soot temperature/ concentration statistics in the turbulent jet flame. Aluminum optical housing (left) is water-cooled and provides N_2 purge gas. Refractory probe ends (right) are uncooled.

Extinction of a 632.8 nm HeNe laser beam was used to determine soot volume fraction, by employing Eq. 1 with an assumed value for K_e of 9.3, based on the measurements of Williams et al. [93]. Fig. 45 shows a sample data record of transmission and emission signals from the ethylene flame at a mid-height position, along with the deduced soot volume fraction and temperature variation. Note that the apparent mean soot volume fraction of ~ 0.5 ppm compares favorably with the mean fv deduced from LII measurements in this region of this flame (Fig. 31). The pyrometry measurements show that the soot temperature is typically within the region of 1350 – 1650 K.

5.4.8 Thermal Radiation

Turbulent non-premixed flames using higher molecular weight fuels typically have substantial thermal radiation loss, on account of strong contributions from radiating soot. This radiant loss reduces the peak flame temperature and also acts to moderate both soot formation and oxidation, because of the high characteristic activation energies of these two processes. As will be demonstrated in a successive section on flame modeling, accurate modeling of soot formation and oxidation requires that soot radiation also be modeled accurately, because a model that predicts the correct soot concentrations within a flame or emitted from a flame but erroneously calculates the soot temperature will not be extendable to other flames. For this reason, measurements of thermal radiation from model flame systems are important components of model validation. As with other experimental measurements, the better the temporal and spatial resolution of the measurement, the more useful the data are for model validation. For this reason, a radiometer was constructed using a thin-film thermopile with a CaF_2 window. The use of the CaF_2 window material makes the radiometer equally sensitive to radiant emission from 0.13–11 μm, encompassing nearly all of the energy-containing radiation from the flame. The thermopile that was chosen for this measurement is 1 mm in diameter and has a characteristic response time of 12.8 ms (corresponding to a -3 dB cut-off frequency of 12.4 Hz). A black-anodized, 250 mm long water-cooled steel tube with an ID of 2 mm minimizes light reflections within the probe and restricts incident radiation to a small solid angle (Ω) of 1.065×10^{-4} sr. The detector sensor is
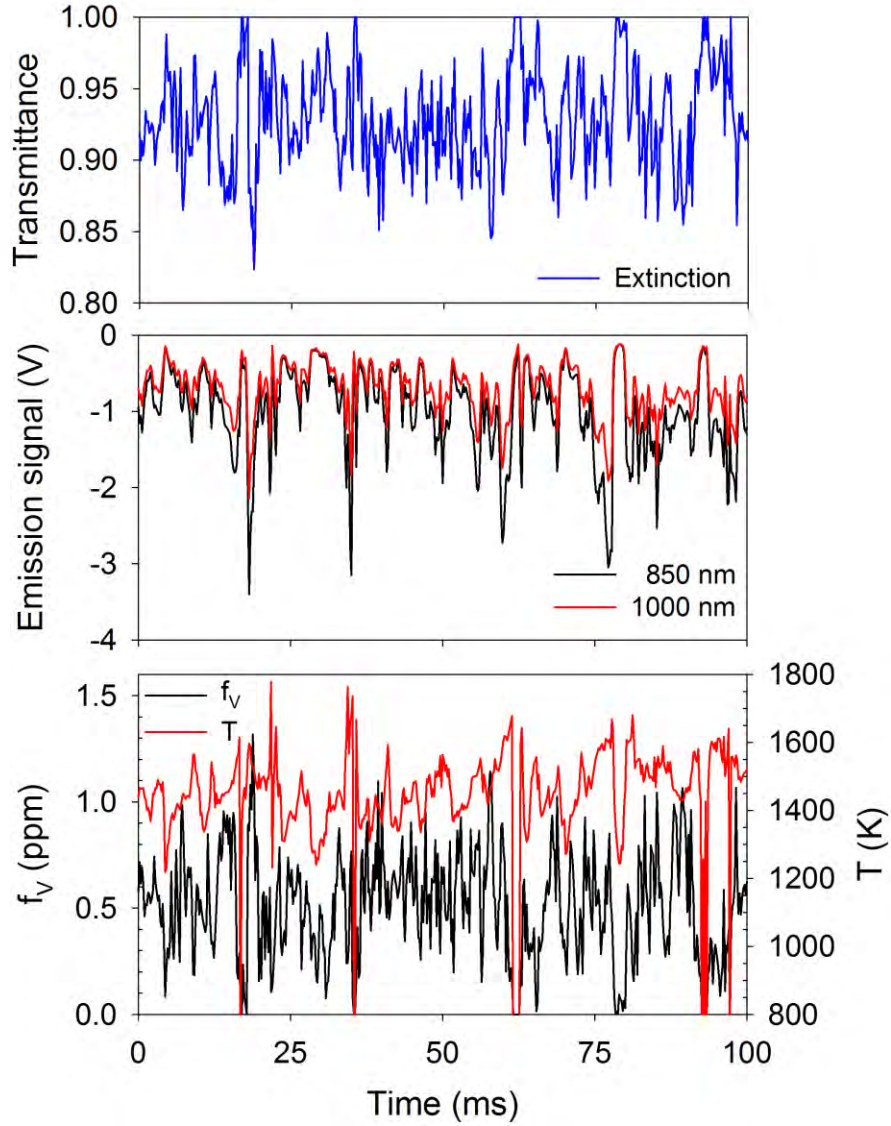
Figure 45.   Optical probe for performing 3-line measurements of soot temperature/ concentration statistics in the turbulent jet flame. Aluminum optical housing (left) is water-cooled and provides N_2 purge gas. Refractory probe ends (right) are uncooled.

located 500 mm away from the jet axis. During experiments, the burner is transversed axially or radially to measure radiation along different paths. As the radiative heat exchange and the electronic response of the thermopile detector are affected by its own temperature, great care has been taken to stabilize the thermal environment of the detector, such as covering the detector case with aluminum foil to shield flame radiative heating. In addition, three thermocouples are attached to the detector case to monitor its temperature, which is used to correct for the effects due to detector temperature rise as described below. The radiometer was calibrated by positioning the end of the light pipe at the exit of a high-temperature blackbody source, as shown in Fig. 46.
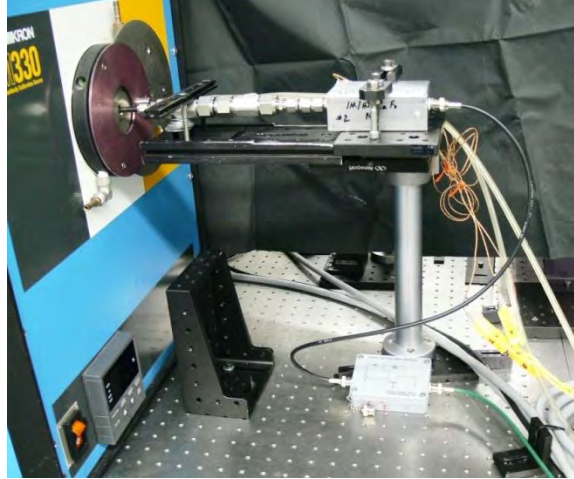
Figure 46. Photograph of radiometer, with water-cooled light pipe attached, positioned at exit of a blackbody source, to calibrate the radiometer output.

Figure 47 shows a sample time record of radiation measured at mid-height of the ethylene flame, along the flame axis. Figure 48 shows the time-averaged statistics of radiant intensity measured across the jet axis for both ethylene and JP-8 surrogate flames. It can be seen that these two flames have similar mean radiant intensity profiles as a function of flame height. The radiant intensity has near-zero values near the flame base, rapidly increases when moving downstream, and eventually peaks at mid-height. For the ethylene flame, the peak is at $z/d = 135$, and for the JP-8 surrogate flame, the peak is at $z/d = 175$. Above the radiant peak, the radiant intensity experiences a gradual decline, and again reaches a low value near the flame tip. The rms profiles show much broader peaks than the mean intensities and also peak at somewhat greater flame heights. It should be recalled that with the partial low-pass filtering provided by the detector response, the magnitude of the true rms intensities are underestimated. It is also interesting to note that, although these two flames have different flame heights and considerably different fuel composition, the mean radiant intensities within the two flames are almost the same for the first 135 jet diameters.
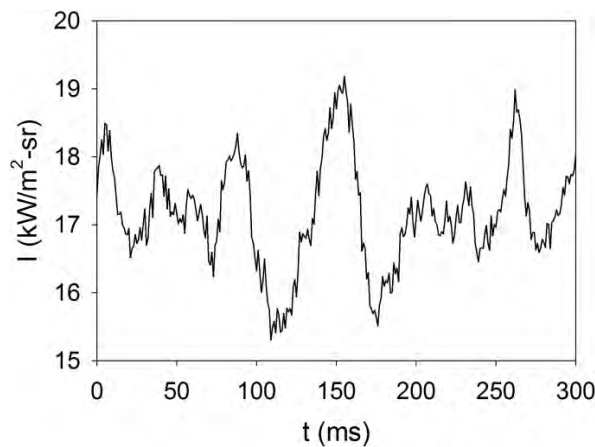
Figure 47. A sample time record of measured radiant intensity for the ethylene flame at $z/d = 135$, $r/d = 0$.
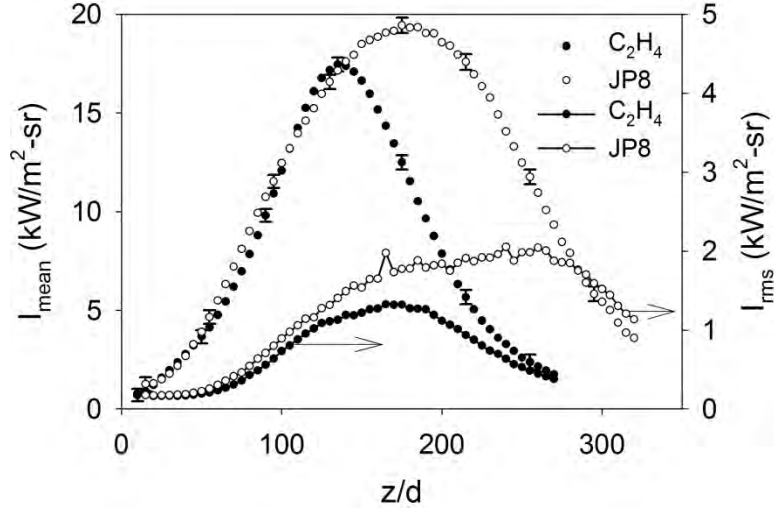
Figure 48.   Axial profiles of mean and rms radiant intensity measured
               within the ethylene and JP-8 surrogate flames. To avoid data
               cluttering, error bars are only drawn at selected positions.

Figure 49 plots radial profiles of time-averaged radiant intensity at different heights within the
ethylene and JP-8 surrogate flames. At all the heights, the radial profile peaks at $r/d = 0$, which
corresponds to the radiation path cross the jet axis. In general, the radial profile becomes broader
when moving downstream, suggesting a steady increase in mean flame width with z/d.
Comparison between the two sides of Fig. 49 reveals similar radial profiles for z/d up to 135,
implying similar spread of mean flame contour and similar radiative heat source in this near-
nozzle region. Integrating the radiant intensity profiles across the entire flame, the JP-8 surrogate
flame radiates much more than the ethylene flame and therefore possesses a greater radiant
fraction, since these two flames have approximately the same heat release rate of 16.5 kW.
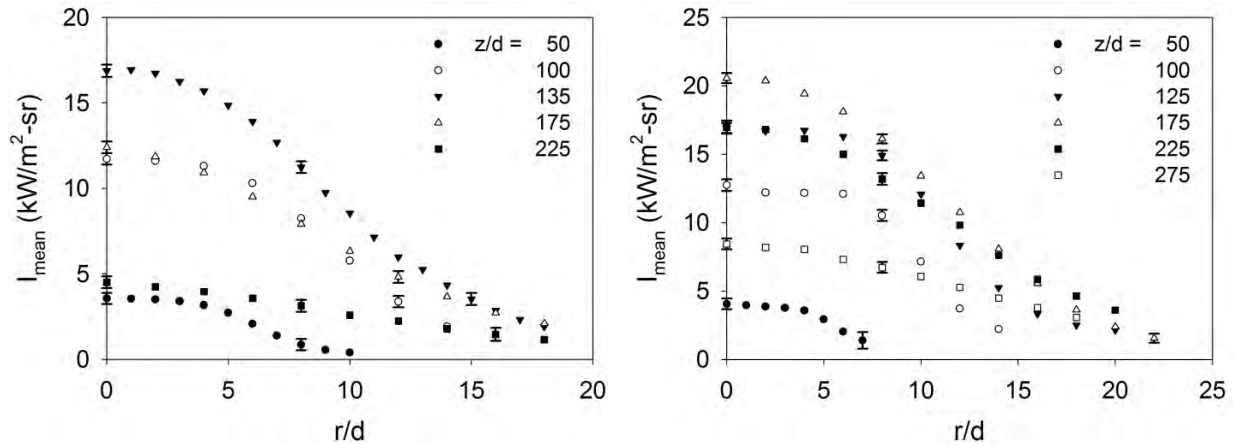
Figure 49.   Radial distributions of mean radiant intensity at several different heights within
               the ethylene (left) and JP-8 surrogate (right) jet flames. To avoid data cluttering,
               error bars are only drawn at selected positions.

47

5.4.9 Velocity Field

Velocity field measurements are desirable to verify that the overall mixing intensities predicted in flame simulations match well with the actual flames. For this purpose, particle image velocimetry (PIV) was employed in the turbulent ethylene jet flame. Performing such PIV measurements in relatively large, highly turbulent flames is quite difficult, on account of the need for high-density particle seeding, multi-frame data collection at each measurement position, and the limited spatial domain for each measurement. Furthermore, when performing PIV in strongly radiant flames, the long-duration camera gating that exists in certain PIV systems (such as the system owned by Sandia) can lead to obscuration of the particle scattering signals by the portion of the broadband luminosity that passes through the laser-line optical filter attached to the camera. During the course of this project, a specialized burner coflow system was designed and constructed which allowed for seeding of the flow immediately surrounding the burner, such that both the fuel jet and the surrounding coflow could be seeded. Fig. 50 shows a photograph of the PIV laser sheet passing just above the burner nozzle, when both the nozzle flow and the surrounding air coflow are seeded with particles. As is evident in this figure, the seeding in the coflow is quite uniform, and the seeding in the fuel jet illuminates the vortical mixing along the jet centerline. Unfortunately, as these measurements were the final ones performed during this project, insufficient time and funds were available to complete a definitive dataset of PIV data in this flame.

Figure 50.   Photograph of the base of the ethylene jet flame when applying PIV to the seeded flow within the fuel jet and in the surrounding coflow air.

5.5 Pressurized Spray Combustion of JP-8 and JP-8 Surrogate

We compared the lift-off lengths, ignition time, and soot volume fractions of the SERDP JP-8 surrogate and a conventional jet fuel to understand the overall performance of the surrogate. Experiments were initially performed at an operating condition, characteristic of modern diesel engine operation, where there was an extensive database of combustion and soot measurements

with a conventional jet fuel. This was followed by a more detailed study with the surrogate fuel for a wider range of ambient and injector conditions characteristic of gas turbine operation.

The conventional jet fuel that was used is an equal blend of five Jet-A fuel samples from different U.S. manufacturers and is called 'WA' in the following, standing for "World-Average" jet fuel. Holley and co-workers performed an ASTM D2425 standard analysis of this fuel and have provided detailed composition data: WA consists of 55.2% n- and i-paraffins, 17.2% cycloparaffins, 12.7% alkylbenzenes, 7.8% dicycloparaffins, 4.9% indans/tetralins, and 1.3% naphthalenes. Physical properties of the Jet-A blend and of the SERDP surrogate fuel are shown in Table 1. The surrogate ('SR') fuel has lower distillation temperature, density, and viscosity, but the lower heating values (based on mass) are quite similar.

Table 1. Fuel Properties

		"WA" World-Average Jet-A Blend	"SR" Surrogate Jet Fuel[1]
Distillation Temperature [$^{\circ}$C]	T_{10}	180	-
	T_{90}	251	-
	T_{100}	274	216
Cetane Number		46	70
Lower Heating Value [MJ/kg]		43.2	43.33
Aromatics [vol. %]		19	23
Density at 15 $^{\circ}$C [kg/m^3]		806	778.9
Kinematic Viscosity at -20 $^{\circ}$C [mm^2/s]		5.2	3.9

[1]23% m-xylene, 77% n-dodecane by volume; volume-weighted quantities

The injector hardware and operating conditions are summarized in Table 2. The injector is a standard common-rail diesel injector with a single 0.090 mm nozzle. The rail was sized to maintain pressure, producing a nearly constant rate of injection after nozzle opening. The injection duration, very long by diesel engine standards, produces ignition and penetration beyond the combustion chamber window during the first 3 ms. Data was acquired in the last 4 ms during a quasi-steady period of combustion – thereby neglecting this initial transient. Two different types of ambient gas conditions were selected. The first mimics operating conditions for the latest generation of low-emission diesel engines. These engines operate with significant exhaust gas recirculation (EGR) to lower NO_x emissions and allow operation in low-temperature combustion regimes. EGR dilution lowers the charge-gas oxygen concentration and this is simulated by using 15% ambient oxygen. While other conditions are fixed, 1000 K ambient temperature was also tested, considering that very low soot levels are often produced with a 900 K ambient. The SR and WA fuels were compared at these simulated engine conditions. For the SR fuel, additional conditions more applicable to gas turbine combustion were explored. Targeting 4.0 MPa as a typical takeoff gas turbine combustor pressure, we used elevated ambient gas temperature (1200 K) in combination with lower ambient oxygen (15%) to simulate the effect of spray mixing with recirculated hot combustion products as would happen in the central

recirculation zone of the combustor. The flame temperature at a soot formation threshold equivalence ratio ($\phi = 2$) is the same as that using air (21% O_2) initially at 810 K. To explore differences between combustion and soot formation processes using air or recirculated products, we varied the ambient temperature with both 21% and 15% ambient oxygen. The fuel injection pressure (or injection velocity) was also varied while other conditions were fixed.

Table 2. Experimental Operating Conditions

	Diesel Engine Conditions	Gas Turbine Conditions
Ambient Gas O_2	15%	15-21%
Ambient Gas Temperature	900 – 1000 K	800-1200 K
Ambient Gas Density	22.8 kg/m^3	11.8 kg/m^3
Ambient Gas Pressure	6.0-6.7 MPa	2.7-4.0 MPa
Injection Pressure	150 MPa	60-150 MPa
Injection Duration	7 ms	7 ms
Fuels tested	WA, SR	SR

5.5.1 Lift-off Length

The flame lift-off was measured by OH chemiluminescence imaging during the quasi-steady period of injection. In lifted sprays, it is well known that the mixture stoichiometry at the flame lift-off significantly affects the downstream soot formation. With increasing lift-off length, the soot formation decreases because the fuel jet entrains more ambient oxidants upstream of the lift-off and forms a leaner mixture. Liquid droplet vaporization may also be completed by mixing with hot ambient gases prior to the lift-off length. Therefore, knowledge of the lift-off length for fuels is needed along with the soot measurement. Images of flame lift-off length are shown in Fig. 51. These are ensemble averages of more than 40 OH chemiluminescence images taken during separate injections. The flame lift-off length, analyzed for each individual injection, is defined as the distance from the nozzle to the first axial location of the OH chemiluminescence and is overlaid as a red, dashed line on the image. Also shown are the jet cross-sectional average equivalence ratios at the lift-off, based on estimates for air entrainment into a 1-D model fuel jet. This estimated value is used for describing average trends in ambient entrainment and fuel-ambient pre-combustion mixing that occurred upstream of the lift-off length. Figure 51 shows that flame lift-off lengths range between 15 to 30 mm for the 900 K and 1000 K conditions shown. Separate spray visualization by Mie-scatter imaging shows that liquid droplets are completely vaporized well upstream of the lift-off length for these conditions. Therefore, combustion occurs without the presence of liquid droplets. Flame lift-off from the injector also coincides with jet velocities that decrease from that at the injector prior to combustion. For reference, the jet head penetration speed is approximately 50 m/s at the 20-mm axial position, which is substantially lower than the velocity at the injector exit. At fixed ambient temperature and density, the lift-off lengths of SR fuel are slightly shorter than that of WA fuel. As a result, the fuel-ambient mixture is slightly more fuel-rich when it burns at the flame lift-off. A shorter ignition delay and flame lift-off length is expected for SR fuel because past research has shown that fuels with a high cetane number tend to have a shorter lift-off length. SR contains 77% n-dodecane, which is quite reactive and has a cetane number of 87, compared to a cetane number of 46 for WA fuel (see Table 1). Although m-xylene (23%) suppresses ignition, a volume-

averaged estimate for cetane number for SR (Table 1) is still quite high (70), indicating that n-dodecane likely continues to dominate the ignition process of SR fuel. Despite the differences in lift-off length between fuels, estimates for ambient gas entrainment show that ambient temperature has a stronger impact on partial premixing than that of fuel type. For example, there is a difference of only 0.2 equivalence ratio units between fuels at 1000 K compared to a full
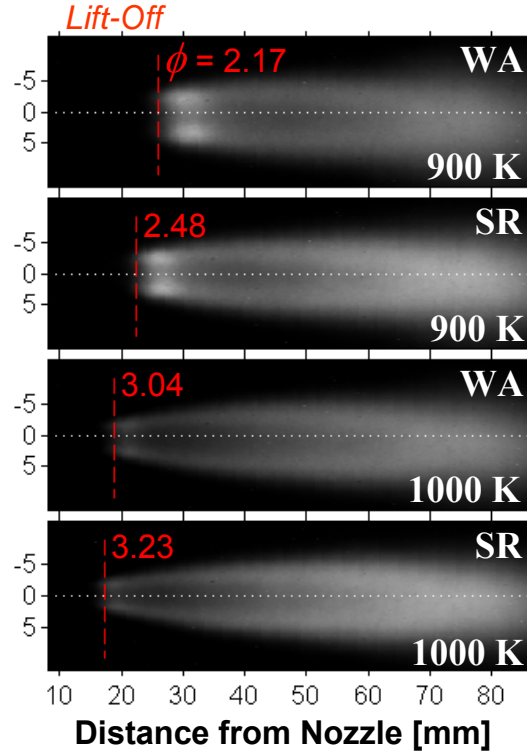
Figure 51.   OH chemiluminescence and lift-off lengths for a quasi-steady fuel jet. Operating conditions: 15% O_2, 22.8 kg/m^3 ambient density and 150 MPa injection pressure.

equivalence ratio unit change moving to 900 K. Consequently, one can compare soot formation and oxidation processes between fuels when there is reasonable similarity between partial-premixing, flame temperature, and residence time.

5.5.2 Soot Measurements

Simultaneous laser extinction and planar laser-induced incandescence (PLII) measurements were performed to acquire quantitative soot information. The laser extinction diagnostic provides the soot optical thickness KL, where the transmitted laser intensity, I, normalized by the baseline laser intensity, I_o, is related to the KL as

$$I / I_o = e^{-KL}$$

where K is the extinction coefficient and L is the path length through the soot. Time-averaged values of KL from multiple injections are shown in Fig. 52. Results are shown between 20 and 86 mm from the nozzle, which contains both soot formation and soot oxidation regions of the fuel jet. There is a general trend that the soot KL begins to increase by 20 to 30 mm, reaches a
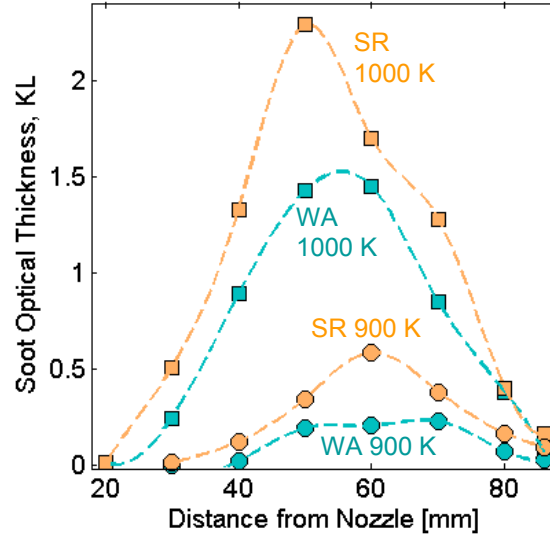
Figure 52.   Optical thickness (*KL*) data as a function of the axial
distance from the nozzle. Operating conditions as in
Fig. 51.

peak at around 50 to 60 mm, and then declines towards 86 mm (the measurement domain was limited by the optical access). At 900 K, however, the *KL* is much lower and reaches a peak further downstream compared to the 1000 K case. This result is consistent with the trend of lower soot formation at lower ambient temperatures. Also, the *KL* varies between the two fuels. At both 900 K and 1000 K, the peak *KL* is higher for SR fuel. The *KL* measurements reflect the trends shown by the PLII images given in Fig. 53. The PLII images are ensemble averages of more than 40 images each. The lift-off lengths are again indicated on the images by a vertical dashed line. The images provide only qualitative information of soot distribution in the fuel jet. Moreover, the camera gain was optimized for each fuel and ambient temperature; therefore, a fuel-to-fuel comparison is not possible from just the PLII. However, PLII images can be used in combination with the quantitative *KL* measurements at the jet centerline to obtain the time-averaged radial soot volume fraction (f_v) distribution. The PLII signal is proportional to the soot volume fraction. Also *KL* is quantitatively related to the soot volume fraction along the path of the extinction laser through

$$\int_{-Z_\infty}^{Z_\infty} f_v(z) \frac{6\pi}{\lambda} (1+\alpha_{sa}) E(m) dz = KL$$

where Z_∞ is the cross-stream position far outside of the jet, λ is the laser wavelength, α_{sa} is the scattering-to-absorption ratio, $E(m) = -\text{Im}[(m^2-1)/(m^2+2)]$, and *m* is the refractive index of soot. A value of $(1+\alpha_{sa})E(m) = 0.47$ (corresponding to a dimensionless extinction coefficient of 8.9) was used to relate *KL* to the soot volume fraction. From these equations, the calibration constant can be determined with the measured LII profile, measured *KL*, and known soot optical properties. This, in turn, enables the calculation of the radial soot volume fraction distribution. The computed soot volume fraction contours are shown in Fig. 54 for both fuels at 900 K and 1000 K. The lift-off lengths are also shown as a dashed vertical line along with the estimated cross-sectional-average equivalence ratio. The immediate conclusion is that SR jet fuel produces more
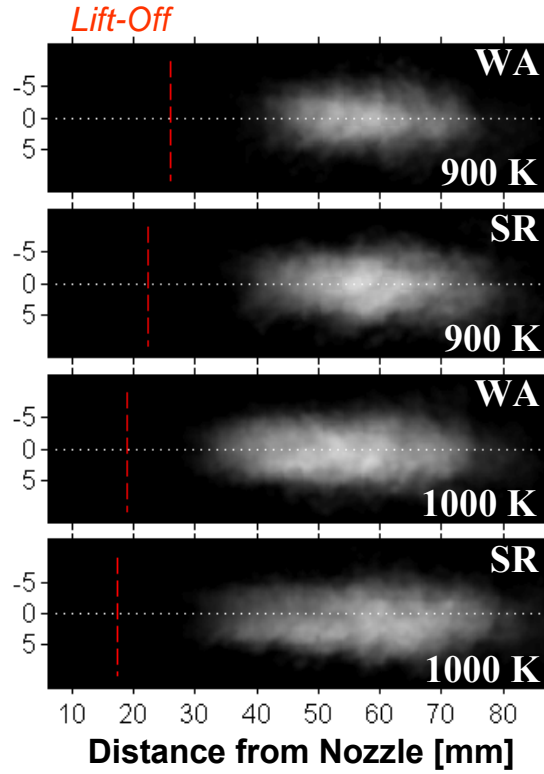
Figure 53. Planar laser-induced incandescence measurement. Operating conditions as in Fig. 51.
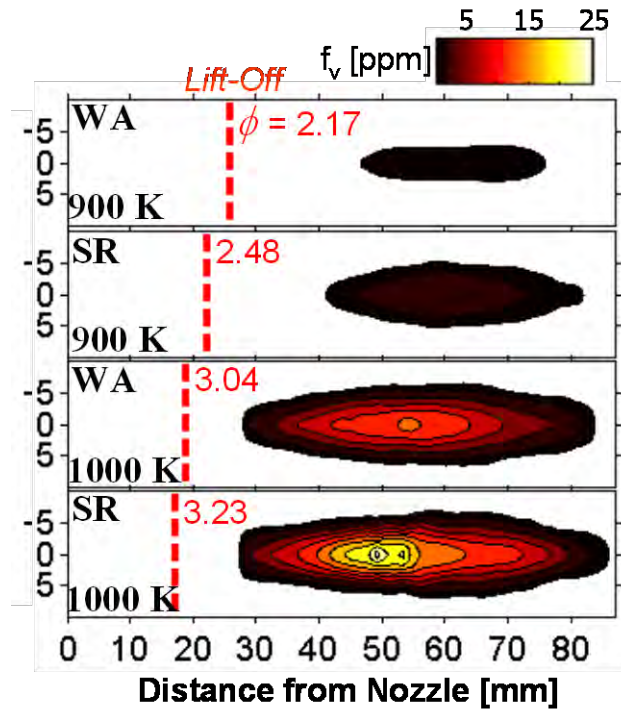
Figure 54. Soot volume fraction distribution. Operating conditions as in Fig. 51.

soot than WA jet fuel at fixed ambient temperature. For example, the peak soot volume fraction at 1000 K is 15 ppm for WA fuel but it increases to 25 ppm for SR fuel. In addition, in the soot formation region, a much steeper increase in soot volume fraction is observed for SR fuel.

5.5.3 *Influence of Ambient Conditions*

A strong influence of ambient temperature on soot formation is also seen in Fig 54. In contrast to the 1000 K condition, for a 900 K ambient temperature the soot volume fraction decreases by more than 3 times for both fuels. The flame lift-off and the soot region also move further downstream of the nozzle. Lower soot production is expected for WA fuel, because of the longer lift-off length and enhanced partial premixing. However, the differences in partial premixing are not enough to explain the large soot increase for SR. The most likely explanation for the high soot volume fraction for SR is fuel molecular structure effects on soot, owing to the higher aromatic content of SR compared to WA.

Figure 55 shows how the lift-off length and soot distribution change if operating at conditions more applicable for a gas turbine combustor with recirculation of hot combustion products. At 4.0 MPa pressure, the ambient gas density decreases from that shown previously, but the higher ambient gas temperature anchors the flame at approximately the same position, 20 mm from the injector. Because of the lower ambient gas density, there is less ambient gas oxygen entrained into the jet prior to the lift-off length, resulting in less partial premixing. A more fuel-rich combustion, combined with high ambient gas temperature that contribute to elevated temperatures in the soot forming region, causes significant soot formation downstream. Soot volume fraction levels reach about the same level as that at 1000 K and an ambient gas density of 22.8 kg/m^3. As the ambient density is much lower (11.8 kg/m^3), the similarity in soot volume fraction means that there is more soot formation at this condition per unit fuel mass (soot yield). Soot volume fraction would be expected to increase proportional to ambient density if the soot yield were the same. Therefore, these results show higher soot production than that at the previous high-density conditions. Another difference evident in Fig. 55 is that the soot oxidation region is elongated in the axial direction. The soot is no longer fully oxidized before reaching the limits of the measurement domain at 87 mm. This is the result of the reduced ambient pressure and density, as the lower oxygen concentration per unit volume causes less oxygen entrainment into the jet at a given axial position.
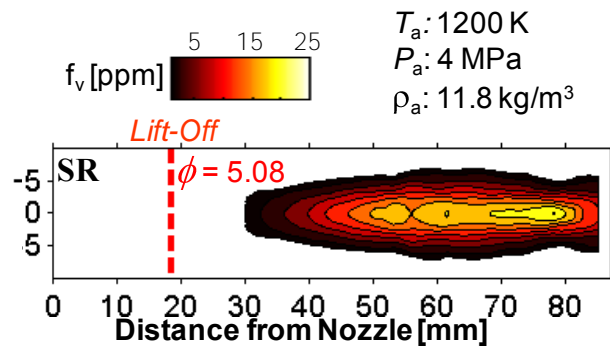
Figure 55.   Soot volume fractions distribution for a gas turbine combustor condition. Ambient conditions: 1200 K, 4.0 MPa, 11.8 kg/m^3, and 15% O_2. Injector conditions: SR fuel, 150 MPa injection pressure.

To obtain more details about ambient temperature effect on soot formation, OH chemiluminescence imaging was performed and *KL* was measured at an axial location of 60 mm from the injector, corresponding to the maximum *KL* for the gas turbine condition of Fig. 55. The results are given in Figs. 56 and 57. Injector conditions including the hardware and injection pressure were held constant. Figure 56 shows that the lift-off length decreases with increasing ambient temperature at fixed ambient O_2 concentration and ambient gas density. Due to the reduced oxidant concentration, the lift-off lengths at 15% O_2 are consistently longer than that at 21% O_2 at fixed temperature. However, the estimated equivalence ratios at the flame lift-off are about the same because the stoichiometric air-fuel ratio also increases with decreasing oxygen concentration. For the tested O_2 concentrations, the stoichiometric ambient-fuel ratio at 21% O_2 is 15.4, while it increases to 21.4 at 15% O_2. More ambient mass needs to be mixed into the jet to have the same equivalence ratio. The maximum soot optical thickness (*KL*) shows a close correlation with the estimated equivalence ratio.
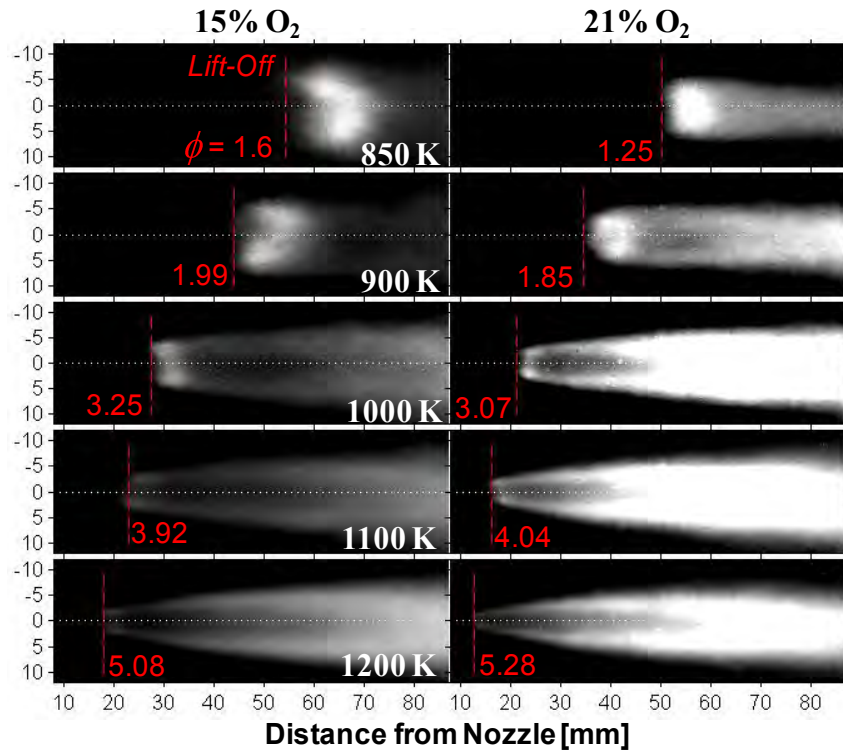
Figure 56.   OH chemiluminescence and lift-off lengths for a quasi-steady fuel jet. Operating conditions: 11.8 kg/m^3 ambient density, SR fuel, and 150 MPa injection pressure.

Figure 57 shows that soot increases with increasing temperature for each oxygen concentration; however, the increase is much more substantial at 15% O_2 compared to 21% O_2. Indeed, the trend of lower soot for 15% O_2 is reversed as the ambient temperature increases from 1000 K to 1200 K. A previous study in our facility showed the same trend when using n-heptane. These trends can be explained by a competition between residence time and soot formation rates. The residence time for soot formation increases and soot formation rates decrease when using reduced ambient oxygen concentration, but soot formation rates also increase with increasing ambient temperature. When there is low ambient oxygen, but high ambient temperature, high

55

soot levels are found because residence time and soot formation rates are both high. However, low-ambient-temperature, low-ambient-oxygen conditions have much less soot production because soot formation rates are low and dominate over the increased residence time. Accordingly, a reduction in soot production with decreasing oxygen concentration occurs only when temperatures are kept low.
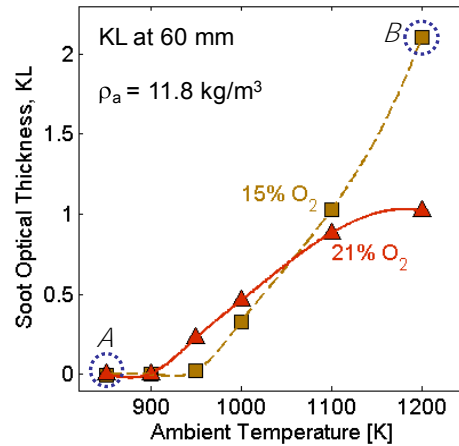
Figure 57.   Soot optical thickness (*KL*) versus ambient temperature for 15% O_2 and 21% O_2 gases. Operating conditions as in Fig. 56.

Two notable conditions are highlighted with labels *A* and *B* in Fig. 57 to illustrate the tradeoff between ambient temperature and oxygen concentration and its impact upon soot formation. Condition *A*, with 21% O_2, is more representative of pure air entering a gas turbine combustor. However, the low ambient temperature for condition *A* creates extensive partial premixing, such that the entire spray is non-sooting (*KL* = 0). This high level of premixing is highlighted in Fig. 56, where mixture equivalence ratios are shown to fall below soot-forming thresholds (ϕ = 2). In contrast, condition *B* has the same flame temperature as *A* at ϕ = 2, but the higher ambient temperature causes a shorter lift-off length, less partial premixing, and soot formation occurs downstream. We believe that condition *B* is more representative of combustion in a gas turbine combustor, where the fuel spray mixes with a mixture of air and hot recirculated combustion products. The impact of these two different pathways on mixing, combustion and soot production is stark, as one condition produces no soot and the other has maximum soot out of the conditions shown in Fig. 57.

5.5.4 Influence of Injection Pressure

The effect of injection pressure on soot level is presented in Fig. 58. Data are shown for four injection pressures at the same ambient conditions as the gas turbine condition shown in Fig. 56. The lowest injection pressure, 60 MPa, was the lower limit for fuel pressure control with the current injection system. The *KL* measurement location is fixed again at 60 mm from the nozzle. Figure 58 shows that the soot level decreases substantially with increasing injection pressure (or pressure drop across the nozzle). In fact, this peak optical thickness decreases linearly with increasing injection velocity.
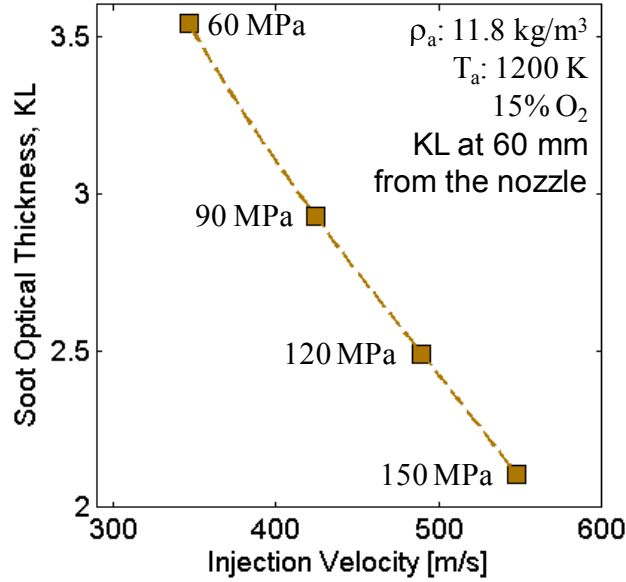
Figure 58. Soot optical thickness (*KL*) versus injection velocity (injection pressure). Ambient conditions: 15% O_2, 11.8 kg/m^3, 1200 K. SR fuel.

One cause for the observed trend is the lift-off length and corresponding equivalence ratio, as shown in Fig. 59. The linear increase in lift-off length results in an increase in upstream air entrainment relative to the amount of fuel injected. This increased premixing results in a

decrease in equivalence ratio at the flame lift-off. The effect of residence time of soot formation is another factor contributing to the decrease in soot level with increasing injection pressure. As the injection velocity increases there is less time for soot formation before the flame reaches the oxidation-dominated region. Again, the soot increase with decreasing injection pressure is well-documented at high-pressure, high-temperature conditions using diesel fuel and the same results are reproduced for a selected surrogate fuel and at selected ambient conditions. Further details about this work are presented in ref. 106.

5.6 Large Eddy Simulation

5.6.1 Coupled Treatment of Soot and Radiation Models in LES Simulations

Our model development approach was to first establish an understanding of the effects of thermal radiation on the predictions of soot, then to formulate a coupled soot and thermal radiation model to be used in both high-fidelity and engineering-based Large Eddy Simulations. The analysis was done using the reduced mechanism developed by H. Wang (22 species, 107 reactions) using the established soot model developed by Leung et al. [38] as a baseline. The Wang reduced ethylene model (whose development was previously described) consists of 22 species (H, O, OH, HO_2, H_2, H_2O, H_2O_2, O_2, CH_3, CH_4, HCO, CH_2O, CH_3O, CO, CO_2, C_2H_2, H_2CC, C_2H_3, C_2H_4, HCCO, CH_2CHO, and N_2) and 107 reactions. The Leung et al. soot model accounts for nucleation, growth, oxidation and coagulation and includes the first two moments to account for the soot number density and volume fraction. The strategy is to be complementary to
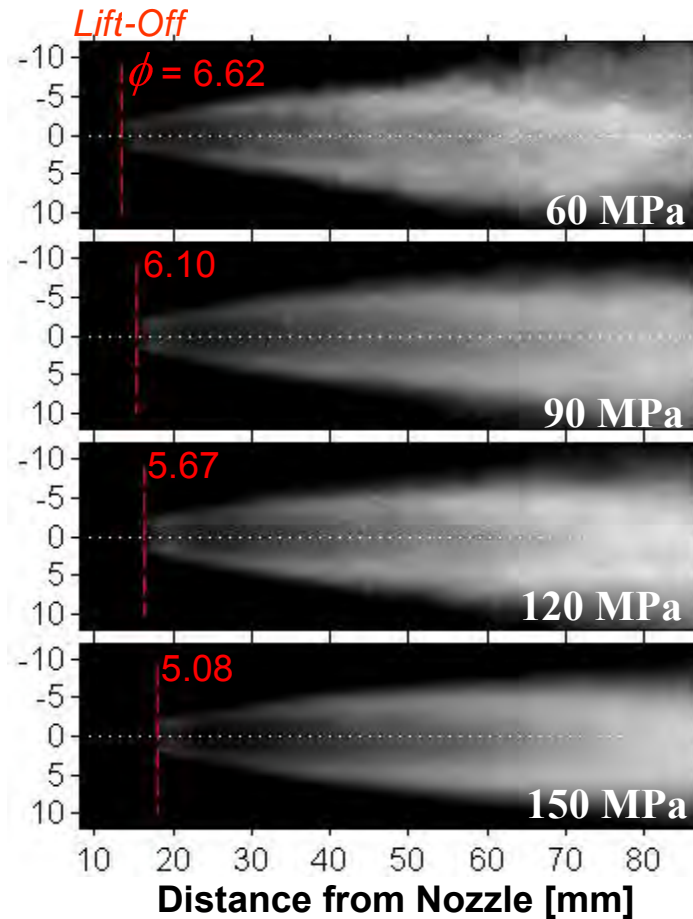
Figure 59.   OH Chemiluminescence and lift-off lengths for the conditions of Fig. 58.

other research efforts affiliated with this project, which focused on detailed aspects related to development of the soot model approach itself while assuming an optically thin medium. Here, we have developed a detailed understanding of the coupled effects of soot and thermal radiation and established a baseline engineering model for soot based on a systematic set of studies.

Modeling sooting flames and incorporating these models into a turbulence closure hinges on achieving simultaneous and balanced levels of accuracy with respect to a coupled set of submodels. The key models are the chemical kinetics mechanism, the soot model, including descriptions of soot inception, growth and oxidation, and a radiation model that is accurate for the medium of interest. All of this must of course be coupled with turbulence. Given the objectives outlined above, we systematically worked toward this goal as follows. First, a systematic study was performed that compared Wang's reduced mechanism to the original full mechanism (111 species, 784 reactions). Fig. 60 shows a comparison of CHEMKIN SENKIN results (calculating thermal runaway) for an ethylene/air mixure when using the full mechanism and the reduced mechanism. Comparisons of premixed flame calculations with the data of Bhargava & Westmoreland [107] also served to verify that the reduced mechanism performed well, as shown in Fig. 61.
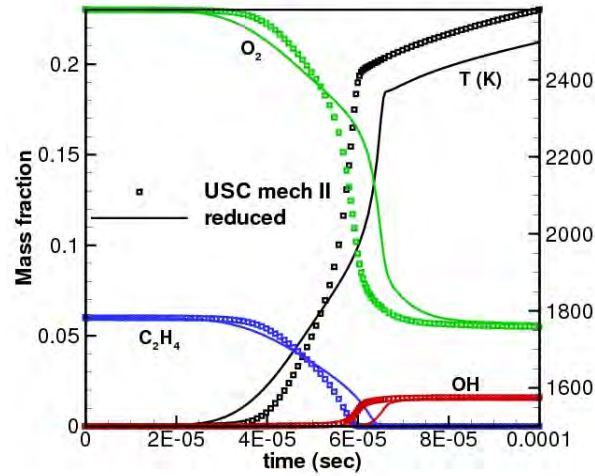
Figure 60.   Comparison of CHEMKIN SENKIN results for an ethylene/air mixture when using the full USC ethylene mechanism and the new reduced ethylene mechanism.
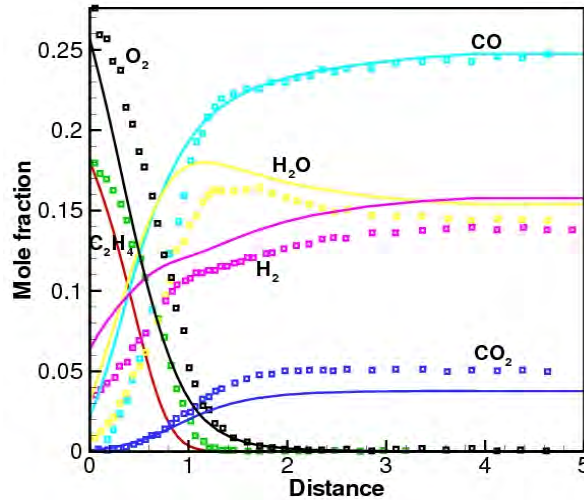
Figure 61.   Comparison between CHEMKIN PREMIX calculations using the reduced ethylene chemical kinetic mechanism and experimental measurements above a flat flame burner [107]: p = 2.7 kPa, $C_2H_4/O_2/50\%$ Ar, φ=1.9).

The soot model of Leung et al. [38] was then incorporated into the LES code and results were compared to premixed flame data provided by Appel et al. [108] and diffusion flame data from Wang et al. [109] (see Figs. 62 and 63). In both cases the temperature and soot volume fraction were shown to compare well with the data. Having established this agreement, we then focused on the sensitivity of the soot model to various radiation models. Here we used the optically thin approximation as a baseline, and incorporated a progressively more accurate (albeit more expensive) set of models to account for gray and non-gray mediums. The primary goal was to

59
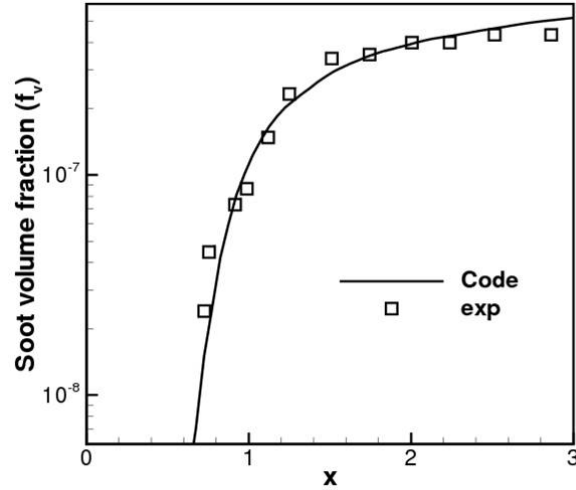
Figure 62.   Comparison of premixed experiment from Appel et al. [108].
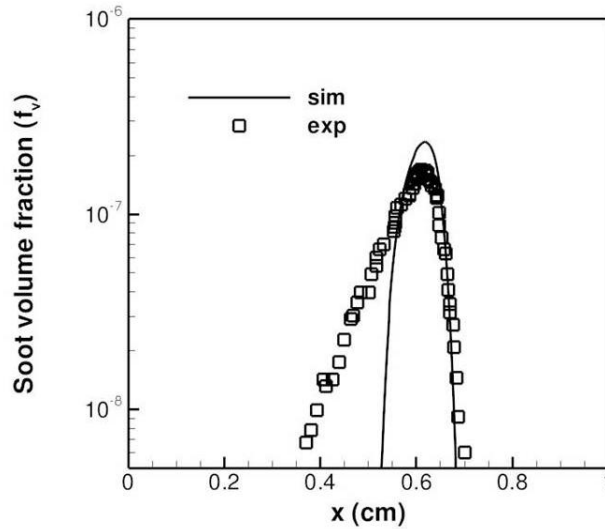
Figure 63.   Comparison of diffusion flame experiment from Wang et al. [109].

establish the limitations of the optically thin model in the context of soot model development. Results indicate that the radiation model itself has a more profound effect on soot predictions than isolated improvements on just the soot part itself indicating that the combined effects of soot and radiation must be considered for models developed for routine use in optically thick media.

The optically thin radiation model [110] was used to establish a bound in this commonly assumed limit. This model provides a simple algebraic equation for the radiative heat flux and is well known to underpredict temperature and therefore underpredict soot volume fraction. The primary reason for this is that the optical thin assumption only includes radiant emission and neglects radiant absorption. To account for optically thick mediums, we used the P_1 gray and P_1

FSK (non-gray) model from Wang et al. [111], which accounts for both emission and absorption with various levels of fidelity. The P_1 gray model is a Helmholtz equation with variable coefficients and a source term. The model also accounts for gas and soot radiation through the absorption coefficient and the evaluation of the Planck–mean absorption coefficients. The database for the gas phase is based on HITEMP from Modest [110]. The P_1 nongray model employs a Helmholtz equation and needs to be solved as a function of spectral location. We employ a Gaussian quadrature technique for its solution. Generally, around ten Helmholtz equations are required to solve the radiative heat flux. The absorption coefficient is a function of normalized spectral space. Each models described above provides a better prediction of temperature in optically thick mediums but includes additional complexity and cost. Thus, it is important to quantify the compounding effect of inaccurate temperature predictions on the soot model itself.

5.6.2 Soot model

The semi-empirical soot model from Leung et al. [38] uses the following soot chemistry mechanism

$$C_2H_2 \rightarrow 2C(S) + H_2,$$
$$nC(S) + C_2H_2 \rightarrow (S) + 2C(S) + H_2,$$
$$C(S) + \frac{1}{2}O_2 \rightarrow CO,$$
$$n \rightarrow (S-1)$$
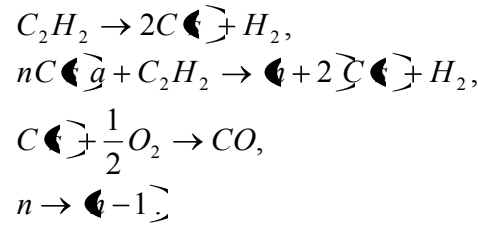
This mechanism includes nucleation, growth, oxidation, and coagulation and is coupled through source terms as a function of C_2H_2, CO, O_2 and H_2. The first two moments are considered to account for the number density and soot mass per volume. The soot mass fraction and particle number density are

$$\frac{\partial n}{\partial t} + \frac{\partial n u_j}{\partial x_j} = -\frac{\partial v_n}{\partial x_j} + \dot{\omega}_n,$$

$$\frac{\partial \rho Y_s}{\partial t} + \frac{\partial \rho Y_s u_j}{\partial x_j} = -\frac{\partial v_{Y_s}}{\partial x_j} + \dot{\omega}_{Y_s}$$

respectively. The soot diffusion term is

$$v_M = \underbrace{-\rho D_{p1} \frac{\partial}{\partial x_j}\left(\frac{1}{Le_M}\frac{M}{\rho}\right)}_{\text{Browniam Diffusion}} - \underbrace{0.556\frac{v}{T}\frac{\partial T}{\partial x_j}}_{\text{Thermophoresis}}$$

where M is either n or . The Lewis number for soot particles is in general large and the Brownian diffusion term is neglected. The source terms for the species, soot mass fraction and particle density are

61

$$S_n = \frac{2N_a}{C_{min}} - R_4,$$

$$S_{Y_s} = W_c \left(R_1 + 2R_2 - R_3 \right),$$

$$\dot{\omega}_{C_2H_2} = -W_{C_2H_2} \left(R_1 + R_2 \right),$$

$$\dot{\omega}_{O_2} = -W_{O_2} \frac{R_3}{2},$$

$$\dot{\omega}_{H_2} = -W_{H_2} \left(R_1 + R_2 \right),$$

$$\dot{\omega}_{CO} = W_{CO} R_3,$$

and the reaction rates are ($kmol/m^3/s$)

$$R_1 = 0.1E5 \exp\left(\frac{-21000}{T}\right) \left[C_2H_2 \right],$$

$$R_2 = 0.6E4 \exp\left(\frac{-12100}{T}\right) \left[C_2H_2 \right] \sqrt{A_s},$$

$$R_3 = 0.1E5 T^{1/2} \exp\left(\frac{-19680}{T}\right) \left[O_2 \right] A_s,$$

$$R_4 = 2C_a \left(\frac{6W_C}{\pi\rho_s}\right)^{1/6} \left(\frac{6\kappa T}{\rho_s}\right)^{1/2} \left(\frac{\rho Y_s}{W_C}\right)^{1/6} n^{11/6},$$

$$A_s = \pi \left(\frac{6\rho Y_s}{\pi\rho_s}\right)^{2/3} n^{1/3}.$$

Note that the total density including soot and the internal energy is $e = Y_g e_g + Y_s e_s$. The soot volume faction is $f_v = \frac{\rho Y\_s}{\rho_S}$ where $\rho_S = 1850\ kg/m^3$ which is defined as the soot density and $C_{min}=100$. The constants $C_a = 9.0$, $\kappa = 1.38E\text{-}23$ (J/K), and $N_a = 6.022E26$ (particles/kmol) are the agglomeration rate constant, incipient carbon particle Boltzmann constant, and Avogadro's number, respectively.

5.6.3 Radiation model

Thermal radiation is represented by Q_r and gives the rate of radiation heat loss per unit volume. This term enters into the energy equation as the divergence of the radiative heat flux and quantifies the loss or gain of thermal energy due to both emission and absorption as

$$Q_r = -\nabla \cdot q_r = \int_0^\infty \kappa_\eta \left(\int_{4\pi} I_\eta \Omega d - 4\pi I_b \right) d\eta$$

$$= \int_0^\infty \kappa_\eta \left(G_\eta - 4\pi I_b \right) d\eta$$

Here, η is the wave-number, Ω is the solid angle, κ_η is the spectral absorption coefficient and I_η is the spectral radiative intensity, G_η the spectral incident radiation and b denotes a black-body property.

From Wang and Modest [111,112], the P_1 non-gray radiation model is

$$Q_r = -\int_0^1 ku \left(\pi I_b - G_g \right) dg.$$

Where k is the reordered local mixture absorption coefficient and is a function of the spectral g variable weighted by the Planck function. The quantity u is a scaling function that incorporates the spatial variations of the absorption coefficient, and a is a nongray stretching factor accounting for varying local temperatures in the Planck function. Term G_g is the spectral incident radiation in g-space. The P_1 approximation is given by

$$\nabla \cdot \frac{1}{ku} \nabla G_g = 3ku\left(G_g - 4\pi a I_b \right) \qquad (1)$$

The boundary conditions for equation (1) are

$$-\frac{2(2-\varepsilon)}{3\varepsilon} \hat{n} \cdot \nabla G_g + ku G_g = 4\pi ku a I_b$$

where ε is the surface emittance. If the wall emittances is zero ($\varepsilon = 0$), then $\nabla G_g = 0$. The incident radiation G_g is calculated at spectral locations as a function of g. To compute Q_r for the non-gray radiation, the integration is performed by numerical quadrature. If Gaussian quadrature is used, then equation (1) is approximated by

$$Q_r \approx -\sum_{j=1}^M \omega_j k_j u_j \left(\pi a_j I_b - G_g \right)$$

A simpler method is to assume that medium is gray, which yields

$$Q_r = -\left(\pi \kappa_p I_b - \kappa_p G \right)$$

where $I_b = \sigma T^4$. Here, G is the spectral incident radiation and κ_p is the Planck mean absorption coefficient. The incident radiation G is solved by the spherical harmonic P_1 method with self-absorption term which is defined as

$$\nabla \cdot \frac{1}{\kappa_p} \nabla G = 3\kappa_p \left(G_g - 4\pi\kappa_p I_b \right) \qquad (2)$$

The boundary conditions for equation (2) are

$$-\frac{2(2-\varepsilon)}{3\varepsilon} \hat{n} \cdot \nabla G + \kappa_p G = 4\pi\kappa_p I_b.$$

The model accounts for gas and soot radiation through the absorption coefficient and the evaluation of the Planck--mean absorption coefficients are from Zhang and Modest [29]. The database is based on HITRAN96 and HITEMP using curve-fitting for CO_2, H_2O, CH_4, and CO. The absorption coefficient for soot is from Kent and Honnery [113] which is modeled as $a_{soot} = 18.62 f_v T$. Therefore, the absorption coefficient is $\kappa_p = p\sum_i \kappa_{p,i}(T) + a_{soot}$ [113-115]. For optically thin radiation, G is zero. Therefore, $Q_r = -4\pi\kappa_p \sigma T^4$.

5.6.4 Sensitivity Analysis

To understand the sensitivity of the coupled system of soot and radiation models, we compare results to the premixed flame from Appel et al. [108] and a diffusion flame from Wang et al. [109]. Figure 62 is a comparison of a premixed flame from Appel et al. and Figure 63 is a comparison of a diffusion flame from Wang et al. The symbols denote the experiment and the simulation is the solid line. Note that reasonable agreement is obtained for the premixed flame. As for the diffusion flame, Leung et al. soot model over-predicts the peak soot volume fraction and under-predicts the soot away from the peak value. The under-prediction is also observed from Wang et al. using a method of moments with interpolative closure.

Figures 64 illustrates the sensitivity of the soot predictions to minor changes in temperature from radiation effects, particularly the effect of including both absorption and emission. We applied the P_1 gray radiation model to an unsteady, unstrained diffusion flame that mimics the conditions of our piloted ethylene jet flame. This problem is a good canonical case to study the effects of radiation as a function of time at conditions analogous to those observed in the jet flame. Relatively small effects of radiation on temperature predictions have a significant effect on the soot volume fraction predictions. The maximum temperature with no radiation model, optically thin radiation, and P1 gray model are 2240 K, 2170 K and 2155 K, respectfully. The maximum soot volume fraction with no radiation, optically thin radiation, and P_1 gray model are 1.62 ppm, 0.75 ppm and 0.68 ppm, respectfully. This simulation illustrates that a small change in temperature (~85 K) can induce an order of magnitude change in soot production. Figure 65 shows the calculated soot volume fraction error between the optically thin radiation model and the P_1 gray model, where P_1 gray model is assumed to be the correct solution. Errors as great as
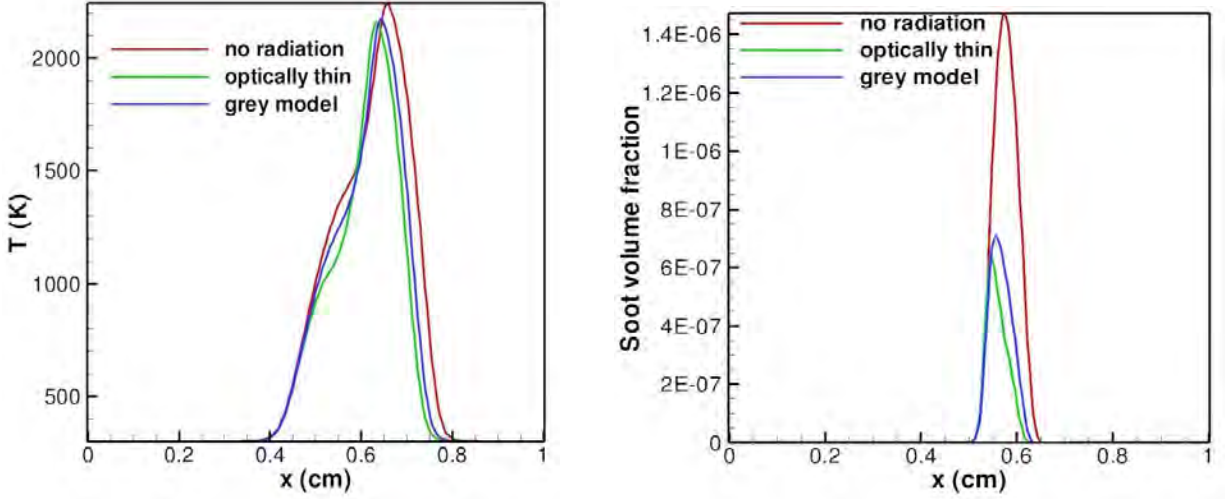
Figure 64.   Unsteady, unstrained ethylene-air diffusion flame showing soot volume fraction which compares the optically thin radiation model, P_1 gray radiation model and no radiation model.

100 percent are observed (albeit on the edge of the soot profile), which highlights the need to advance both the soot and radiation models concurrently.

5.6.5 LES of the ethylene-air diffusion flame

Using the models and insights above, we performed an LES of the piloted ethylene-air flame experiment described previously. The goal was to establish the baseline accuracy of a flamelet model designed for engineering that incorporates both soot and detailed treatment of radiation in a manner that complements Carbonell et al. [115], Watanabe et al. [116] and Chan et al. [117]. To account for the coupled effects of soot and optically thick radiation for flame structures that are consistent with the flamelet approximation, we have incorporated the soot and radiation "sub" models described above into the baseline flamelet equations. This provides both a base model for engineering LES and also a mechanism to incorporate and test more detailed
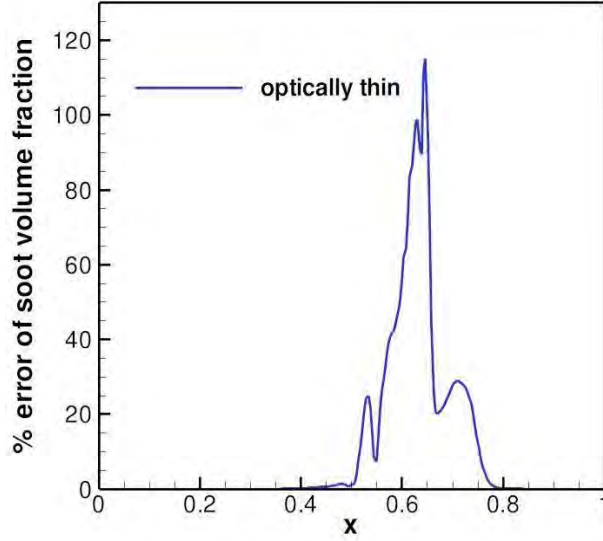
Figure 65. The calculated error of soot volume fraction between the optically thin radiation model to the P_1 gray model, where P_1 gray model is assumed to be the correct solution.

treatments of soot chemistry using both full and reduced mechanisms. The transport equation for the mixture fraction is defined as

$$\frac{\partial \rho Z}{\partial t} + \frac{\partial \rho Z u_j}{\partial x_j} = \frac{\partial}{\partial x_j}\left(\rho D_Z \frac{\partial Z}{\partial x_j}\right).$$

The flamelet equations are written as [109]

$$\rho \frac{\partial Y_k}{\partial t} = \frac{\rho \chi}{2 Le_k} \frac{\partial^2 Y_k}{\partial Z^2} + \frac{1}{4}\left(\frac{1}{Le_k} - 1\right)\left[\frac{\chi}{D_Z}\frac{\partial}{\partial Z}(\rho D_Z) + \frac{\partial \rho \chi}{\partial Z}\right]\frac{\partial Y_k}{\partial Z} + \acute{\omega}_k,$$

$$\rho \frac{\partial T}{\partial t} = \frac{\rho \chi}{2}\frac{\partial^2 T}{\partial Z^2} + \left[\frac{\rho \chi}{2 c_p}\frac{\partial c_p}{\partial Z} + \frac{\partial \rho \chi}{2 c_p}\sum \frac{c_{p,k}}{Le_k}\frac{\partial Y_k}{\partial Z}\right]\frac{\partial T}{\partial Z} + \frac{\acute{\omega}_k}{c_p} + \frac{Q_r}{c_p}.$$

where $\chi = 2 D_Z \dfrac{\partial Z}{\partial x_j}\dfrac{\partial Z}{\partial x_j}$ is the scalar dissipation. Temperature, species, specific heat, enthalpy, rate of production and heat loss are T, Y_k, $c_{p,k}$, h_k, $\acute{\omega}_k$, and Q_R, respectively for the k_{th} species.

The flamelet transformation for non-gray modeling of equation (1) is

$$\frac{\chi}{2 D_Z}\frac{\partial^2 G}{\partial Z^2} + \frac{\partial G_j}{\partial Z}\left[\frac{1}{4 D_Z}\frac{\partial \chi}{\partial Z} - \frac{\chi}{4 D_Z^2}\frac{\partial D_Z}{\partial Z} - \frac{\chi}{2 D_Z ku}\frac{\partial ku}{\partial Z}\right] \qquad (3)$$

$$= 3 k^2 u^2\left(G_j - 4\pi a_j I_b\right) \qquad j = 1,\dots\dots,M$$

66

The boundary conditions for equation (3) are

$$-\frac{2(2-\varepsilon)}{3\varepsilon}\sqrt{\frac{\chi}{2D_Z}}\frac{\partial G_j}{\partial Z}+k_j u G_j = 4\pi k_j u a_j I_b.$$

For gray mediums, the radiation model in mixture fraction space (Eq. 2) is

$$\frac{\chi}{2D_Z}\frac{\partial^2 G}{\partial Z^2}+\frac{\partial G}{\partial Z}\left[\frac{1}{4D_Z}\frac{\partial \chi}{\partial Z}-\frac{\chi}{4D_Z^2}\frac{\partial D_Z}{\partial Z}-\frac{\chi}{2D_Z \kappa_p}\frac{\partial \kappa_p}{\partial Z}\right] \quad (4)$$
$$= 3\kappa_p\left(G_j - 4\pi I_b\right).$$

The boundary conditions for equation (4) are

$$-\frac{2(2-\varepsilon)}{3\varepsilon}\sqrt{\frac{\chi}{2D_Z}}\frac{\partial G}{\partial Z}+\kappa_p G_j = 4\pi\kappa_p I_b.$$

For soot modeling, the two-equation flamelet model from Carbonell et al. [111] is used, i.e,

$$\rho\frac{\partial Y_s}{\partial t}=\frac{\rho\chi}{2Le_{Y_s}}\frac{\partial^2 Y_s}{\partial Z^2}-\sqrt{\frac{\chi}{2D_Z}}\frac{\partial \rho Y_s V_s}{\partial Z}+\dot{\omega}_{Y_s}$$

$$\rho\frac{\partial N_s}{\partial t}=\frac{\rho\chi}{2Le_{N_s}}\frac{\partial^2 N_s}{\partial Z^2}-\sqrt{\frac{\chi}{2D_Z}}\frac{\partial \rho N_s V_s}{\partial Z}+\dot{\omega}_{N_s}.$$

This system handles the soot model of Leung et al. as well as Pitsch et al. [118]. Generally, the Lewis number for soot particles is large and is neglected. The thermophoresis term is

$$V_s=-0.556\frac{\nu}{T}\sqrt{\frac{\chi}{2D_Z}}\frac{\partial T}{\partial Z}.$$

The coupled system of models described above was used to simulate the CRF piloted ethylene jet experiment for a jet Reynolds number of 20,000. The experiment conditions are list in Table 1. The computational domain and qualitative comparison with the experiment are shown in Fig. 66. Green is the fuel jet (i.e., isocontour where the mixture fraction is 0.8). Yellow is an isocontour that represents where the soot volume fraction is 5% of the peak value in the field. Purple is an arbitrary value of soot volume fraction in the vicinity of the peak value. Here we use the soot volume fraction to qualitatively mark a region in approximately the same vicinity as the luminosity in the photograph of the actual flame. This shows a qualitative correspondence in the turbulence structure between the simulated and actual flames.
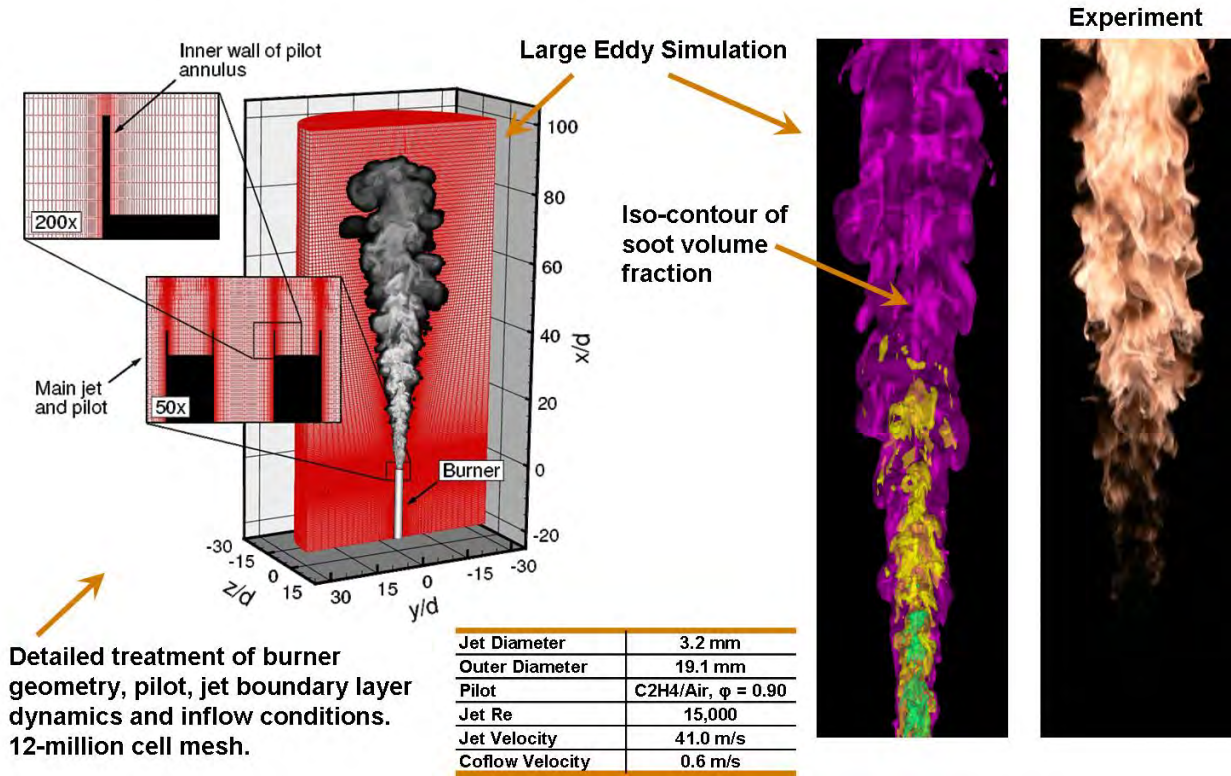
Figure 66.   LES of the CRF piloted ethylene diffusion flame showing the computational domain, flow conditions and instantaneous soot volume fraction with a qualitative comparison to the experiment.

Table 3: Operating conditions for piloted ethylene jet flame

Jet Diameter	Outer Diameter	Pilot	Jet Reynolds number	Jet velocity	Coflow velocity
3.2 mm	19.1 mm	φ=0.9	20,000	54.7 m/s	0.6 m/s

Figure 67 shows the computed and measured soot volume fraction versus axial distance along the centerline of the burner. The blue curve is the time-averaged prediction from LES. The red is the experimental LII data. For the LES, the error bars indicate the effect that a 20 K change in mean local temperature has on the performance of the soot model. For the experiment, the error bars represent an uncertainty of 20 percent in accuracy. Surprisingly good agreement is achieved to within the uncertainties over the complete interval between x/d of 0 to 300. The LES computations with the Leung et al. soot model and the P_1 non-gray radiation model tends to overpredict the experimental soot concentrations. However, the experimental concentrations are known to be underpredicted by ~ 10% because of the effects of signal trapping, as previously discussed, so the actual disparity between the simulations and the measurements is smaller than suggested by Fig. 67.
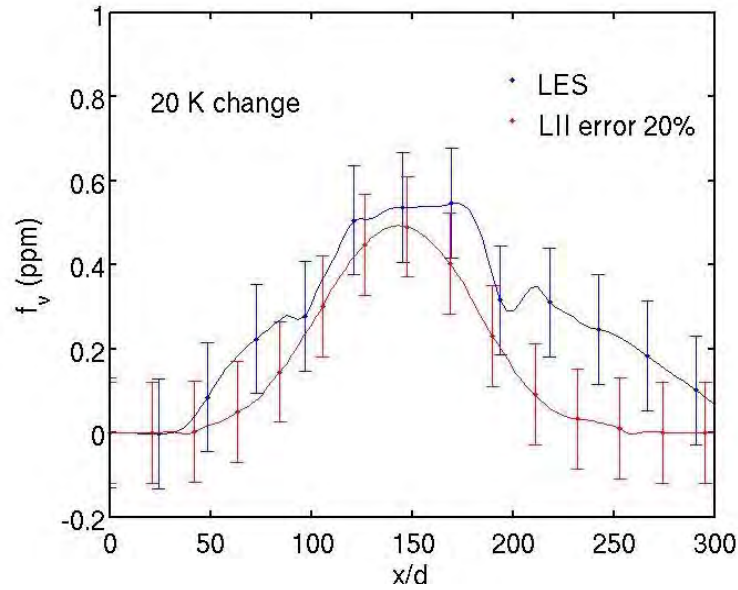
Figure 67.   Soot volume fraction versus axial distance along
the centerline of the burner.

The trends shown above highlight the sensitivities and demonstrate the potential for misinterpretations of the modeling results if the sole focus is on the soot part of the problem. Our analysis has highlighted the sensitivity of predictions to the combined influence of the radiation and soot models. The combination of using the new, reduced ethylene chemical kinetic model, the Modest P_1 non-gray radiation model, and the Leung et al. soot model yields quite accurate soot predictions for the investigated ethylene jet flame.

6.0 Conclusions and Implications for Future Research

Measurements of soot formation were performed in laminar flat premixed flames and turbulent non-premixed jet flames at 1 atm pressure and in turbulent liquid spray flames under representative conditions for takeoff in a gas turbine engine. The laminar flames and open jet flames used both ethylene and a prevaporized JP-8 surrogate fuel composed of n-dodecane and m-xylene. The pressurized turbulent jet flame measurements used the JP-8 surrogate fuel and compared its combustion and sooting characteristics to a world-average JP-8 fuel sample. The pressurized jet flame measurements demonstrated that the surrogate was representative of JP-8, with a somewhat higher tendency to soot formation. The premixed flame measurements revealed that flame temperature has a strong impact on the rate of soot nucleation and particle coagulation, but little sensitivity in the overall trends was found with different fuels. Even in the higher temperature flames, the soot particles demonstrated liquid-like behavior. Significant quantities of aliphatic carbon were found in soot sampled from the premixed flames. An extensive array of non-intrusive optical and laser-based measurements was performed in turbulent non-premixed jet flames established on specially designed piloted burners. Soot concentration data was collected throughout the flames, together with instantaneous images showing the relationship between soot and the OH radical and soot and PAH. Time-records of local soot concentration-temperature were collected, as well as spatially resolved thermal radiation emitted from the flames. Measurements of red laser light extinction across the flames provided useful data for correcting the soot concentration measurements for signal trapping.

A detailed chemical kinetic mechanism for ethylene combustion, including fuel-rich chemistry and benzene formation steps, was compiled, validated, and reduced. Difficulties in existing m-xylene chemical kinetic mechanisms prevented the development of a reduced mechanism for the JP-8 surrogate. The reduced ethylene mechanism was incorporated into a high-fidelity LES code, together with a moment-based soot model and models for thermal radiation, to evaluate the ability of the chemistry and soot models to predict soot formation in the jet diffusion flame. The LES results highlight the importance of including an optically-thick radiation model to accurately predict gas temperatures and thus soot formation rates. When including such a radiation model, the LES model predicts mean soot concentrations within 30% in the ethylene jet flame.

The results of this project suggest that LES modeling, when incorporating suitably reduced chemical kinetics with fuel-rich chemistry and a suitable, optically-thick radiation model, can predict soot formation with good accuracy in an ethylene nonpremixed jet flame (at 1 atm) when using a fairly simple soot model (developed explicitly for application to ethylene flames). Extension of this predictive ability to more complex fuels representative of JP-8 requires improvements in the understanding of aromatic oxidation and pyrolysis chemistry and may require further improvements to the soot model itself. The single most important insight that was gained from this project was that it is essential for a suitable radiation model, generally meaning one designed for at least moderately optically thick environments, to be directly incorporated into the turbulent flame model, together with a soot model. Simply incorporating a soot model in post-processing mode, as has generally been done to-date in predicting soot formation and emission from gas turbine engines, is not a meaningful test of the soot model, because the predicted flow field temperatures will be in significant error, and the soot formation chemistry is

characterized by a high activation energy. Incorporating soot models with increasing complexity while neglecting the influence of radiation does not guarantee any more accurate results than using the simplest soot model.

In the three years that we have worked on this problem, we have made significant strides, in keeping with the original project plan. To generate a soot and radiation model that is truly predictive for gas turbine combustion engines, (a) more work needs to be done to clarify aromatics reaction chemistry, particularly under fuel-rich conditions, (b) a suitable reduced chemical kinetic mechanism needs to be generated for the JP-8 surrogate for which we made experimental measurements in this project, and (c) detailed comparisons need to be made between LES model predictions (using a suitable radiation and soot model) and the experimental measurements. To account for variations in JP-8 composition, measurements should be performed in a piloted turbulent jet flame burner (such as developed here) for different fuel compositions, reduced chemical kinetic mechanisms should be developed, and then comparisons should be made with LES simulations and measurements. If these comparisons prove to not be favorable, adjustments should be made to either the form or the constants in the soot model to give better agreement. Having validated the soot/radiation model for applications at 1 atm pressure, LES simulations should be performed of a pressurized experiment using the same fuel.

7.0 Literature Cited

[1] F. Laden, L.M. Neas, D.W. Dockery, J. Schwartz, "Association of fine particulate matter from different sources with daily mortality in six US cities," *Envir. Health Persp.* 108:941-947 (2000).

[2] J.A. Sarnat, J. Schwartz, P.J. Catalon, H.H. Suh, "Gaseous pollutants in particulate matter epidemiology: Confounders or surrogates?" *Envir. Health Persp.* 109:1053-1061 (2001).

[3] C.A. Pope, R.T. Burnett, M.J. Thun, E.E. Calle, D. Krewski, K. Ito, G.D. Thurston, "Lung cancer, cardiopulmonary mortality, and long-term exposure to fine particulate air pollution," *JAMA* 287:1132-1141 (2002).

[4] A.J. Ghio, Y.C.T. Huang, "Exposure to concentrated ambient particles (CAPs): A review," *Inhalation Toxic.* 16:53-59 (2004).

[5] EPA Report No. EPA 600/6-04/058, "Particulate Matter Research Program: Five years of progress," July 2004, available at www.epa.gov.

[6] R.J. Delfino, C. Sioutas, S. Malik, "Potential role of ultrafine particles in associations between airborne particle mass and cardiovascular health," *Envir. Health Persp.* 113:934-946 (2005).

[7] C. de Haar, I. Hassing, M. Bol, R. Bleumink, R. Pieters, "Ultrafine carbon black particles cause early airway inflammation and have adjuvant activity in a mouse allergic airway disease model," *Toxic. Sciences* 87:409-418 (2005).

[8] R.B. Schlesinger, N. Kunzli, G.M. Hidy, T. Gotschi, M. Jerrett, "The health relevance of ambient particulate matter characteristics: Coherence of toxicological and epidemiological inferences," *Inhalation Toxic.* 18:95-125 (2006).

[9] R. Watson, J. Houghton, D. Yihui, B. Metz, O. Davidson, N. Sundararaman, D. Griggs, D. Dokken, *Aviation and the Global Atmosphere*, a special report of the Intergovernmental Panel on Climate Change (IPCC), 1999, available from http://www.grida.no/climate/ipcc/aviation/.

[10] L.G. Blevins, "Particulate matter emitted from aircraft engines," AIAA Paper 2003-0666, presented at the AIAA/ICAS International Air and Space Symposium and Exposition: The Next 100 Years, Dayton OH, 2003.

[11] L.H. Linden, J.B. Heywood, "Soot emission from jet engines," *Combust. Sci. Tech.* 2:401-411 (1971).

[12] P. Sampath, M. Gratton, D. Kretschmer, J. Odgers, "Fuel property effects upon exhaust smoke and the weak extinction characteristics of the Pratt & Whitney PT6A-65 engine," *J. Eng. Gas Turb. Power* 108:175-181 (1986).

[13] A. De Champlain, D. Kretschmer, J. Tsogo, G.F. Pearce, "Prediction of soot emissions in gas-turbine combustors," *J. Prop. Power* 13:117-122 (1997).

[14] E.M. Amin, G.E. Andrews, M. Pourkashnian, A. Williams, R.A. Yetter, "A computational study of pressure effects on pollutant generation in gas turbine combustors," *Trans. ASME* 119:76-83 (1997).

[15] A.K. Tolpadi, A.M. Danis, H.C. Mongia, R.P. Lindstedt, "Soot modeling in gas turbine combustors," ASME 97-GT-149, 1997.

[16] H.T. Brocklehurst, C.H. Priddin, J.B. Moss, "Soot predictions within an aero gas turbine combustion chamber," ASME 97-GT-148, 1997.

[17] H. Barths, N. Peters, N. Brehm, A. Mack, M. Pfitzner, V. Smiljanovski, "Simulation of pollutant formation in a gas-turbine combustor using unsteady flamelets," *Proc. Combust. Inst.* 27:1841-1847 (1998).

[18] M. Balthasar, F. Mauss, M. Pfitzner, A. Mack, "Implementation and validation of a new soot model and application to aeroengine combustors," *Trans. ASME* 124:66-74 (2002).

[19] E. Riesmeier, S. Honnet, N. Peters, "Flamelet modeling of pollutant formation in a gas turbine combustion chamber using detailed chemistry for a kerosene model fuel," *J. Eng. Gas Turb. Power* 126:899-905 (2004).

[20] W.-W. Kim, S. Menon, H.C. Mongia, "Large-eddy simulation of a gas turbine combustor flow," *Combust. Sci. and Tech.* 143:25-62 (1999).

[21] F. di Mare, W.P. Jones, K.R. Menzies, "Large eddy simulation of a model gas turbine combustor," *Combust. Flame* 137:278-294 (2004).

[22] P. Moin, S. Apte, "Large-eddy simulation of realistic gas turbine combustors," AIAA Paper 2004-330, 2004.

[23] W.-W. Kim, S. Syed, "Large-eddy simulation needs for gas turbine combustor design," AIAA Paper 2004-331, 2004.

[24] S. James, J. Zhu, M.S. Anand, "Large-eddy simulations of gas turbine combustors," AIAA Paper 2005-552, 2005.

[25] C.R. Shaddix, J.E. Harrington, K.C. Smyth, "Quantitative measurements of enhanced soot production in a flickering methane/air diffusion flame," *Combust. Flame* 99:723-732 (1994).

[26] C.R. Kaplan, C.R. Shaddix, K.C. Smyth, "Computations of enhanced soot production in time-varying CH_4/air diffusion flames," *Combust. Flame* 106:392-405 (1996).

[27] H. Pitsch, H. Steiner, "Large-eddy simulation of a turbulent piloted methane/air diffusion flame (Sandia flame D)," *Phys. Fluids* 12:2541-2554 (2000).

[28] A. Kempf, A. Sadiki, J. Janicka, "Prediction of finite chemistry effects using large eddy simulation," *Proc. Combust. Inst.* 29:1979-1985 (2002).

[29] H. Pitsch, "Improved pollutant predictions in large-eddy simulations of turbulent non-premixed combustion by considering scalar dissipation rate fluctuations," *Proc. Combust. Inst.* 29:1971-1978 (2002).

[30] C.D. Pierce, P. Moin, "Progress-variable approach for large-eddy simulation of non-premixed turbulent combustion," *J. Fluid Mech.* 504:73-97 (2004).

[31] A. Kempf, F. Flemming, J. Janicka, "Investigation of lengthscales, scalar dissipation, and flame orientation in a piloted diffusion flame by LES," *Proc. Combust. Inst.* 30:557-565 (2005).

[32] M.R.H. Sheikhim, T.G. Drozda, P. Givi, F.A. Jaberi, S.B. Pope, "Large eddy simulation of a turbulent nonpremixed piloted methane jet flame," *Proc. Combust. Inst.* 30:549-556 (2005).

[33] S. Navarro-Martinez, A. Kronenburg, F. di Mare, "Conditional moment closure for large eddy simulations," *Flow Turbulence Combust.* 75:245-274 (2005).

[34] R.S. Barlow, N.S.A. Smith, J.-Y. Chen, R.W. Bilger, "Nitric oxide formation in dilute hydrogen jet flames: Isolation of the effects of radiation and turbulence-chemistry submodels," *Combust. Flame* 117:4-31 (1999).

[35] R.S. Barlow, G.J. Fiechtner, C.D. Carter, J.-Y. Chen, "Experiments on the structure of turbulent CO/H2/N2 jet flames," *Combust. Flame* 120:549-569 (2000).

[36] W. Meier, R.S. Barlow, Y.-L. Chen, J.-Y. Chen, "Raman/Rayleigh/LIF measurements in a turbulent CH4/H2/N2 jet diffusion flame: Experimental techniques and turbulence chemistry interaction," *Combust. Flame* 120:326-343 (2000).

[37] R.S. Barlow, J.H. Frank, "Effects of turbulence on species mass fractions in methane/air jet flames," *Proc. Combust. Inst.* 27:1087-1095 (1998).

[38] K.M. Leung, R.P. Lindstedt, W.P. Jones, "A simplified reaction mechanism for soot formation in non-premixed flames," *Combust. Flame* 87:289-305 (1991).

[39] X. You, F.N. Egolfopoulos, H. Wang, "Detailed and simplified kinetic models of n-dodecane oxidation: The role of fuel cracking in aliphatic hydrocarbon combustion," *Proc. Combust. Inst*. 32:403-410 (2009).

[40] F. Battin-Leclerc, R. Bounaceur, N. Belmekki, P.A. Glaude, "Experimental and modeling study of the oxidation of xylenes," Int. J. Chem. Kinet. 38:284-302 (2006).

[41] M. Frenklach, H. Wang, "Detailed modeling of soot particle nucleation and growth," *Proc. Combust. Inst.* 23:1559-1566 (1991).

[42] M. Frenklach, H. Wang, "Detailed mechanism and modeling of soot particle formation," in <u>Soot Formation in Combustion: Mechanisms and Models of Soot Formation</u>, (Bockhorn, H., ed.), Springer Series in Chemical Physics, vol. 59, Springer-Verlag, Berlin, 1994, pp.162-190.

[43] H. Wang, M. Frenklach, "A detailed kinetic modeling study of aromatics formation, growth and oxidation in laminar premixed ethylene and acetylene flames," *Combust. Flame* 110: 173-221 (1997).

[44] H. Richter, J.B. Howard, "Formation of polycyclic aromatic hydrocarbons and their growth to soot—a review of chemical reaction pathways," *Prog. Energy Combust. Sci.* 26:565-608 (2000).

[45] J.A. Miller, S.J. Klippenstein, "The recombination of propargyl radical: solving the master equation," *J. Phys. Chem. A* 105:7254-7266, (2001).

[46] B. Zhao, Z. Yang, M.V. Johnston, H. Wang, A. S. Wexler, M. Balthasar, M. Kraft, "Measurement and numerical simulation of soot particle size distribution functions in a laminar premixed ethylene-oxygen-argon flame," *Combust. Flame* 133: 173-188 (2003).

[47] M.B. Colket, R.J. Hall, in <u>Soot Formation in Combustion: Mechanisms and Models of Soot Formation</u>, (Bockhorn, H., ed.), Springer Series in Chemical Physics, vol. 59, Springer-Verlag, Berlin, 1994, 442-468.

[48] J. Appel, H. Bockhorn, M. Wulkow, "Numerical simulation of soot particle size distributions with a discrete galerkin method," In Scientific Computing in Chemical Engineering II, Simulation, Image Processing, Optimization, and Control, F. Keil, W. Mackens, H. Voß, J. Werther (ed.), Berlin Heidelberg, 1999, p. 94.

[49] J. Singh, M. Balthasar, M. Kraft, W. Wagner, "Stochastic modeling of soot particle size and age distributions in laminar premixed flames," *Proc. Combust. Inst.* 30:1457-1465 (2005).

[50] J. Singh, R.I.A. Patterson, M. Kraft, H. Wang, "Numerical simulation and sensitivity analysis of detailed soot particle size distribution in laminar premixed ethylene flames," *Combust. Flame* 145:117-127 (2006).

[51] T. Løvås, D. Nilsson, F. Mauss, "Automatic reduction procedure for chemical mechanisms applied to premixed methane/air flames," *Proc. Combust. Inst.* 28:1809–1815 (2000).

[52] B. Zhao, Z. Yang, J. Wang, M. V. Johnston, H. Wang, "Analysis of soot nanoparticles in a laminar premixed ethylene flame by scanning mobility particle sizer," *Aerosol Sci. Technol.* 37:611-620 (2003).

[53] B. Zhao, Z. Yang, Z. Li, M. V. Johnston, H. Wang, "Particles size distribution function of incipient soot in laminar premixed ethylene flames: effect of flame temperature," *Proc. Combust. Inst.* 30: 1441-1448 (2005).

[54] S.C. Wang, R.C. Flagan, "Scanning electrical mobility spectrometer," *Aer. Sci. Technol.* 13: 230-240 (1990).

[55] C. M. Sorensen, "The mobility of fractal aggregates: a review," *Aer. Sci. Technol.* 45: 755-769 (2011).

[56] M.A. Delichatsios, "Transition from momentum to buoyancy-controlled turbulent jet diffusion flames and flame height relationships," *Combust. Flame* 92:349–364 (1993).

[57] R.W. Schefer, W.G. Houf, B. Bourne, J. Colton, "Spatial and radiative properties of an open-flame hydrogen plume," in press, *Int. J. Hydrogen Energy*.

[58] L.M. Pickett, D.L. Siebers, "Soot in diesel fuel jets: effects of ambient temperature, ambient density, and injection pressure," *Combust. Flame* 138:114–135 (2004).

[59] J.D. Naber, D.L. Siebers, "Effects of gas density and vaporization on penetration and dispersion of diesel sprays," *SAE Paper* 960034, 1996.

[60] D.L. Siebers, "Liquid phase fuel penetration in diesel sprays," *SAE Paper* 980809, 1998.

[61] D.L. Siebers, B. Higgins, L.M. Pickett, "Flame liftoff on direct-injection diesel fuel jets: Oxygen concentration effects," *SAE Paper* 2002-01-0890, 2002.

[62] D.L. Siebers, "Scaling liquid phase fuel penetration in diesel sprays based on mixing-limited vaporization," *SAE Paper* 1999-01-0528, 1999.

[63] J.C. Oefelein, "Thermophysical characteristics of LOX-H2 flames at supercritical pressure," *Proc. Combust. Inst.* 30: 2929-2937 (2005).

[64] J.C. Oefelein, "Mixing and combustion of cryogenic oxygen-hydrogen shear-coaxial jet flames at supercritical pressure," *Combust. Sci. and Tech.* 178:229-252 (2006).

[65] J.C. Oefelein, V. Sankaran, T.G. Drozda, "Large eddy simulation of swirling particle-laden flow in a model axisymmetric combustor," *Proc. Combust. Inst.* 31:2291-2299 (2007).

[66] J.C. Oefelein, "Large eddy simulation of turbulent combustion processes in power and propulsion systems," *Prog. Aerosp. Sci.* 42:2-37 (2006).

[67] J.C. Oefelein, R.W. Schefer, R.W. Barlow, "Toward validation of large-eddy simulation for turbulent combustion ," *AIAA J.* 44:418-433 (2006).

[68] G. Erlebacher, M.Y. Hussaini, C.G. Speziale, T.A. Zang, "Toward the large eddy simulation of compressible turbulent flows," *J. Fluid Mech.* 238:155-185 (1992).

[69] C.G. Speziale, "Galilean invariance of subgrid-scale stress models in the large eddy simulation of turbulence," *J. Fluid Mech.* 156:55-62 (1985).

[70] M. Germano, U. Piomelli, P. Moin, W.H. Cabot, "A dynamic subgrid-scale eddy viscosity model," *Phys. Fluids* 3:1760-1765 (1991).

[71] P. Moin, K. Squires, W. Cabot, S. Lee, "A dynamic subgrid-scale model for compressible turbulence and scalar transport," *Phys. Fluids* 3:2746-2757 (1991).

[72] D.K. Lilly, "A proposed modification of the Germano subgrid-scale closure method, *Phys. Fluids* 3:633-635 (1992).

[73] J. Smagorinsky, "General circulation experiments with the primitive equations. I. The basic experiment," *Monthly Weather Rev.* 9:99-164 (1963).

[74] T.W. Leland, P.S. Chappelear, "The corresponding states principle. A review of current theory and practice," *Ind. Eng. Chem. Fund.* 60:15-43 (1968).

[75] J.S. Rowlinson, I.D.Watson, "The prediction of the thermodynamic properties of fluids and fluid mixtures-I. The principle of corresponding states and its extensions," *Chem. Eng. Science* 24:1565-1574 (1969).

[76] A.Y. Klimenko, R.W. Bilger, "Conditional moment closure for turbulent combustion," *Prog. Energy Combust. Sci.* 25:595-687(1999).

[77] C. Pantano, S. Sarkar, "A subgrid model for nonlinear functions of a scalar," *Phys. Fluids* 13:3803-3819 (2001).

[78] J. P. Mellado, S. Sarkar, C. Pantano, "Reconstruction subgrid models for nonpremixed combustion," *Phys. Fluids* 15:3280-3307 (2003).

[79] H. Wang, X. You, A.V. Joshi, S.G. Davis, A. Laskin, F. Egolfopoulos, C.K. Law, USC Mech Version II. High-Temperature Combustion Reaction Model of H2/CO/C1-C4 Compounds. http://ignis.usc.edu/USC_Mech_II.htm , May 2007.

[80] C.J. Brown, G.O. Thomas, *Combust. Flame* 117:861-870 (1999).

[81] D.A. Sheen, X. You, H. Wang, T. Løvås, "Spectral uncertainty quantification, propagation and optimization of a detailed kinetic model for ethylene combustion," *Proc. Combust. Inst*. 32:535-542 (2009).

[82] S.S. Vasu, D.F. Davidson, Z. Hong, V. Vasudevan, R.K. Hanson, "*n*-Dodecane oxidation at high-pressures: Measurements of ignition delay times and OH concentration time-histories," *Proc. Combust. Inst*. 32:173-180 (2009).

[83] T.J. Farrell, R.J. Johnston, I.P. Androulakis, "Molecular structure effects on laminar burning velocities at elevated temperature and pressure," *SAE Paper* 2004-01-2936, 2004.

[84] C.A. Taatjes, D.L. Osborn, T.M. Selby, G. Meloni, A.J. Trevitt, E. Epifanivskii, A.I. Krylov, B. Sirjean, E. Dames, H. Wang, "Products of the benzene + O(3P) reaction," *J. Phys. Chem. A* 114:3355-3370 (2010).

[85] A.D. Abid, N. Heinz, E.D. Tolmachoff, D.J. Phares, C.S. Campbell, H. Wang, "On the evolution of particle size distribution functions of soot in premixed ethylene-oxygen-argon flames," *Combust. Flame* 154:775-788 (2008).

[86] A.D. Abid, E.D. Tolmachoff, D.J. Phares, H. Wang, Y. Liu, A. Laskin, "Size distribution and morphology of nascent soot in premixed ethylene flames with and without benzene doping," *Proc. Combust. Inst*. 32:681-688 (2009).

[87] A.D. Abid, J. Camacho, D.A. Sheen, H. Wang, "Quantitative measurement of soot particle size distribution in premixed flames–the burner-stabilized stagnation flame approach," *Combust. Flame* 156:1862–1870 (2009).

[88] A.D. Abid, J. Camacho, D.A. Sheen, H. Wang, "Evolution of soot particle size distribution function in burner-stabilized stagnation *n*-dodecane-oxygen-argon flames," *Energy & Fuels* 23:4286-4298 (2009).

[89] J.P. Cain, P.L. Gassman, H. Wang, A. Laskin, "Micro-FTIR study of soot chemical composition – evidence of aliphatic hydrocarbons on nascent soot surfaces," (feature article), *Physical Chemistry Chemical Physics* 12:5206-5218 (2010).

[90] J.P. Cain, J. Camacho, D.J. Phares, H. Wang, A. Laskin, "Evidence of aliphatics in nascent soot particles formed in premixed ethylene flames," *Proc. Combust. Inst*. 33:533-540 (2011).

[91] J. Zhang, C.R. Shaddix, R.W. Schefer, "Design of 'model-friendly' turbulent non-premixed jet burners for C2+ hydrocarbon fuels." submitted to *Rev. Sci. Instr*.

[92] K.C. Smyth, C.R. Shaddix, D.A. Everest, *Combust. Flame* 111:185–207 (1997).

[93] T.C. Williams, C.R. Shaddix, K.A. Jensen, and J.M. Suo-Anttila, "Measurement of the dimensionless extinction coefficient of soot within laminar diffusion flames," *Int. J. Heat and Mass Transfer* 50:1616-1630 (2007).

[94] C.J. Dasch, "One-dimensional tomography: a comparison of Abel, onion-peeling, and filtered backprojection methods," *Appl. Optics* 31:1146-1152 (1992).

[95] T.C. Williams, C.R. Shaddix, "Simultaneous correction of flat field and nonlinearity response of intensified charge-coupled devices," *Rev. Sci. Instr.* 78, 123702 (2007).

[96] N.H. Qamar, Z.T. Alwahabi, Q.N. Chan, G.J. Nathan, D. Roekaerts, K.D. King, "Soot volume fraction in a piloted turbulent jet non-premixed flame of natural gas," *Combust. Flame* 156:1339–1347 (2009).

[97] S.S. Krishnan, K.-C. Lin, G.M. Faeth, "Extinction and scattering properties of soot emitted from buoyant turbulent diffusion flames," *J. Heat Trans.* 123:331-339 (2001).

[98] F. Goulay, P.A. Schrader, L. Nemes, M. Dansson, H.A. Michelsen, "Photochemical interferences for laser-induced incandescence of flame-generated soot,"*Proc. Combust. Inst.* 32:963-970 (2009).

[99] R.J. Santoro, C.R. Shaddix, "Laser-induced incandescence," in: K. Kohse-Höinghaus, J.B. Jeffries (Eds.), Applied Combustion Diagnostics, Taylor & Francis, New York, NY, 2002, pp. 252–286.

[100] H.A. Michelsen, P.O. Witze, D. Kayes, S. Hochgreb, "Time-resolved laser-induced incandescence of soot: the influence of experimental factors and microphysical mechanisms," *Appl. Optics* 42:5577-5590 (2003).

[101] M.P. Musculus, L.M. Pickett, "Diagnostic considerations for optical laser-extinction measurements of soot in high-pressure transient combustion environments," *Combust. Flame* 141:371-391 (2005).

[102] Y.R. Sivathanu, G.M. Faeth, "Temperature/soot volume fraction correlations in the fuel-rich region of buoyant turbulent diffusion flames," *Combust. Flame* 81:150-165 (1990).

[103] A. Coppalle, D. Joyeux, "Temperature and soot volume fraction in turbulent diffusion flames: measurements of mean and fluctuating values," *Combust. Flame* 96:275-284 (1994).

[104] L.A. Gritzo, Y.R. Sivathanu, W. Gill, "Transient measurements of radiative properties, soot volume fraction and soot temperature in a large pool fire," *Combust. Sci. and Tech.* 139:113–136 (1998).

[105] J.J. Murphy, C.R. Shaddix, "Soot property measurements in a two-meter diameter JP-8 pool fire," *Combust. Sci. and Tech.* 178:865–894 (2006).

[106] S. Kook, L.M. Pickett, "Soot volume fraction and morphology of conventional and surrogate jet fuel sprays at 1000-K and 6.7-MPa ambient conditions," *Proc. Combust. Inst.* 33:2911-2918 (2011).

[107] A. Bhargava, P.R. Westmoreland, "Measured flame structure and kinetics in a fuel-rich ethylene flame," *Combust. Flame* 113:333–347 (1998).

[108] J. Appel, H. Bockhorn, M. Frenklach, "Kinetic modeling of soot formation with detailed chemistry and physics: laminar premixed flames of C2 hydrocarbons," *Combust. Flame* 121:122–136 (2000).

[109] H. Wang, D.X. Du, C.J. Sung, C.K. Law, "Experiments and numerical simulation on soot formation in opposed–jet ethylene diffusion flames," *Proc. Combust. Inst.* 26:2359–2368 (1996).

[110] M.F. Modest, Radiative Heat Transfer, 2nd ed., Academic Press, San Diego, 2003.

[111] L.Wang, D. Haworth, S. Turns, M. Modest, "Interactions among, thermal radiation, and *NOx* emissions in oxygen–enriched turbulent non–premixed flames: a computational fluid dynamics modeling study," *Combust. Flame* 141:170–179 (2005).

[112] L. Wang, M.F. Modest, D. C. Haworth and S. R. Turns, "Modeling nongray gas-phase and soot radiation in luminous turbulent nonpremixed jet flames," *Combust. Theory and Modeling* 9:479-498 (2005).

[113] J.H. Kent, D.R. Honnery, "Soot formation rates in diffusion flames – a unifying trend," *Combust. Sci. and Tech.* 75:287-298 (1991).

[114] H. Zhang, M. F. Modest, "Evaluation of the Planck-mean absorption coefficients from HITRAN and HITEMP databases," J. Quant. Spectroscopy Radiative Transf. 73:649-653 (2002).

[115] D. Carbonell, A. Oliva, C. Perez-Segarra, "Implementation of two-equation soot flamelet models of laminar diffusion flames," *Combust. Flame* 156:621-632 (2009).

[116] H. Watanabe, R. Kurose, S. Komori, H. Pitsch, "Effects of radiation on spray flame characteristics and soot formation," *Combust. Flame* 152:2-13 (2008).

[117] S. H. Chan, X. C. Pan, M. M. M. Abou-Ellail, "Flamelet structure of radiating CH4/air flames," *Combust. Flame* 102:438-446 (1995).

[118] H. Pistch, E. Riesmeier, N. Peters, "Unsteady flamelet modeling of soot formation in turbulent diffusion flame," *Combust. Sci. and Tech.* 158:389-406 (2000).

8.0 List of Technical Publications

Peer-Reviewed Journal Publications

[1] J. Zhang, C.R. Shaddix, R.W. Schefer, "Simultaneous 2-D imaging of OH/soot and PAH/soot in a turbulent nonpremixed jet flame," to be submitted to *Applied Physics B*.

[2] J. Zhang, C.R. Shaddix, R.W. Schefer, "Quantitative measurements of soot volume fraction in a turbulent nonpremixed ethylene jet flame," to be submitted to *Combustion and Flame*.

[3] J. Zhang, C.R. Shaddix, R.W. Schefer, "Design of 'model-friendly' turbulent non-premixed jet burners for C2+ hydrocarbon fuels." submitted to *Rev. Sci. Instr*.

[4] H. Wang, "Formation of nascent soot and other condensed-phase materials in flames," (Invited) *Proc. Combust. Inst.* 33:41-67 (2011).

[5] J.P. Cain, J. Camacho, D.J. Phares, H. Wang, A. Laskin, ―Evidence of aliphatics in nascent soot particles formed in premixed ethylene flames," *Proc. Combust. Inst.* 33:533-540 (2011).

[6] S. Kook, L.M. Pickett, "Soot volume fraction and morphology of conventional and surrogate jet fuel sprays at 1000-K and 6.7-MPa ambient conditions," *Proc. Combust. Inst*. 33:2911-2918 (2011).

[7] S. Kook, L.M. Pickett, ―Effect of Fuel Volatility and Ignition Quality on Combustion and Soot Formation at Fixed Premixing Conditions", SAE International Journal of Engines 2(2):11-23 (SAE Paper 2009-01-2643), 2010.

[8] J.P. Cain, P.L. Gassman, H. Wang, A. Laskin, ―Micro-FTIR study of soot chemical composition – evidence of aliphatic hydrocarbons on nascent soot surfaces," (feature article), *Physical Chemistry Chemical Physics* 12:5206-5218 (2010).

[9] C.A. Taatjes, D.L. Osborn, T.M. Selby, G. Meloni, A.J. Trevitt, E. Epifanivskii, A.I. Krylov, B. Sirjean, E. Dames, H. Wang, ―Products of the benzene + O(^{3}P) reaction," *Journal of Physical Chemistry A* 114:3355-3370 (2010).

[10] A.D. Abid, J. Camacho, D.A. Sheen, H. Wang, ―Evolution of soot particle size distribution function in burner-stabilized stagnation *n*-dodecane-oxygen-argon flames," *Energy & Fuels* 23:4286-4298 (2009).

[11] A.D. Abid, J. Camacho, D.A. Sheen, H. Wang, ―Quantitative measurement of soot particle size distribution in premixed flames–the burner-stabilized stagnation flame approach," (Feature article) *Combustion and Flame*, **156**, 1862–1870 (2009).

[12] A.D. Abid, E.D. Tolmachoff, D.J. Phares, H. Wang, Y. Liu, A. Laskin, ―Size distribution and morphology of nascent soot in premixed ethylene flames with and without benzene doping," *Proceedings of the Combustion Institute*, **32**, pp. 681-688 (2009).

[13] D.A. Sheen, X. You, H. Wang, T. Løvås, ―Spectral uncertainty quantification, propagation and optimization of a detailed kinetic model for ethylene combustion," *Proceedings of the Combustion Institute*, **32**, pp. 535-542 (2009).

[14] A.D. Abid, N. Heinz, E.D. Tolmachoff, D.J. Phares, C.S. Campbell, H. Wang, ―On the evolution of particle size distribution functions of soot in premixed ethylene-oxygen-argon flames," *Combustion and Flame*, 154, pp. 775-788 (2008).

Book Chapter

[15] H. Wang, A.D. Abid, ―Size distribution and chemical composition measurements of nascent soot formed in premixed ethylene flames," in Bockhorn, H., D'Anna, A., Sarofim, A. F., Wang, H. eds., Combustion Generated Fine Carbonaceous Particles, Karlsruhe University Press, 2009, Chapter 23, pp. 367-384.

Technical Reports

[16] C. Shaddix, H. Wang, R. Schefer, J. Oefelein, L. Pickett, "Predicting the Effects of Fuel Composition and Flame Structure on Soot Generation in Turbulent Non-Premixed Flames," 2009 SERDP Interim Project Report, Feb. 28., 2009.

[17] C. Shaddix, H. Wang, R. Schefer, J. Oefelein, L. Pickett, "Predicting the Effects of Fuel Composition and Flame Structure on Soot Generation in Turbulent Non-Premixed Flames," 2007 SERDP Annual Project Report, Dec. 14, 2007.

Conference Proceedings

[18] S. Kook, L.M. Pickett, "Quantitative Soot Measurement for Fuels with Different Cetane Number at Low-Temperature-Combustion Diesel Conditions," Proceedings of the Australian Combustion Symposium, pp. 207-210, Brisbane, Australia, Dec. 2-4, 2009.

[19] J. Zhang, C.R. Shaddix, R.W. Schefer, "Soot Formation in a Turbulent JP-8 Jet Flame Investigated by 2D Laser-induced Incandescence and Planar Laser-induced Fluorescence," Proceedings of Fall 2009 Meeting of the Western States Section of the Combustion Institute, paper 09F-57, Irvine, CA, Oct. 26–27, 2009.

[20] S. Kook, L.M. Pickett, "Combustion and Soot Processes of World-Average and Surrogate Jet Fuels at High Temperature and High-Pressure Conditions," Proceedings of 6th U.S. National Combustion Meeting, Ann Arbor, MI, May 17–20, 2009.

[21] A.D. Abid, J. Camacho, D.A. Sheen, H. Wang, "Burner-Stabilized Stagnation Flow Flame Approach to Probe Soot Size Distributions," Proceedings of 6th U.S. National Combustion Meeting, Ann Arbor, MI, May 17–20, 2009.

[22] A.D. Abid, H. Wang, "Particle Size Distribution Functions of Soot Formed in Laminar Premixed n-Dodecane-Oxygen-Argon Flames," Proceedings of 6th U.S. National Combustion Meeting, Ann Arbor, MI, May 17–20, 2009.

[23] D.A. Sheen, T. Lovas, H. Wang, "Reduction of Detailed Chemical Models with Controlled Uncertainty," Proceedings of 6th U.S. National Combustion Meeting, Ann Arbor, MI, May 17–20, 2009.

[24] J. Zhang, C.R. Shaddix, R.W. Schefer, "Investigation of Soot Formation in Turbulent Nonpremixed Ethylene Jet Flames by 2D Laser-Induced Incandescence and Planar Laser-Induced Fluorescence," Proceedings of 6th U.S. National Combustion Meeting, Ann Arbor, MI, May 17–20, 2009.

[25] A.D. Abid, H. Wang, "Study on the Presence of Nanoparticles in Near-Sooting Premixed Ethylene-Air Flat Flames," Proceedings of Spring 2008 Meeting of the Western States Section of the Combustion Institute, paper 08S-69, Los Angeles, CA, Mar. 16–18, 2008.

[26] J. Zhang, T.C. Williams, C.R. Shaddix R.W. Schefer, "Application of Planar LIF and LII Imaging to a Turbulent Nonpremixed Sooty Ethylene Jet Flame," Proceedings of Spring 2008 Meeting of the Western States Section of the Combustion Institute, paper 08S-30, Los Angeles, CA, Mar. 16–18, 2008.

[27] A.D. Abid, H. Wang, "Detailed Soot Particle Size Distributions and Modeling Study of Ethylene/Oxygen/Argon Flames Doped with Benzene," Proceedings of Fall 2007 Meeting of the Western States Section of the Combustion Institute, paper 07F-68, Livermore, CA, Oct. 16–17, 2007.

[28] A.D. Abid, N. Heinz, E.D. Tolmachoff, D.J. Phares, C.S. Campbell, H. Wang, "Evolution of Particle Size Distribution Function of Nascent Soot in Premixed Ethylene Flames," AAAR 2007 Annual Conference, Reno, NV, Sept. 24–28, 2007.

Conference Abstracts

[29] C.R. Shaddix, J. Zhang, R.W. Schefer, ―Towards Quantitative Measurements of Soot Concentration in Strongly Sooting Turbulent Jet Diffusion Flames," OSA LACSEA Conference, San Diego, CA, Feb. 1-3, 2010.

[30] C.R. Shaddix, J. Zhang, R.W. Schefer, L.M. Pickett, S. Kook, J. Doom, J.C. Oefelein, A. Abid, J. Camacho, H. Wang, ―Predicting the Effects of Fuel Composition and Flame Structure on Soot Generation in Turbulent Non-Premixed Flames," Partners in Environmental Technology Technical Symposium & Workshop, Washington, DC, December 1-3, 2009.

[31] J. Doom, J.C. Oefelein, ―Simulation of an ethylene-air jet flame with soot and radiation modeling," 62nd Annual American Physical Society DFD Meeting, Minneapolis, MN, Nov. 22-24, 2009.

[32] J. Zhang, C.R. Shaddix, R.W. Schefer, ―Application of 2D laser-induced incandescence and planar laser-induced fluorescence to a highly sooty turbulent jet flame" Gordon Research Conference on Laser Diagnostics in Combustion, Waterville Valley, NH, Aug. 16–21, 2009.

[33] C. Shaddix, J. Zhang, R. Schefer, L. Pickett, S. Kook, J. Oefelein, A. Abid, J. Camacho, H. Wang ―Predicting the Effects of Fuel Composition and Flame Structure on Soot Generation in Turbulent Non-Premixed Flames," Partners in Environmental Technology Technical Symposium & Workshop, Washington, DC, T-160, December 2-4, 2008.

[34] J. Zhang, C.R. Shaddix, R.W. Schefer, "Soot Volume Fraction Imaging in a Turbulent Nonpremixed Ethylene Jet Flame" 32nd International Combustion Symposium, Montreal, Canada, Aug. 3–8, 2008.

[35] J. Zhang, T.C. Williams, C.R. Shaddix, R.W. Schefer, ―Soot Volume Fraction Imaging in a Turbulent Nonpremixed Ethylene Jet Flame by Quantitative 2D Laser-Induced Incandescence," Ninth International Workshop on Measurement and Computation of Turbulent Nonpremixed Flames, Montreal, Canada, July 31–Aug. 2, 2008.

[36] T. Litzinger ―Combustion Science to Reduce PM Emissions from Military Engines: An Overview of Five New SERDP Projects," Partners in Environmental Technology Technical Symposium & Workshop, Washington, DC, December 4-6, 2007.